Politecnico di Torino

Master's Degree in Aerospace Engineering
Propulsion Systems

Master's Degree Thesis

Experimental characterisation of a Transpiration Cooling System for Rocket Engine applications using High-Test Peroxide as coolant

Advisors:

Prof. Andrea Ferrero
Prof. Christian Bach
PhD Suk Min Choi

Candidate:

Michele Paolicelli

A.A. 2025/2026

Abstract

The objective of this research is to validate the feasibility of applying the transpiration cooling at the combustion chamber of a liquid propelled rocket engine using an exothermic reactive propellant, namely high-concentration hydrogen peroxide. The research is driven by the critical need for efficient thermal management in advanced propulsion systems, particularly in high-performance liquid rocket engines utilizing high-concentration hydrogen peroxide (H_2O_2) as a propellant.

Conventional cooling methods like regenerative cooling, which relies on circulating the propellant through narrow internal channels, are not suitable for H_2O_2-based engines due to the material compatibility issues and the risk of vapour detonation caused by the propellant rapid boil-off. In fact, high-concentration H_2O_2 is highly reactive with most common high-conductivity metals, such as copper or nickel alloys, making it challenging to implement conventional cooling strategies. In addition, the high vapour pressure and exothermic decomposition characteristics of H_2O_2 significantly increase the risk of localized overheating and potential structural failure if not properly managed.

One of the most promising approaches to address this challenge is transpiration cooling, a technique that utilizes a porous wall to inject coolant directly into the hot gas flow, forming a protective boundary layer that significantly reduces thermal loads on structural components. This approach offers superior heat dissipation compared to film cooling, as it provides more uniform surface cooling and reduces peak thermal stresses. Additive manufacturing (AM) has emerged as a key enabler for allowing the precise fabrication of complex porous structures that can optimize coolant distribution, enhance mechanical strength and reduce overall component mass. However, the lack of comprehensive design guidelines and manufacturing techniques for porous structures remains a significant barrier to their widespread adoption.

This research thesis aims to address this gap, by focusing on the preliminary required steps for the development of a transpiration cooling system for a laboratory-scale rocket engine. In particular, the thesis focuses on definying a generalized framework for the design, manufacturing and performance characterisation of a porous component for transpiration cooling, additive manufactured through a promising and innovative technique called Laser Powder Bed Fusion (LPBF).

The investigated cooling system is designed as a three-parts assembly, the metallic housing, the cover and the porous structure. The first two components are manufactured at the TU Dresden laboratory workshop, meanwhile the porous structure is provided by TU Dresden partner IWS Fraunhofer. The thesis will then cover the development of a complete test bench specifically designed for the experimental characterisation of the cooling system. This setup will be employed for running a cold water flow test, whose aim is to assess the system's functionality and the porous structure actual permeability (namely the relation between the transpiring mass flow rate and the pressure drop across the wall) with various tank pressures. Moreover, the

setup is fully equipped with safety measures and emergency lines, which make it suitable also for running a possible hot-fire test of the engine.

Finally, the results acquired from the cold flow test will then serve as input for a final simulation and modelling process of the entire cooling technique. At this scope, a MATLAB script is developed, implementing the Allison's model of combustion for simulating the chemical reactions that may occur at the interface between the combustion chamber freestream and the transpiration cooling boundary layer. The simulation will produce a preliminary conclusion about the feasibility of applying transpiration cooling with high-concentration hydrogen peroxide employed as coolant and may represent the first step towards the development of an actual cooling performance assessment throughout an engine hot-fire test.

Index

List of Figures

List of Tables

Chapter 1

Introduction

Rocket engine performances directly depend on the temperature and the combustion chamber inner pressure, resulting that with the increasing of these values, specific impulse rises accordingly. However, an increase in their value inevitably leads to a greater **heat flux** across the walls. Heat is transmitted to all components exposed to hot gases, mostly by convection and, to a lesser extent (5 to 35%), as radiations, while conduction entity can generally be neglected. Nowadays rocket engines heat flux intensity can range from $50\ W/cm^2s$ to $20\ kW/cm^2s$, varying along the machine axial position, with a heat peak occurring at the nozzle throat region.

Such extreme heat loads can not be managed passively by the wall material alone, since materials lose strength as their temperature rises, ultimately failing or eventually melting. For example, a typical aluminum alloy for aerospace use loses up to 50% of its strength when heaten up to 200°C. On the other hand, combustion chamber temperatures commonly exceeds by far every material, even refractory ones, melting point. Therefore, the use of appropriate and advanced **cooling systems** is required to prevent the thrust chamber walls from failing, ensuring the safe operation of the engine and its structural integrity.

Over the past decades, advancements in high-temperature materials and propellants have continuously pushed engine performances, allowing for higher combustion temperatures and pressures. These developments have simultaneously increased the thermal loads on engine components, necessitating the research of more sophisticated cooling techniques for all space applications.

The great variety of possible solutions includes different cooling principles, from using a fluid as a heat sink, to passively cool the material through the emission of radiations. Every technique has a characteristic efficiency which makes it suitable for a specific application. However, the selection of a cooling system for a rocket engine combustion chamber is a complex process, influenced by multiple factors. As mentioned, the extreme operating conditions require careful evaluation of the heat flux to the walls and the material's ability to withstand degradation. The selection of high-performance materials is inevitably essential, complementing the cooling strategy, as the combination of thermal resistance and mechanical strength allows to tolerate higher heat fluxes.

The type of propellants also plays a crucial role, as it determines both the flame temperature and the possibility of using them as a coolant. The operating duration and the number of expected cycles further affect the choice, distinguishing between reusable configurations and systems designed for short operating times. Finally, cooling systems influence the overall en-

gine design, affecting mass distribution, structural layout and integration with auxiliary systems. Moreover, designers must consider the trade-off between thermal efficiency and simplicity, as overly complex systems can increase manufacturing difficulties and maintenance requirements.

A promising technique introduced in recent years is **transpiration cooling**, an advanced concept representing a potential evolution of the largely employed **film cooling**. This approach relies on a porous wall through which a liquid coolant is directly injected into the combustion chamber. As the coolant transpires through the wall, it simultaneously cools the structure, ultimately forming a protective boundary layer on the inner chamber's wall that significantly reduces thermal loads. This cooling solution can be a vastly favourable option for specific space applications, such as **hydrogen peroxide**-propelled rocket engines. Due to its high reactivity, this propellant is incompatible with most conventional cooling techniques, despite exhibiting several encouraging features like storability at room temperature and high combustion performances.

With the objective of developing a generalized framework for the design, manufacturing and performance characterisation of an hydrogen peroxide-based transpiration cooling system, this thesis covers the preparation and development of an experiment for validating the application of traspiration cooling to the combustion chamber of a rocket engine, where high-test hydrogen peroxide is employed as coolant. The aim of the experiment is to assess the feasibility of the cooling technique when applied to a laboratory-scale 500 N rocket engine. In particular, the research includes the development of a fully functioning experimental test bench, comprehending the propellant tanks and feeding system, a pressurization system and emergency and relief lines. The experimental setup is firstly validated through a water cold-flow test, verifing the correct operation of all valves and system components and experimentally measuring the porous structure permeability. Test results are subsequently considered as input for a numerical simulation of the transpiration cooling concept, which is a necessary step for conducting an actual hot firing test.

This dissertation presents the most crucial aspects that emerge during the development of an experimental research project, dealing with rocketry and highly reactive chemical substances, as well as the difficulties associated with modelling a difficult scenario such as the transpiration and decomposion of a fluid in a rocket combustion chamber.

In this introductory chapter, in order to better comprehend the functionality of rocket chambers cooling, the basic principles of heat flux theories will be presented. Subsequently, as a preliminary step toward the study of the advanced **transpiration cooling** technique, a brief overview of the conventional cooling methods used in aerospace applications for rocket engines will follow. Finally, a description of the oxidizer propellant used in the study, **hydrogen peroxide** and its properties, will be given, followed by the transpiration cooling system presentation, with its operation principles and related advantages.

1.1 Heat transfer analysis

During the design process of a rocket engine, heat transfer represents a crucial aspect which is firstly analysed through theoretical calculations and then always verified through experimental testing. The extremely high temperatures and heat fluxes generated during combustion lead to a complex thermal environment, in which multiple heat transfer mechanisms interact and must be carefully modelled to obtain reliable predictions.

There are three main mechanisms through which heat is transferred. **Conduction** consists of the energy diffusion by atomic interactions inside a solid material when a temperature difference occurs between two separated points. **Convection**, on the other hand, involves the transport of

energy through the movement of a fluid mass between two regions that experience a temperature difference and is particularly relevant in the presence of high-speed propellant flows. Finally, **radiation** is the emission of energy from a material in the form of electromagnetic waves, which becomes significant at high temperatures. In practical applications, these mechanisms act simultaneously and must be considered together to obtain a realistic prediction of the thermal behaviour of the engine.

The relations that describe each one of these mechanism in steady-state conditions are hereby presented. In these conditions and under the assumption of homogeneous and isotropic materials, the governing relations for the different heat transfer mechanisms can be expressed in a relatively compact analytical form. For conduction, the **Fourier's equation** applies:

$$\frac{Q}{A} = -k\frac{dT}{dy} \tag{1.1}$$

where Q is the heat flux across the surface area A measured in W, k is the solid material's thermal conductivity and dT/dy is the temperature gradient. Fourier's equation shows that conductive heat transfer is directly proportional to the temperature gradient inside a material, with energy transfer proceeding from warmer regions to colder ones. This formulation is valid as long as the material properties can be considered constant with temperature and no internal heat generation is present. Despite its simplicity, Fourier's law provides an effective description of heat conduction within solid rocket engine components such as chamber walls and nozzles. Meanwhile, for convection, the heat transfer relation is:

$$\frac{Q}{A} = h(T_1 - T_2) \tag{1.2}$$

where h is the fluid convective heat transfer coefficient, while T_1 and T_2 are the temperatures of the interacting regions across which heat exchange occurs. The value of the convective heat transfer coefficient incorporates the combined effects of fluid properties, flow regime and geometry. As a consequence, its evaluation typically relies on experimentally derived correlations. For example, for the convection of heat transfer in turbulent flows, the following empirical relation stands:

$$\frac{hD}{k} = 0.023\left(\frac{Dv\rho}{\mu}\right)^{0.8}\left(\frac{\mu c_p}{k}\right)^{0.4} \tag{1.3}$$

where D is the diameter of the chamber or the nozzle, v is the average velocity of the gas, ρ is the gas density, μ its viscosity and c_p its specific heat at constant pressure. Usually, heat transfer theories are also presented using dimensionless parameters, allowing the generalization of experimental results and facilitating the comparison between different flow configurations and operating conditions. Hence, the previous correlation can be written also adopting the Nusselt, the Reynolds and the Prandtl numbers:

$$Nu = 0.023 \cdot Re^{0.8} \cdot Pr^{0.4} \tag{1.4}$$

The presented empirical correlation is also known as **Bartz's equation** and comprehends empirical correcting factors for adjusting the formula to the real cases. The Bartz's equation will be subsequently used in this research for the computation of the theoretical hot flow convective heat transfer coefficient.

The radiation mechanism follows the **Stefan-Boltzmann equation**:

$$\frac{Q}{A} = \varepsilon\sigma T^4 \tag{1.5}$$

where ε is the emissivity of the waves emitting substance, σ is the Stefan-Boltzmann constant and T the substance's temperature. According to this formula, every material and substance loses energy in the form of electromagnetic waves proportionally to its temperature. The amount of energy loss is reduced by the ε parameter, which indicates the percentage of energy emission of a real material compared to an ideal **black body**. Although radiation can become relevant at extremely high temperatures, in the present study its contribution is neglected, as convective and conductive heat transfer dominate the overall thermal balance under the considered operating conditions.

In cases where the fluid is in motion and actively participates in the energy transport, heat transfer can no longer be described solely by the presented laws. Under these conditions, the local energy balance includes both the diffusion effect and the convective term associated with the enthalpy transport due to fluid motion, expressed as:

$$\rho c_p \vec{V} \cdot \nabla T = \nabla \cdot (k \nabla T) \tag{1.6}$$

The left-hand side of the equation represents the convective transport of thermal energy due to fluid motion, while the right-hand side accounts for thermal diffusion within the medium. This equation is derived from a steady-state energy balance and shows that even if the local heat flux can still be evaluated through Fourier's law ($q = -k\nabla T$), its value is not spatially constant, since it is affected by the convective contribution of the moving fluid.

Considering a small volume between two concentric surfaces, equation 1.6 can be rewritten in its one-dimensional form:

$$\frac{dq}{dy} = \dot{m}\, c_p \frac{dT}{dy} \tag{1.7}$$

Equation 1.7 will be later employed in chapter 3 for assessing the theoretical heat flux profile within the combustion chamber's wall boundary layer. In that case, the moving fluid will be represented by the engine coolant, hence $\dot{m}$ will be its mass flow rate and c_p its specific heat. [1, 2, 21]

1.2 Conventional cooling systems

The main task of a rocket engine cooling system is to ensure that the temperature of all components exposed to hot gases (such as chamber and nozzle walls or the injector plate) remains within acceptable limits, thereby preventing any thermal degradation, loss of mechanical strength or structural failure. During steady engine operation, gas temperatures can exceed 3000 K, while the allowed temperature for metallic materials used in the chamber structure rarely exceeds 1000 K. Consequently, an efficient heat management system is essential to guarantee safe and reliable engine performance.

The choice of an appropriate cooling method depends on several parameters, including the type of propellant combination, chamber pressure, mission duration, thrust level and manufacturing constraints, resulting in a complex engineering challenge where the objective is to find the right trade-off between thermal protection, mechanical robustness and mass efficiency.

All widely used systems in modern rocket engines can be divided into two main categories: the **steady-state methods**, in which the wall temperature and the heat transfer rate eventually reach thermal equilibrium, and the **transient** or **unsteady methods**, where thermal equilibrium is not achieved and the wall temperature keeps increasing during operations. Steady-state systems are generally employed in reusable or long-duration engines, where continuous operation and

high reliability are required. In contrast, transient systems are typically found in small-scale or expendable propulsion systems, where the short firing time allows higher wall temperatures without compromising safety.

In addition to these fundamental approaches, several auxiliary techniques can be implemented to enhance the overall cooling effectiveness, such as **film cooling** or the use of **insulating coatings** and **ablative materials**. These solutions are often combined in hybrid configurations to obtain a more efficient and lightweight heat management system.

In the following sections, the main cooling principles and configurations adopted in liquid rocket engines will be reviewed, with particular attention to regenerative, film and ablative cooling systems, highlighting their operational mechanisms, advantages and limitations.

1.2.1 Steady-state methods

Steady-state cooling systems are typically employed in long-duration rocket engine applications, where continuous operation requires the maintenance of chamber and nozzle temperatures within safe limits over extended periods. These systems are highly versatile and effective, being used in a wide range of applications, from medium to high-thrust bipropellant liquid rocket engines to small monopropellant thrusters for attitude control or orbital maneuvers. As previously mentioned, in this kind of systems both the wall temperature and the heat transfer rate within the combustion chamber eventually achieve thermal equilibrium, allowing the system to operate under predictable and controlled thermal conditions.

In the following sections the two main approaches commonly used to achieve steady-state cooling will be presented: **regenerative cooling**, where the propellant itself is circulated through channels in the chamber or nozzle walls to absorb heat, and **radiation cooling**, in which heat is passively dissipated from the hot surfaces to the surrounding environment.

Regenerative cooling

Regenerative cooling system consists of a dense network of channels built into the chamber and nozzle walls, through which a propellant is circulated before being injected into the chamber (figure 1.1). Since the propellant is much colder than the hot gases, it serves as an excellent heat sink, while its high velocity within the channels enhances heat transfer by forced convection. In

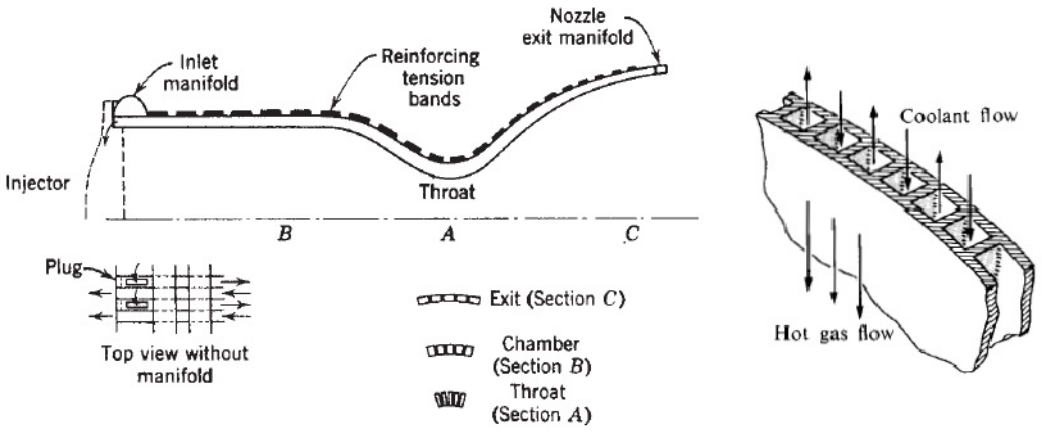

Figure 1.1: Diagram of a regenerative cooling system [1]

addition, this concept allows part of the lost energy to be recovered and returned to the system inside the thrust chamber (from which comes the term ”regeneration”). However, its effect remains very slight if compared to other applications such as steam engines. In particular, specific impulse can grow by 1% when propellants are preheated from 100°C to 200°C. Nonetheless, the effect can be much greater in small combustion chambers with a relatively large wall-surface-to-chamber volume ratio, where the temperature rise in the coolant would be higher, resulting in a specific impulse increase of over 1%. [1]

In cases involving forced convection, a key factor is represented by the **fluid film behaviour**, which depends on the difference between the wall temperature and the coolant bulk temperature. Figure 1.2 shows the heat flux trend as a function of the temperatures difference. The graph clearly exhibits four distinct film behaviours, associated with the possible onset of fluid boiling. In fact, for low temperature differences, no phase change occurs and the flow is dominated by simple forced convection (region A-B). Therefore, equation 1.2 stands and the heat flux follows a linear increasing trend. This flow regime is also referred to as **pool boiling**, as the heat is trasmitted whithin the fluid by convective currents.

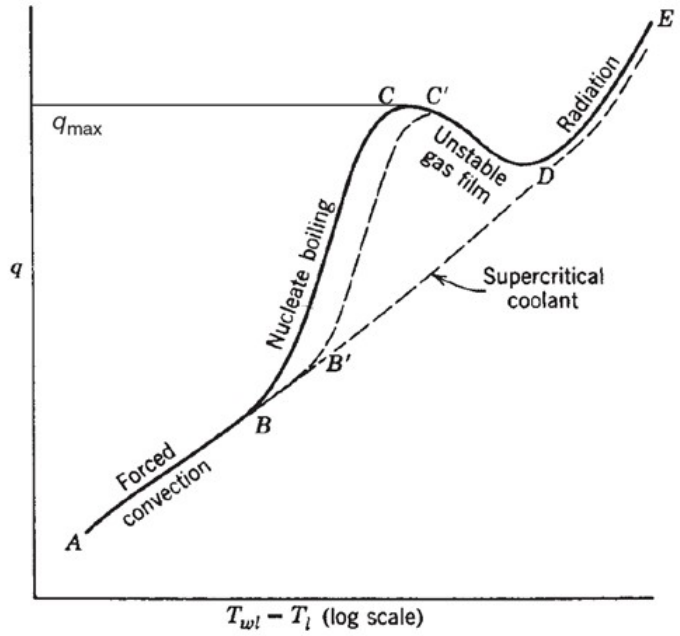

Figure 1.2: Heat flux behaviours between a wall and a boiling fluid [1]

As the temperature difference increases, the coolant starts to evaporate. Vaporization always initially occurs adjacent to the channels walls, where fluid particles can more easily equal their vapour tension to the liquid pressure (since part of the particle surface is replaced by the physical wall). Bubbles forming on the side of the wall is also known as **nucleate boiling** phenomenon (region B-C). The endothermic phase change of the substance absorbs more heat from the system, as indicated by the trend local increment, determing a more efficient cooling process. This effect is further enhanced by higher flow velocities within the channels, since the formed bubbles are more rapidly replaced by fresh fluid ready to evaporate.

When the temperatures difference is sufficiently high, the number of formed bubbles increases to the point where they coalesce, creating a dense gas film that separates the wall from the fluid freestream. For this reason the regime is known as **film boiling** (region C-D) and is characterised

by a decreasing trend of the heat flux, as heat transfer capacity is significantly reduced. At even higher wall temperatures, the heat flux increases again due to the large amount of thermal radiation emitted by the wall material.

The graph shows also an important dependence on the fluid pressure: at higher pressures, evaporation occurs at higher temperatures, since vapour tension must increase further for reaching the vaporization pressure. Moreover, as the latent heat decreases with increasing pressures, the peak of heat flux in the nucleate boiling flow regime (region B'- C') is lower than before. This effect is further amplified when the fluid reaches supercritical temperature–pressure conditions, under which it is not possible to distinguish between liquid and vapour phases and the boiling effect vanishes. [1]

The coolant passages follow the wall contour along the chamber and the nozzle, while their cross-sectional area modifies so that the number of channels remains the same in different axial positions. The coolant enters the system from an inlet manifold and flows through the passages towards the rear end of the engine. Here, fluid can either be expelled from the system through smaller nozzles (approach known as **dump cooling**), or be flown back to the injector plate through ducts similar to the initial ones. Although the second approach results in greater system's complexity, it offers performance advantages since all the available propellant is utilized to generate thrust.

The regenerative cooling system has been employed in all first-stage engines of medium- to high-thrust launch vehicles. Notable examples include SpaceX's Merlin and Raptor engines, the RL10 engine used on Atlas and Delta launch vehicles, and NASA's RS-25 engine powering the Space Launch System (SLS). In each of these cases fuel is used as a coolant, since the oxidizer could easily react with the channels material due to the high temperature.

Radiation cooling

For smaller thrusters, a regenerative cooling system would be too complex, since the channels within the wall would become too small and geometric tolerances too restrictive. In such cases, a less complex and equally effective cooling method is preferred, the radiation cooling. This approach consists in allowing the components to become incandescent and lose energy through the emission of radiations. In order to do so, the relevant engine components must protrude from the vehicle so that the emitted radiation is not reabsorbed by the structure and can be dissipated into the surroundings.

Since the cooling capacity of the approach is limited by the thermo-resistive properties of the materials, it can be employed only in applications with relatively small heat loads, such as small thrusters for in-space attitude control or apogee engines. Furthermore, radiation cooling is also implemented as the main cooling method for high-thrust vacuum engine nozzles, such as SpaceX's vacuum Merlin engine and Rocket Lab's vacuum Rutherford engine, which both rely on radiation cooling for their extended nozzle sections. In vacuum, due to the lack of atmosphere, no convection takes place, while the radiation heat transfer occurs more efficiently since there is no absorbing media. In such cases, the large, heat-resistant, niobium alloy-based nozzles can easily lose energy emitting radiations into the surroundings.

Although this method is relatively simple and lightweight, it is inherently limited to applications where the heat fluxes are moderate or where other cooling strategies would impose excessive complexity or mass penalties. For this reason, radiation cooling is typically employed as a complementary technique rather than a standalone solution in most high-performance rocket engines.

1.2.2 Transient/Unsteady methods

Transient or unsteady cooling systems are often used in small rocket engines, with small chamber pressures and heat transfer rates. In these cases, thrust chamber does not reach the thermal equilibrium, allowing the wall temperature to rise during operation. The engine can operate as long as the wall temperature remains below a critical value at which structural failure could occur. For this reason, it represents a limited durability cooling method, which depends on the heat absorption capacity of the material chosen for the structure.

The systems can be made of a fully metallic structure, built with sufficiently thick walls so that relative heat loads can be managed. Otherwise, inner layers of **ablative materials** can be added to enhance the cooling power. An ablative material is an organic substance, usually made out of carbon composite, which has an extremely high melting point and is capable of chemically reacting when being heated. Its reactions of decomposition and vaporization are endothermic and take heat away from the system; moreover, the gases produced from the decomposition can also form an additional protective film on the inner surface of the chamber.

The use of ablative materials, also known as **ablative cooling**, or insulating ones is widely diffused in solid rocket motors, such as Space Shuttle Solid Rocket Boosters (SRBs) and Ariane 5 and 6 boosters. For this type of thrusters, since it is not possible to rely on liquid propellants as a heat sink, a so called **passive cooling** method is necessary, especially for the protection of the nozzle throat, where highest thermal peaks occur. In both these cases, carbon-phenolic materials were implemented for protecting the nozzle throat, while silica-phenolic and insulating EPDM (Ethylene-Propylene-Diene Monomer) for nozzles' divergent part. [1, 2, 22]

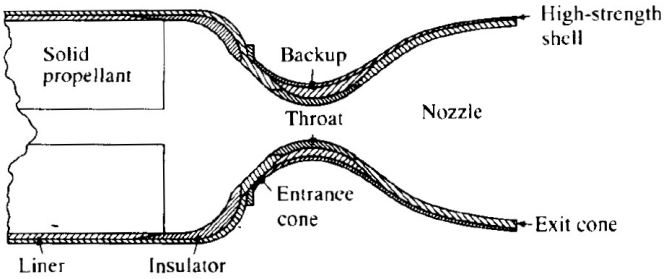

Figure 1.3: Diagram of a passively cooled solid rocket motor [2]

1.2.3 *Film cooling*

The film cooling method involves injecting a certain amount of propellant or an inert fluid, either in liquid or gaseous form, inside the chamber in a way that this could form a thin protective layer near the wall, thanks to its colder temperature.

The easiest way to produce a film cooling is by having a higher concentration of fuel or oxidizer injectors on the outer perimeter of the injector plate. This would create a locally fuel-rich or oxidizer-rich flow along the wall, which will not react with the rest of the hot flow, remaining relatively cool and preventing the heat from transferring to the chamber's walls. Otherwise, another method can be injecting the liquid tangentially to the surface through a series of dedicated orifices and coolant slots (see figure 1.3), however augmenting system's complexity and manufacturing costs. [1, 2, 22]

Usually, in liquid propelled rocket engines which implement turbopumps feed-system, film cooling is made with the injection of the turbines discharge gases rather than liquid propellants,

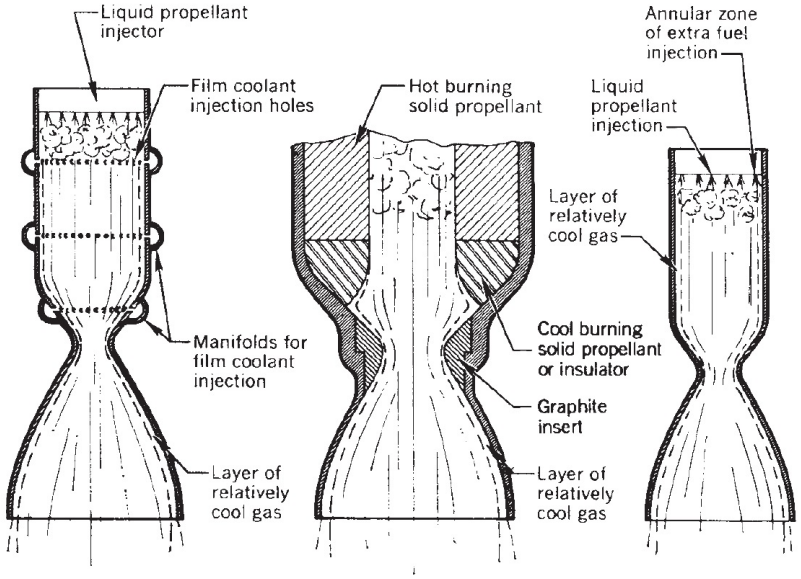

Figure 1.4: Diagrams of two possible configurations of film cooling system for rocket engines [1]

since their temperatures ranges from 400 to 800°C, thus much colder than the main chamber's hot flow. This choice found application in the Vulcain 2 engine for Ariane's launchers. In that case, the turbine exhaust gases were reinjected into the chamber for cooling the lower part of the nozzle.

Film cooling can also be employed in solid rocket motors as an auxiliary cooling method, in addition to the already mentioned passive cooling approach. The only way to make a cooler film in this case is to create a solid propellant grain with a cool burning material at the lower part. Alternatively, changing the grain's composition would give almost the same results. Intuitively, the burning of this material would produce a much colder gas that would flow along the walls, protecting them.

1.3 Hydrogen peroxide

Hydrogen peroxide is a propellant widely employed in the aerospace sector due to its numerous practical advantages and high performance. It can be used both as an oxidizer in bipropellant engines, often combined with organic fuels and hydrocarbons, and as a monopropellant, through highly exothermic catalyzed decomposition. The most adopted form for the propulsion sector is high concentration water solutions (from 70 up to 98%), known as **high-test peroxide** or **HTP**. All concentrations provided in this chapter are expressed by mass.

Before discussing its chemical behavior, it is useful to examine its physical state and thermodynamic characteristics, which determine many of its handling and operational properties. As shown by its solid-liquid phase diagram (figure 1.5), hydrogen peroxide exists in the liquid state under ambient pressure and temperature conditions, thus representing a **storable propellant**. This peculiarity reduces costs on the systems and procedures for its management and storage, since it is not necessary to reach extreme pressure conditions or cryogenic temperatures to maintain the liquid state.

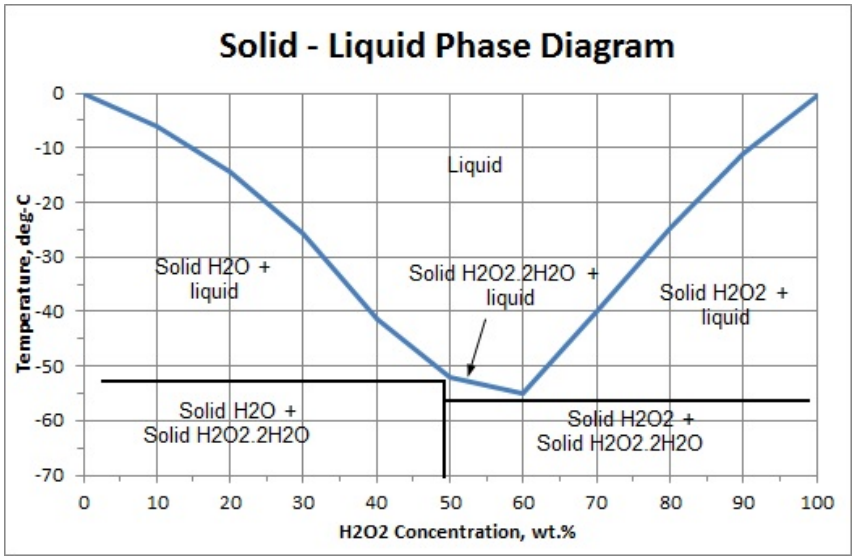

Figure 1.5: Solid-liquid phase diagram of hydrogen peroxide [3]

To better quantify these advantages, the main chemical and physical properties of hydrogen peroxide solutions at different concentrations are summarized in the table below.

Property	wt 70%	wt 80%	wt 90 %
Specific gravity (at 20°C)	1.289	1.35	1.392
Boiling point (at 1 atm)	125°C	130°C	141°C
Freezing point	-40°C	-25°C	-12°C
Viscosity (at 25°C)	1.23 mPa·s	1.25 mPa·s	1.25 mPa·s
Vapour pressure (at 30°C)	173 Pa	267 Pa	369 Pa
Decomposition enthalpy	2.887 MJ/kg	-	-
Volumetric energy density	2.6 MJ/L	3.11 MJ/L	3.6 MJ/L

Table 1.1: Hydrogen peroxide solutions (70, 80 and 90%) main physical-chemical properties

As can be observed, increasing concentration results in higher density and boiling point, thus extending the useful temperature range for storage and operation. On the other hand, the freezing point rises as well.

Hydrogen peroxide has a thermodynamically unstable molecule due to the peroxide bond and is characterised by the natural tendency to decompose, even at room temperature. When stored under such conditions, a gradual decomposition of about 1% per year is observed. Decomposition is further promoted by possible contact of the liquid with impurities such as dirt or grease, as well as with chemically incompatible materials, which will be addressed later. [23]

This delicate balance between storability and reactivity has historically limited its large-scale adoption in the propulsion sector. Only recently, with the introduction of new mixtures of higher concentration and purity, safety and performance levels have improved, ensuring better preservation of the substance's chemical characteristics.

From a chemical standpoint, hydrogen peroxide is particularly interesting because of its dual nature. The distinct chemical structure of the molecule allows it to act both as an oxidizing and as a reducing agent (due to the peculiar oxidation state of the oxygen atoms, –1), depending on the pH value of the solution.

The reaction of decomposition is:

$$H_2O_2 \rightarrow H_2O + \frac{1}{2}O_2 + \text{heat} \tag{1.8}$$

It involves a strongly exothermic reaction, whose products are relatively harmless, consisting of superheated steam (the adiabatic decomposition temperature exceeds 1200 K) and gaseous oxygen, with no formation of toxic substances such as unburned hydrocarbons or nitrogen oxides. For this reason, it is classified among the **green** propellants of current interest in the aerospace field.

Decomposition is very slow in natural conditions, but can be accelerated by increasing concentration and temperature, eventually becoming potentially explosive when a critical temperature is exceeded (near the boiling point). Another important effect is given by the employ of a wide range of **catalysts**. These can be heterogeneous (e.g. silver, gold, iron, platinum and manganese oxides), homogeneous (e.g. iodide, iron ions and liquid permanganates) or enzymes (e.g. catalase). The catalyst can initiate decomposition, which can subsequently become self-sustaining due to the large amount of heat released.

In addition to its chemical activity, hydrogen peroxide also exhibits favourable physical characteristics for propulsion applications. Its relatively high density represents an additional advantage, as it secures high volumetric performances, i.e. a large energy output coupled with a relatively low mass of all systems involved.

As previously mentioned, in the aerospace and propulsion fields, it can be employed as a **monopropellant**, serving as a green alternative to monomethylhydrazine (MMH). A 90% hydrogen peroxide solution can provide a specific impulse of up to 180 s in vacuum conditions, which is lower than hypergolic hydrazine, but remains a viable option for its high energy density and overall lower costs (the higher costs of hydrazine are mainly due to its high toxicity and hazards).

Moreover, hydrogen peroxide can be used as a liquid **oxydizer** in bipropellant propulsion systems, alongside with one of several available fuels. In these cases, a conventional igniter can be adopted, otherwise a peroxide catalyst can be used to achieve an almost hypergolic combustion. Alternatively, hydrogen peroxide also produces hypergolic combustion when combined with hydrazine. [23] Table 1.2 reports the performance of some examples of liquid bipropellant combinations in which H_2O_2 acts as the oxidizer. Due to its high **reactivity**, hydrogen peroxide requires special attention in the selection of materials with which it comes into contact, as many surfaces can promote its uncontrolled decomposition. The choice of materials throughout the substance's entire lifecycle is based on a series of very rigorous chemical compatibility tests.

Vacuum expansion, p_c = 1000 psia, ϵ = 40						
Oxidizer	Fuel	I_{sp}	r	T_c	d	c^*
H_2O_2	MMH	336.8	3.69	2980	1.24	1714
	N_2H_4	337.6	2.12	2918	1.25	1744
	N_2H_4 - Be	403.5	0.57	3371	1.24	1940
	B_5H_9	371.5	2.09	2870	1.01	1817

Table 1.2: Examples of liquid propellant combinations in which H_2O_2 acts as the oxidizer; I_{sp} = specific impulse [s]; r = mixture ratio; d = density [g/cm^3]; T_c = chamber temperature [F]; c^* = characteristic velocity [m/s] [21]

[24] The **compatibility** of a material is determined by its ability to withstand chemical attack by the propellant, in the form of corrosion, as well as by the **stability** of the substance itself upon contact with the material. The stability of hydrogen peroxide with a given material is assessed by measuring the active oxygen loss (AOL) during a 24-hour test, expressed as a percentage.

Hydrogen peroxide has been investigated regarding its compatibility with different materials since the early 1930s, but lack of set-up description, incomparability of test setups and investigated probes often led to inconclusive or even contradictory results. More modern experimental evaluations (such as the one from reference [25]) have shown that all materials can be classified based on their chemical compatibility with hydrogen peroxide into 4 categories or classes [25, 26]:

- **class 1**, materials that can withstand a long-term contact with the substance, ensuring the preservation of its chemical-physical properties. This category includes all materials used for propellant storage.

  Examples (AOL datas given in % per month at 30°C): Aluminum alloys (1060 (0.3), 1160 (0.4), 1260 (0.4), 5254 (1.5), 5652 (1.5)), tantalum (-), PTFE (Teflon) (-);

- **class 2**, materials that allow repeated short-term contact (less than 4 hours at 72°C or 1 week at 22°C), used for all propellant management systems related to its storage or for the use itself, such as valves and pumps in the feed systems.

  Examples (AOL datas given in % per month at 30°C): Aluminum alloys containing bronze (6061 (1.3), 6063 (1.6), 5054 (-), 5056 (1.5), 6363 (1.6)), stainless steels (AISI 300 to 321 (1.5)), silicone (30 per week at 66°C), tin (0.6 per week at 66°C);

- **class 3**, materials that can withstand only brief contact with hydrogen peroxide (1 minute at 72°C or 1 hour at 22°C). After contact, the substance must be used or discarded and cannot be further stored, as it has lost a significant portion of its chemical properties.

  Examples (AOL datas given in % per week at 66°C): Aluminum alloys (2024 (16.4)), stainless steels (AM 350–355 (7.8), 440 C (2.5 per month at 30°C));

- **class 4**, materials incompatible with H_2O_2 because they induce excessive decomposition even after brief contact.

  Examples (AOL datas given in % per week at 66°C): Aluminum alloys (7075 (100), 2017 (100)), pure metals (beryllium, cadmium, chromium, cobalt, bronze, gold, iron, magnesium, manganese, mercury, molybdenum, nickel, platinum, silver, tungsten, zinc) (100).

In addition to material compatibility, hydrogen peroxide also poses a risk for human safety due to its strong oxidizing effect. Its vapours are relatively low in toxicity compared to those of other propellants, given its very low vapour tension. On the other hand, contact with high concentrations mixtures can cause severe skin burns and irritations. Upon contact, peroxide can decompose, releasing high-energy gases capable of igniting fuels and other materials, like clothing. For these reasons, this propellant still requires careful handling and the possess of appropriate protective equipment.

In table 1.3 some information regarding hydrogen peroxide's safety are provided. [27, 28, 29, 30]

NFPA 704	Health risks 3^a	Flammability 0^b	Stability 3^c	Special effects OX^d

Acute toxicity - Oral	Category 4
Acute toxicity - Inhalation (vapours)	Category 4
Skin corrosion/irritation	Category 1 (Sub-category A)
Serious eye damage/eye irritation	Category 1
Specific target organ toxicity (single exposure)	Category 3
Oxidizing liquids	Category 1

LD50 Oral	70% solution: 1026 mg/kg bw
LD50 Dermal	70% solution: 9200 mg/kg bw
LC50 Inhalation	50% solution: $>$ 170 mg/m^3

[a]Can cause serious or permanent injury; [b]will not burn under typical fire conditions; [c]normally stable but can become unstable at elevated temperatures and pressures; [d]possesses oxidizing properties.

Table 1.3: Information regarding hydrogen peroxide's safety

1.4 *Transpiration cooling*

As it was mentioned above, all active cooling systems which use a propellant as coolant, such as regenerative and film cooling, usually employ fuel as their cooling liquid. The main reason for this choice is that an oxidizer is more likely to react when exposed to high temperatures and could oxidize regenerative cooling channels or the nozzle walls. However, there are cases where the amount of fuel available for the engine operation is not enough for considering also the usage for a cooling system. This could happen in rocket applications with high **mixture ratio** (MR) values, which is the ratio between the oxidizer and the fuel mass flow rates. As an example, the combination of propellants ethanol-HTP has a stoichiometric mixture ratio of 4.922, meaning that fuel's mass flow rate can not manage the heat transfer insider chamber. In such cases, using oxidizer as coolant remains as the only way, although requiring inevitable adjustments in the cooling system choice process.

A conventional cooling system such as regenerative cooling, which relies on circulating the propellant through narrow internal channels, would not be suitable for hydrogen peroxide-propelled engines due to the material compatibility issues and the high risk of vapour detonation. In addition, the exothermic decomposition would significantly increase the risk of localized overheating and potential structural failures inside the channels. As seen in the previous section, high-concentration H_2O_2 mixtures are highly reactive with most common high-conductivity metals, such as copper, nickel and iron. This makes the choice of a cooling strategy really challenging.

Although film cooling still stands as possible solution, a more promising approach to address this challenge is **transpiration cooling**, a technique that utilizes a porous wall to inject coolant directly into the hot gas flow, forming a protective boundary layer that significantly reduces thermal loads on structural components. The transpiration of coolant allows also a more uniform surface cooling and reduces peak thermal stresses.

The availability of porous light-weight high-temperature materials is making transpiration cooling a viable solution for future re-usable rocket thrust chambers, aiming for a cheaper access to space. [31]

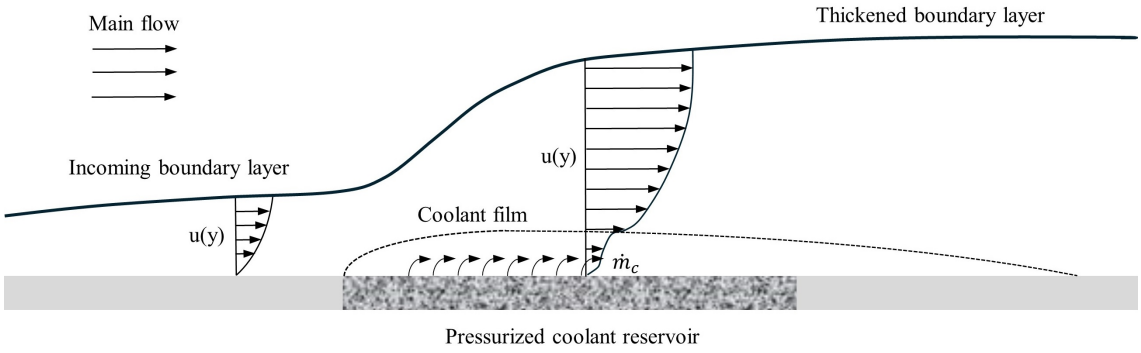

Figure 1.6: Operation scheme of a transpiration cooling system

In figure 1.6 a schematic of the transpiration cooling system operation is given. The pressurized coolant (coolant mass-flow rate $\dot{m}_c$) flows adjacent to the porous chamber enclosed by an outer shell, similar to the one used for the film cooling technique. [21] It is afterwards injected into the main flow's boundary layer through the permeable wall, cooling the structure through convection as it passes through it. Within the wall, a very efficient heat exchange takes place, thanks to the very small diameter of the channels. Furthermore, the boundary layer is thickened by the coolant injection, making the velocity and temperature gradients near wall smaller. Thus, the wall heat transfer and the skin friction is significantly reduced, as well as the total drag of the chamber. [25] As the coolant is injected at the liquid state, the liquid film subsequently evaporates absorbing a wide amount of heat (process known as **evaporative-transpiration cooling**). [31]

Hence, this cooling approach acts through multiple ways. The coolant firstly extracts heat from the wall by convection as it permeates through it, subsequently provides a protective film on the hot-gas side, while the endothermic evaporation of the liquid assists subtracting heat from the system.

In addition, liquid coolant is continuously renewed and, unlike discrete film injection, it is uniformly distributed over the surface, ensuring a more homogeneous thermal protection of the chamber. [31] It is also worth noticing that the more efficient coolant distribution in transpiration cooling lowers the general coolant-flow requirements compared to other cooling approaches. [21]

An important parameter used to characterise the transpiration cooling process is the **blowing ratio** (F), i.e. the ratio between the mass flow rate of the coolant transpired through the wall and the main flow's one:

$$F = \frac{\rho_c u_c}{\rho_g u_g} \tag{1.9}$$

where ρ_c and u_c are respectively the coolant's density and velocity, while ρ_g and u_g are the main flow's ones. By changing the geometry of the pores, the wall's porosity changes, resulting in a variation in the blowing ratio which has substantial consequences on the cooling performances.

Usually, in film and transpiration cooling, the cooling efficiency is quantified by the pressure (p_c/p_g) and temperature ($(T_g - T_w)/(T_g - T_c)$) coolant-to-hot-flow ratios, since they express a thermal capacity of the system. [32] The cooling efficiency can also be implemented for assessing the convective heat transfer between the mainstream and the chamber wall:

$$q_w = h\,(T_g - T_w) = \eta\,h\,(T_g - T_c) \tag{1.10}$$

where h is the conductivity, T_w is the wall temperature and η is the cooling efficiency. As

shown by the formula, the higher the cooling efficiency, the lower the wall's temperature.

The production of high-quality, accurate and thermal-resistant porous components can be achieved through several manufacturing processes. Among them, **powder metallurgy** is an applicable way for obtaining permeable structures by using any metal which can be reduced to a fine powder. The powder is mixed with a binder and occasionally with a space holder, then deposited into a mold of desired shape and compressed with a pneumatic or hydraulic press. With the mold been removed, the so called **green body** is afterwards sintered in a furnace at a specific temperature for a certain period, depending on the material used. [31]

In this process, the achieved porosity can be controlled by varying the powder or the space holder particles dimension, the percentage of binder or the compression pressure. As an alternative to the powder form for sintering applications, also metal fibers and wires can be employed, creating a mesh which would be equally sintered.

Other than thermal resistant, the chosen material for the fabrication of the porous wall must also be corrosion and erosion resistant to the specific propellant, as well as resistant to thermal shock. [31]

Alternatively, **additive manufacturing** (**AM**) is emerging as a good trade-off for producing complex porous structures with high precision and low costs, characterised by high mechanical strength and reduced overall mass. Different AM technologies can be employed, such as selective laser melting (LSM), inkjet or binder jetting. However, this manufacturing technique still lacks of comprehensive design guidelines regarding porous structures, representing a barrier to its large-scale adoption. [33]

Regardless the numerous advantages hereby enumerated, transpiration cooling has not found yet wide adoption among cooling techniques, mainly due to the technological difficulty associated with manufacturing precise porous components with uniform porosity and complex geometry. This research aims to address this problem by developing a generalized framework for the design, manufacturing and performance characterisation of additively manufactured and powder sintered porous components for transpiration cooling in rocket engine applications.

Chapter 2

500 N HTP/Ethanol bypropelled rocket engine

In this research, the feasibility of applying transpiration cooling to the combustion chamber of a hydrogen peroxide–propelled rocket engine is evaluated through the firing test of a small laboratory-scale demonstrator. The investigated engine is a modified version of an existing design, which was previously operated using high-concentration hydrogen peroxide as the oxidizer and kerosene as the fuel, delivering up to 500 N of thrust.

The baseline configuration of the original engine featured a conventional layout, with all components made of stainless steel to ensure compatibility with high-test peroxide. The oxidizer was injected through an injector plate at the top of the engine and directed across the catalyst bed, where the decomposition of hydrogen peroxide occurred. Downstream of the catalyst section, the fuel was injected normally to the chamber wall to promote mixing and combustion. The subsequent combustion took place in a simple, cylindrical combustion chamber and the hot gases were then accelerated through a conventional nozzle.

In its initial design, the engine relied solely on film cooling to protect the combustion chamber. Hydrogen peroxide, used as a liquid coolant, was tangentially injected downstream of the injector assembly to form a thin protective layer along the chamber wall.

For the current experiment, the original configuration has been slightly modified to accommodate the new cooling concept. First of all, the redesigned engine will be powered by **90% high-test hydrogen peroxide** as the oxidizer and **70% ethanol–water solution** as the fuel, replacing kerosene used in the previous setup. This substitution was made for compatibility reasons between the fuel and the existing sensors, such as thermocouples, pressure transducers and the mass flow meter. In addition, the new configuration incorporates a transpiration cooling system directly integrated into the structure of the combustion chamber, completely eliminating any other cooling method. As explained in chapter 1, hydrogen peroxide is transpired through the wall into the chamber and serves as a coolant. In fact, due to high mixture ratio value, fuel's mass flow rate would be too low to adequately cool off the engine's wall.

Apart from the modified chamber design, the overall geometry and dimensions of the engine remain unchanged, ensuring that the comparison with the previous configuration focuses solely on the performance and effectiveness of the new cooling approach. However, as will be explained in more detail later, the integration of the new cooling system will make the final configuration slightly longer than the original one, effectively changing the overall combustion performances.

Furthermore, similarly to the previous configuration, the new engine does not include an ignition system, relying only on the spontaneous reaction between hydrogen peroxide

and ethanol. For activating this reaction, a **manganese-based catalyst** (chemical formula: $MnO_2/PbO/Al_2O_3$) is employed within the catalyst bed. A detailed description of the catalyst and its synthesis procedure will be provided later in this chapter.

In the table below are listed the main data of the experimental demonstrator:

Fuel	70% ethanol
Oxidizer	90% wt HTP
Mixture Ratio (MR)	4.9223
Equivalence Ratio (φ)	1 (stoichiometric)
Thrust	500 N
Chamber pressure	To be computed
Chamber temperature	2627 K
Tanks pressure	To be computed
Cooling method	Transpiration (HTP)
Coolant pressure	To be computed
Fuel mass flow rate	0.0341 kg/s
Oxidizer mass flow rate	To be computed
Coolant mass flow rate	To be computed

Engine	
Total length	$\sim$200 mm
Maximum diameter	100 mm
Chamber and Nozzle	
Nozzle's throat diameter	13.4 mm
Nozzle's exit diameter	26 mm
Nozzle's length	50 mm
Chamber's diameter	48 mm
Chamber's length	60 mm

Table 2.1: 500 N HTP/Ethanol rocket engine main data

This chapter provides a detailed description of the engine's overall geometry, outlining the main components and their respective functions. This will also include a description of the catalyst synthesis procedure and the design of the new combustion chamber equipped with the transpiration cooling system, along with the design requirements and project constraints that guided its development.

2.1 Description of the engine's original configuration

The original laboratory-scale HTP/Kerosene rocket engine implements a very simple yet efficient configuration, conceived for testing the cooling performances of a film cooling system in which hydrogen peroxide was injected as the coolant. Its layout was conventional, featuring two separated injector systems for the two propellants, a catalyst bed, a cylindrical combustion chamber and a supersonic nozzle. The engine was designed to be modularly assembled, with each component manufactured as an independent part and connected to the adjacent ones through flanges and standard fastening elements such as bolts and nuts. This design philosophy offered

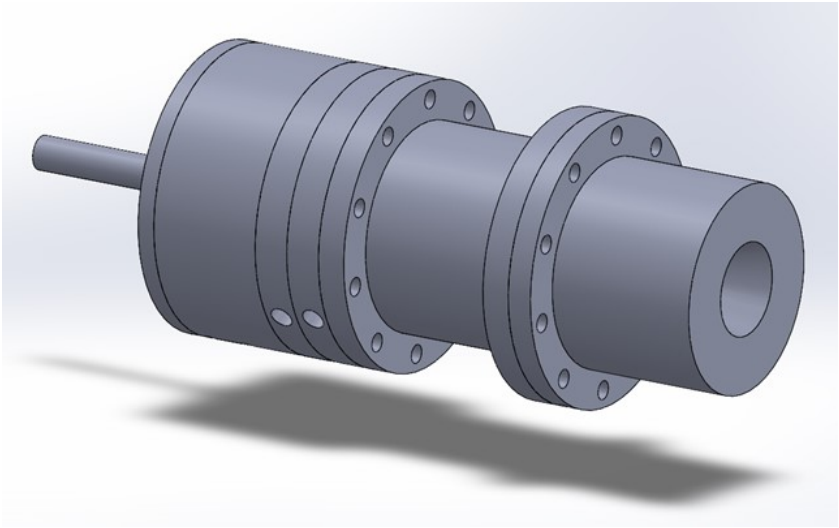

Figure 2.1: 500 N HTP/Kerosene laboratory-scale rocket engine

several advantages, such as great ease of production, assembly and maintenance. However, to prevent any form of leakage at the component junctions, each part is equipped with grooves designed to host sealing elements.

The modular architecture also provided great flexibility during experimental campaigns, allowing individual subsystems to be replaced, modified, or redesigned without the need to rebuild the entire engine. This approach significantly reduced preparation time between test sessions and facilitated the investigation of different design solutions. In particular, this feature made it possible to replace the existing cooling method and to implement the new transpiration cooling system into the layout, without the need to redesign an entirely new combustion chamber. Furthermore, the clear mechanical separation between components simplified troubleshooting and post-test inspections.

In the following sections, a detailed description of the original engine configuration is presented, dividing the full system into three main components groups, the **injection system**, the **cooling system** and the **thrust chamber**, and explaining for each one the main functional features, geometrical characteristics and operating principles. In figure 2.1 a first view of the engine can be seen.

Injection system

The engine operation begins with the injection of the two propellants from two separated injection systems. An exploded view of this first part of the whole system is shown in figure 2.2. Hydrogen peroxide enters the system from the left end (indicated as H_2O_2 entry). An 8 mm diameter propellant supply main manifold is connected to this flange by a leak-proof, hydraulic threaded fitting.

On top of the flange, a shower-head type injector plate is placed. The plate has a thickness of 2 mm, an overall diameter of 46 mm and it is featured with several 0.4 mm injection holes, distributed along eight equidistant radial lines. The propellant is instantly atomized due to the pressure drop experimented across this passage, given the small dimension of the injector plate holes.

The so nebulized propellant then flows across the catalyst bed where hydrogen peroxide would react and hence decompose. As it was mentioned before, the engine lacks of an ignition

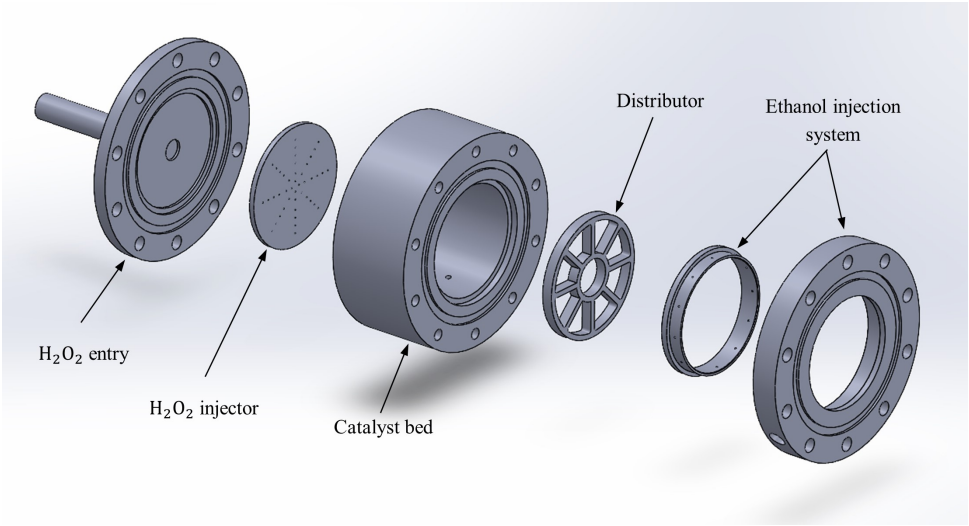

Figure 2.2: Exploded view of the engine's injection system

system, relying only on the spontaneous reaction of hydrogen peroxide with the chosen catalyst. The latter's particles are kept from flowing downstream by a thin metallic wire mesh, supported by a thicker structure called distributor. The catalyst bed has a cylindrical shape, with an overall length of 28 mm and a diameter of 42 mm.

The fuel is injected separately from an injector ring, located right after the distributor and secured by a flange. Fuel is laterally supplied by its main manifold through a lateral port of the flange, it flows inside a small annular gap between the injector ring and the flanges, before being injected and mixed with oxidizer. The injector ring is featured with twelve 0.6 mm equally distributed injector holes, which atomize the propellant as it passes through. Thus, an high-momentum gas flows axially, while the liquid fuel is sprayed transversely, promoting efficient mixing and subsequent combustion.

Cooling system

The original film-cooling configuration of the rocket engine consisted of a two-component assembly, comprising an injector ring and a flange. This unit was installed between the kerosene

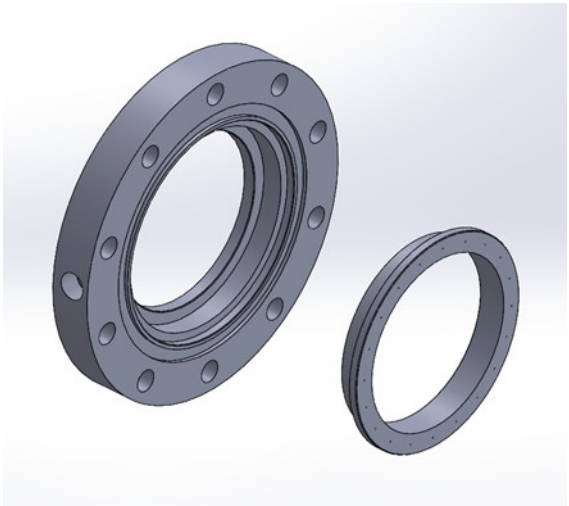

Figure 2.3: Exploded view of the engine's original film cooling system

injector system and the combustion chamber and has an overall thickness of 10 mm.

The coolant is injected tangentially along the chamber wall through a series of 0.3 mm diameter orifices distributed uniformly around the circumference of the injector ring. Each orifice is positioned approximately 0.5 mm from the inner wall, allowing the coolant film to enter directly into the hot-gas boundary layer and form a protective layer that reduces convective heat transfer to the chamber wall.

Prior to injection, the coolant is supplied laterally from a secondary manifold into the annular gap formed between the flange and the injector ring. This space ensures a uniform pressure distribution along the ring and promotes consistent mass flow through all orifices. The general configuration and flow path closely resemble those used in the fuel injection system, allowing the cooling flow to be easily integrated into the overall propellant feed architecture.

Thrust chamber

Overall, The chamber-nozzle assembly forms the thrust chamber unit of the engine, where oxidizer and fuel react and the resulting high-temperature gases are expanded to produce momentum. This unit consists of a simple cylindrical combustion chamber and a supersonic nozzle. The chamber has an internal diameter of 48 mm and a total length of 60 mm, giving a length-to-diameter ratio (L/D) of approximately 1.25. The supersonic nozzle has a very simple shape as well, with both the convergent and divergent sections realized as simple conical flanks. The overall nozzle length is 50 mm, the throat diameter is 13.4 mm and the exit diameter is 26 mm, resulting in an **area ratio** (ε) of about 3.76.

Such compact and regular geometry supports repeatable manufacturing and straightforward assembly, which are desirable attributes for a laboratory-scale demonstrator intended for comparative testing. The cylindrical chamber provides a consistent cross-section for the mixing and combustion processes, while the conical nozzle gives predictable expansion behaviour of the hot gases produced in the chamber. It can also be considered the already mentioned film cooling assembly to be part of the thrust chamber, since combustion starts occurring at that point.

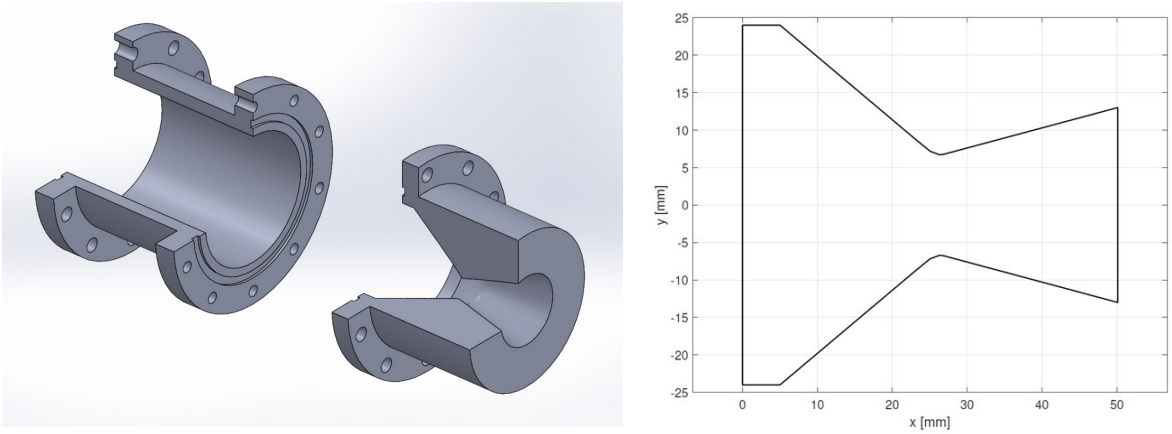

Figure 2.4: (left) Exploded view of engine's thrust chamber; (right) nozzle's contour

2.2 New combustion chamber configuration

The design process of a new combustion chamber was driven by the need to integrate the transpiration cooling, replacing the original film cooling system. The modular configuration of the engine permits easy substitution of these components within the assembly. However,

the slight difference in length between the two systems will modify the original overall thrust chamber length, thus effectively altering, even though in small portion, the engine's combustion performances.

The new chamber's design is intended to incorporate a **porous wall** through which the coolant transpires. The propellant is introduced via a lateral injector and flows along the outside of the porous wall, within a circumferential manifold formed between the porous structure and an external metallic **housing**, similarly to the previous film cooling arrangement. The new geometry shall meet these requirements, in addition to the possibility of inserting thermocouples for measuring the wall's temperature in different locations and depths.

Integrating a new component into an existing configuration inevitably imposes geometric constraints. The chosen shape for the porous wall is cylindrical, matching the main chamber, with an inner radius of 24 mm and a total length of 18 mm. Its thickness may vary, depending on the material porosity and the desired cooling capacity. A higher thickness would cause a higher pressure drop within the wall and would hinder coolant flow, while a thinner wall facilitates a greater coolant flow into the chamber. This geometry promotes a more efficient and homogeneous cooling effect over the entire chamber's lateral surface. Furthermore, the simple shape facilitates the manufacturing process, allowing greater flexibility for later possible adjustments.

To sum up, the new transpiration cooling system would consist of three separate components, the porous wall, a metallic housing and a cover. The unit would merge with the rest of the engine's configuration and can be implemented either upstream or downstream of the existing chamber. This choice permits reuse of the existing chamber body without the need for fabricating a replacement. Additionally, it leads to a more elastic design which can be adjusted whereas the objective is to cool down the chamber the nozzle.

Externally, the whole system has a very simple, cylindrical shape that guarantees a more straightforward production process. Additionally, the extra material would act as a heat sink during experimental operations. The housing and the cover parts are joined by six 5.2 mm through-holes, while ten blind M4 threaded-holes allow to connect the cooling module with the rest of the engine. Sealing features prevent any sort of coolant leakage from the engine. At each joint a small groove is provided to host a copper O-ring. Even though copper is generally incompatible with hydrogen peroxide, the propellant will already have decomposed and would not react further. In addition, highly ductile and soft copper can adapt to the groove geometry, covering the whole space and avoiding propellants losses. For the cooling system, since the propellant is still in the liquid form and shall not react before entering the combustion chamber, Teflon (PTFE, class 1 hydrogen peroxide-compatible) seals and O-rings shall be used. Accordingly, a PTFE sheet is inserted at the top and the bottom of the porous wall, avoiding fluid passages towards the chamber. All grooves were designed in compliance with the DIN ISO 3601-2 standard for axial-face sealing. The standard requires that, for applications where greater pressure is acting from the inside surface of the seal toward the outside, the outer diameter of the groove and the outer diameter of the seal shall be equal.

Finally, lateral holes for thermocouples insertion and the main peroxide injector are added to the housing design. The thermocouples are placed and welded into four 3 mm smooth holes arranged in an X pattern, forming a 36° angle with each other. The injector hole is similarly integrated into the system, having a greater diameter of 6 mm.

Figures 2.5 shows a first cut-view of the new thrust chamber assembly, while 2.6 and 2.7

show the designs for the new components.

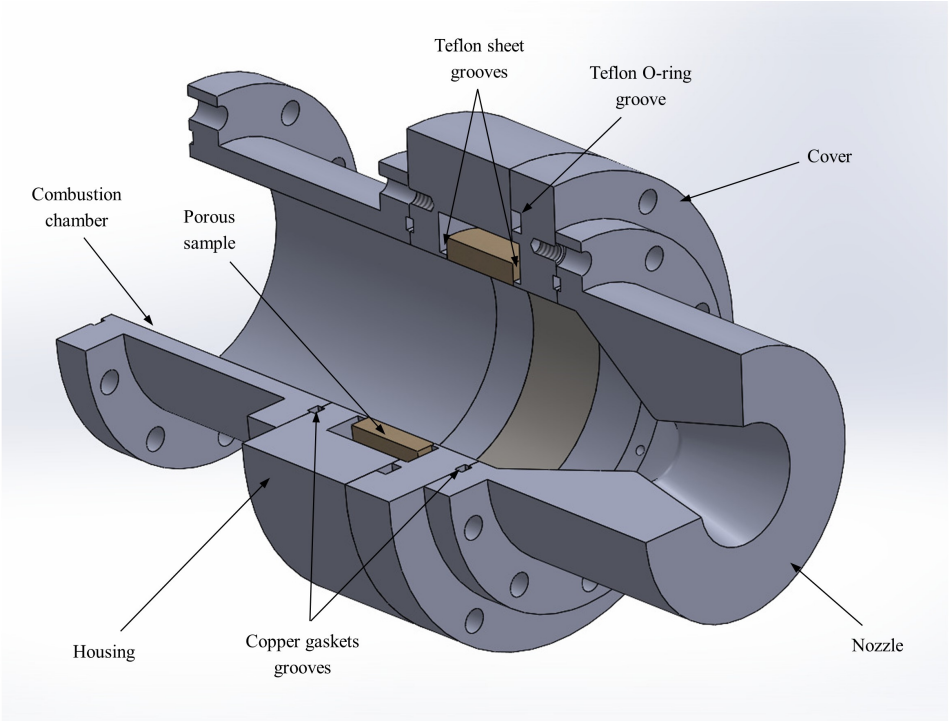

Figure 2.5: Sectional view of the engine with the transpiration cooling components

Both the housing and the cover parts were manufactured at the TU Dresden Aerospace Engineering Department laboratory by casting and turning processes. Final results are shown in figures 2.8 and 2.9. Meanwhile, the porous cylinder was manufactured by TU Dresden's partner Fraunhofer IWS, using an advanced additive manufacturing process called **Laser Powder Bed Fusion** (**LPBF**). This process generally allows the fabrication of accurate structures by selectively melting thin layers of metallic powder with a high-energy laser beam on a build platform. Layer thickness and scanning parameters can be precisely controlled, which makes the LPBF process particularly suitable for producing fine lattice structures or components with complex internal geometries. In this case, the porous walls were created by repeating an elementary cubic cell with a central hole, thus forming a porous lattice. Two examples were produced by Fraunhofer IWS, with respective cell dimensions of 1 mm and 0.7 mm and porosities ranging between 30 and 40%. The porous cylinders have an external diameter of 62 mm and a thickness of 7 mm. An image of the manufactured component is shown in figure 2.10.

An equally effective method for manufacturing highly precise porous components could be **powder metallurgy**, as detailed in chapter 1. This technique enables great control over porosity by changing powder particles dimension and compaction strength, while maintaining a certain degree of geometric flexibility since the component is formed by pressing powder into a mold of desired shape. However, this procedure was not explored in this research mainly due to time constraints.

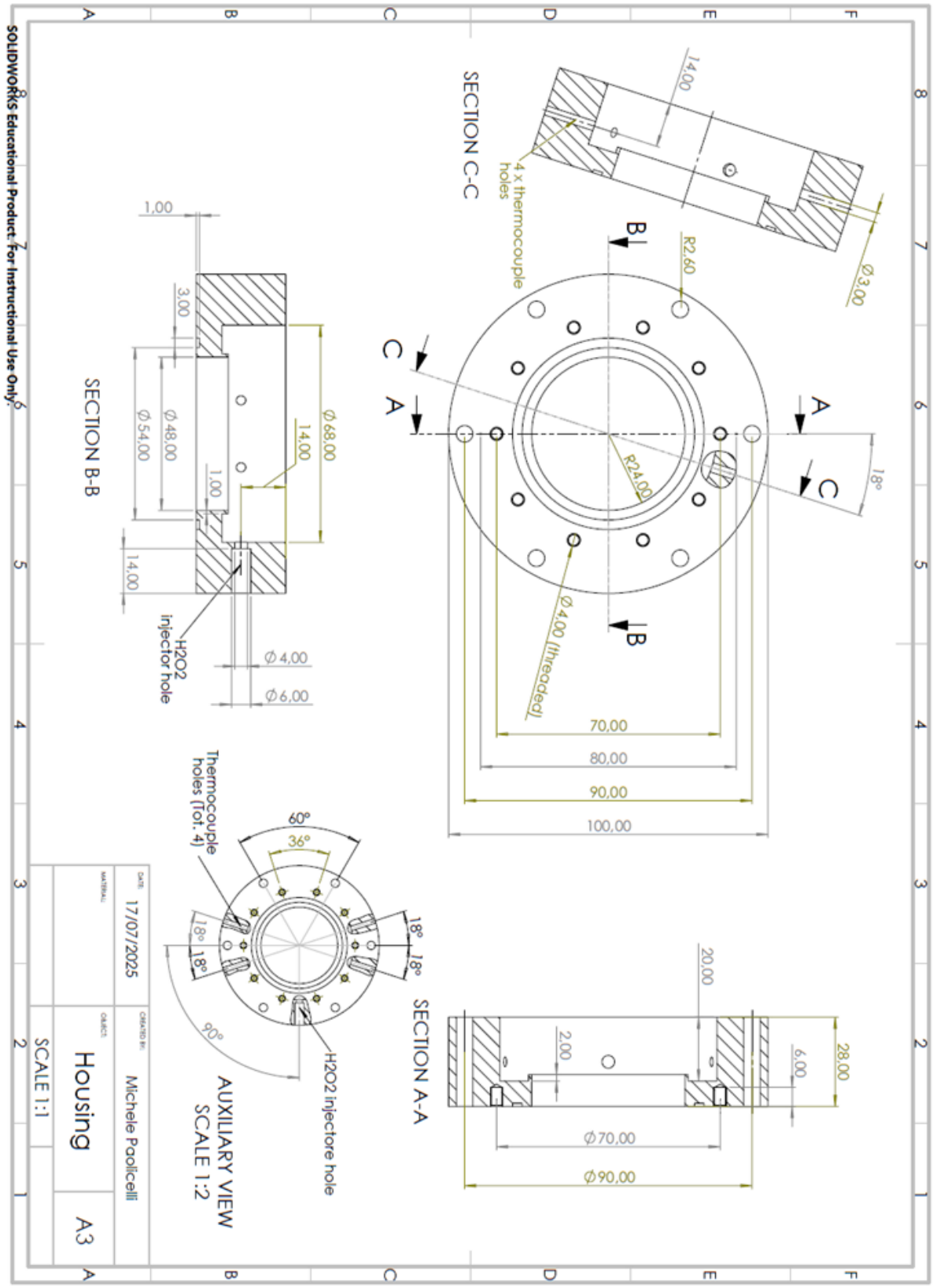

Figure 2.6: Housing part design

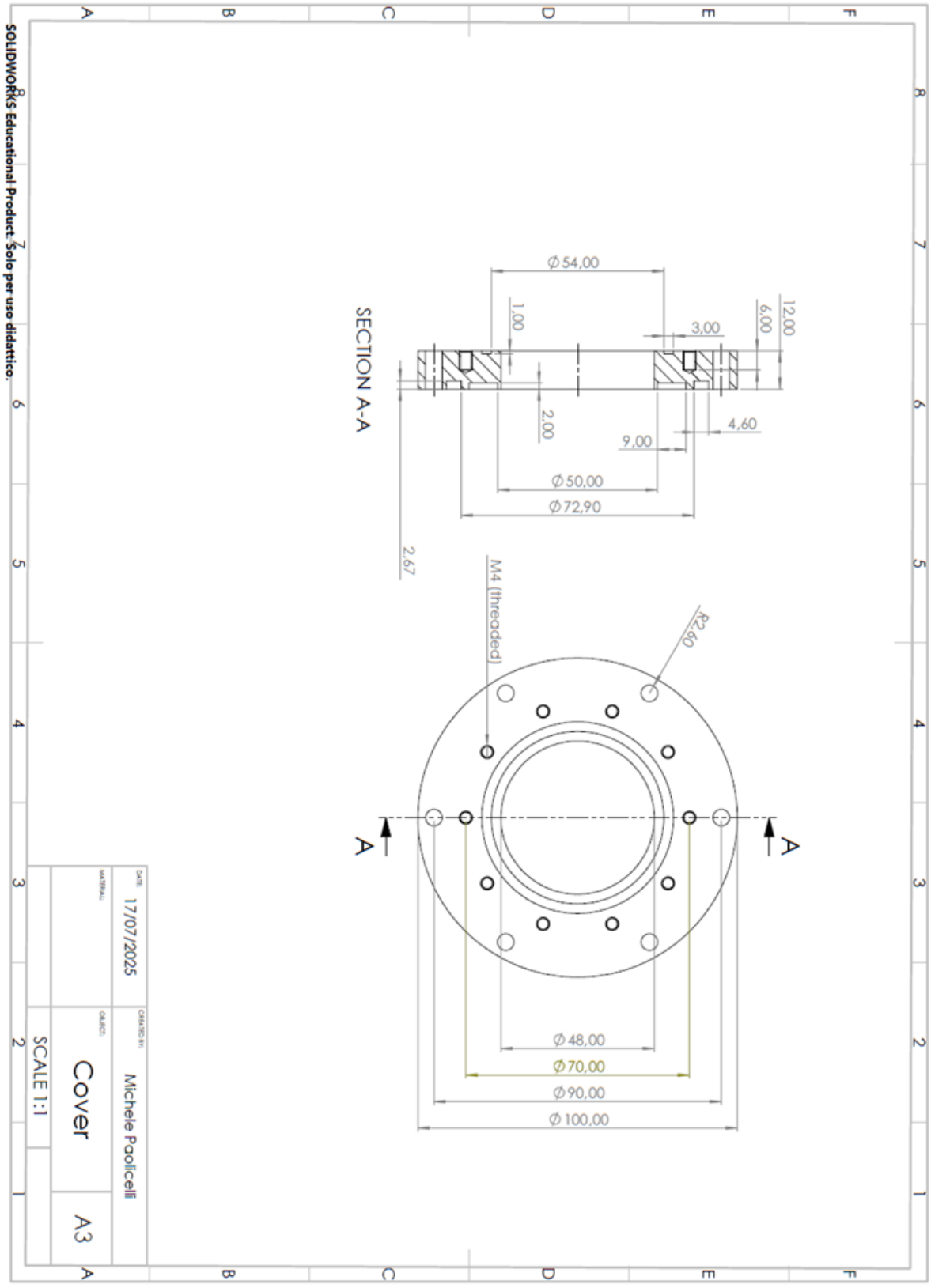

Figure 2.7: Cover part design

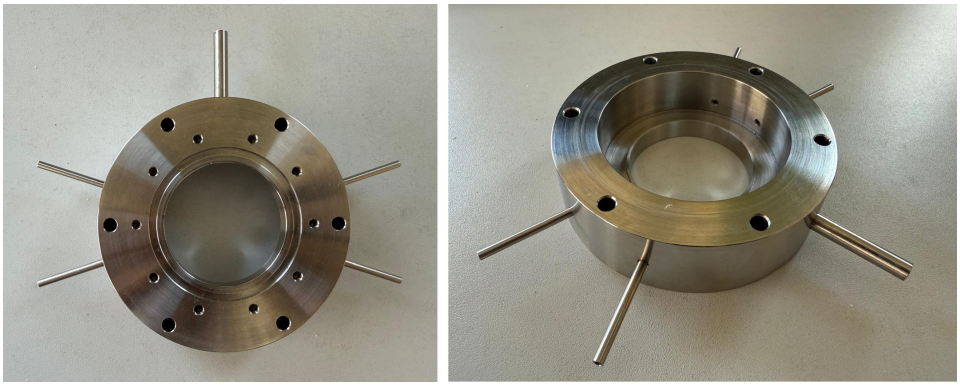

Figure 2.8: Housing part

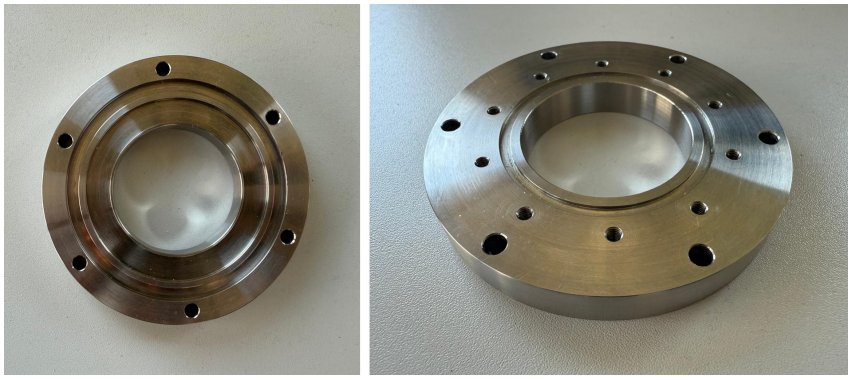

Figure 2.9: Cover part

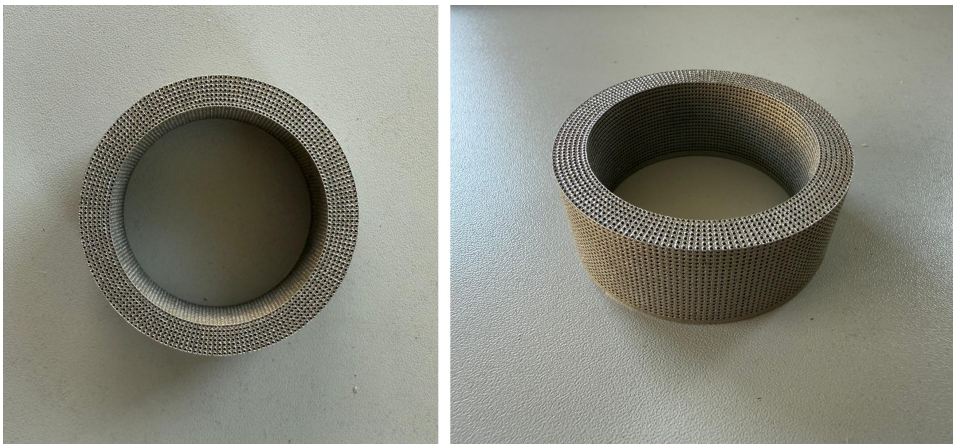

Figure 2.10: Fraunhofer IWS's porous cylinder

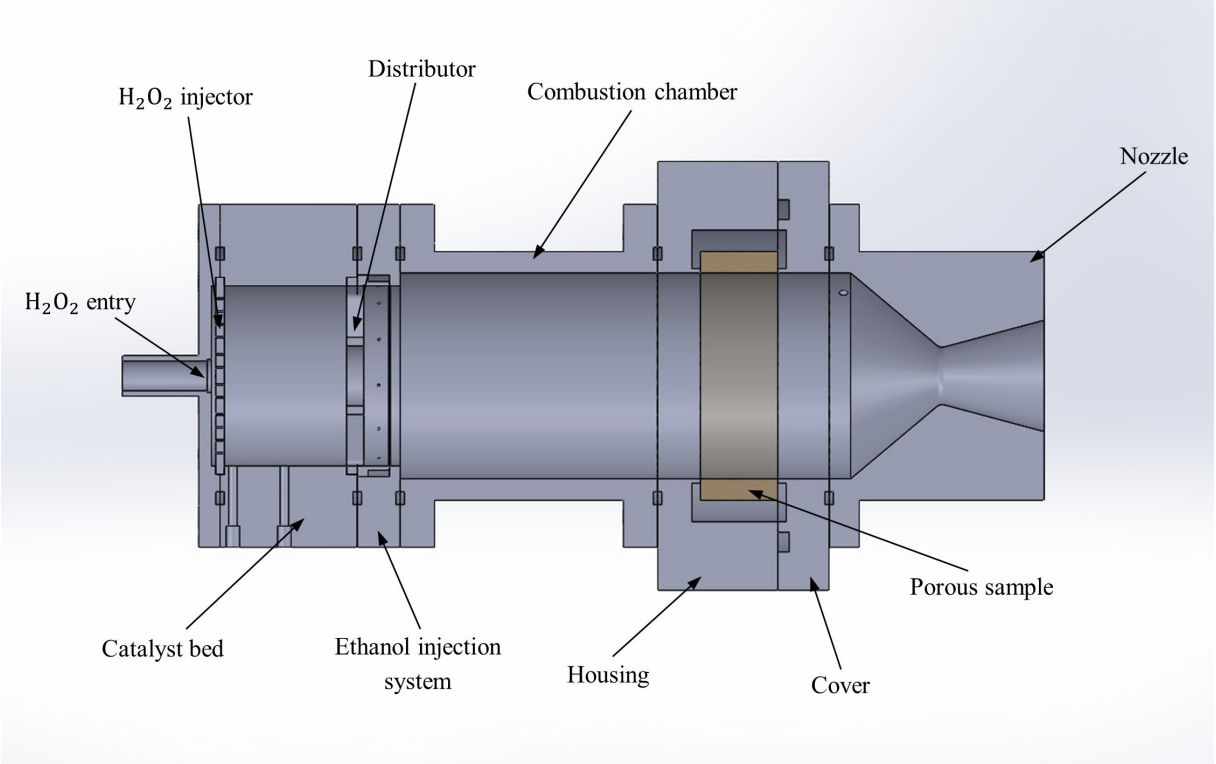

Figure 2.11: Engine's new configuration full assembly

2.3 Catalyst synthesis process

One of the most significant advantages of hydrogen peroxide as a monopropellant is the possibility of initiating its highly exothermic decomposition without the need for an external igniter or dedicated starting system. This feature relies solely on the chemical reactivity of hydrogen peroxide when brought into contact with suitable catalytic materials, resulting in simpler propulsion systems capable of multiple restarts.

Since its discovery in the early nineteenth century, numerous substances capable of promoting the catalytic decomposition of hydrogen peroxide have been identified. All materials classified as Class 4 hydrogen peroxide–compatible materials and listed in section 1.3 may, in principle, act as effective catalysts, as they exhibit strong chemical incompatibility with the propellant. However, the selection of an appropriate catalyst for rocket engine applications remains a challenging task. In fact, an effective catalyst must also satisfy several stringent requirements. Upon contact with it, hydrogen peroxide should decompose as rapidly as possible, ideally within approximately 100 ms, in order to achieve maximum reaction rates. The substantial heat released during decomposition leads to a rapid increase in the temperature and pressure of the gaseous products, requiring the catalyst to withstand severe thermal shocks without structural degradation. Furthermore, high catalytic activity and stability must be maintained over a wide range of operating conditions, both in the liquid and vapour phases, as well as in the presence of stabilizing agents commonly added to hydrogen peroxide for long-term storage.

One key factor influencing catalyst performance is its **specific surface area**, defined as the area of the material available for interaction with hydrogen peroxide. For being selected, the catalyst must exhibit an optimal balance between surface area and mechanical strength. If this value is too low, decomposition rates drop, resulting in incomplete peroxide decomposition and

reduced exhaust temperatures. On the other hand, if the material has an excessively high surface area, it may suffer structural disintegration during operation, which would lead to undesired pressure drops across the catalyst bed.

Considering common catalytic metals (like nickel, iron, silver and manganese), if only their active phase is used, hydrogen peroxide's decomposition rate would be insufficient for a rocket engine application due to small catalyst surface area. To overcome this limitation, the active phase is applied as a thin layer onto a highly porous **support**. The support structure and shape can vary, but the most common type is pellet-form, consisting of small-sized, porous particles. This type of support present larger specific surface area and can be easily and readily produced in huge quantities from cheap material using a lower-cost technology than other support forms like honeycombs and metallic gauzes. [34]

The most common combination for rocketry applications including hydrogen peroxide is pellets support based on aluminum oxide (γ-Al_2O_3) with manganese or platinum oxide as active phases. Manganese oxides in particular are considered to be very promising for their high activity, especially if coupled with promoters as lanthanum oxides or copper and lead oxides. The catalytic decomposition of hydrogen peroxide in the presence of manganese oxides is a complex process, characterised by a multi-step radical reaction chain, as reported by Jildeh et al. [35]:

$$Mn^{4+} + H_2O_2 \rightarrow H^+ + Mn^{3+} + HO_2^{\bullet} \quad (1)$$

$$HO_2^{\bullet} + H_2O_2 \rightarrow H_2O + O_2 + HO^{\bullet} \quad (2)$$

$$HO^{\bullet} + H_2O_2 \rightarrow H_2O + HO_2^{\bullet} \quad (3)$$

$$HO^{\bullet} + Mn^{3+} \rightarrow Mn^{4+} + OH^- \quad (4)$$

The reaction starts with the adsorption of a hydrogen peroxide molecule on the active phase and the exchange of an electron with manganese oxide. This leads to the formation of a per-hydroxyl radical ($HO_2^{\bullet}$) (Equation 1). The reactivity of the radical product attracts two more peroxide molecules to the reaction (Equation 2 and 3), at the end of which high-temperature steam (water vapour and oxygen) and replenished catalyst are formed (Equation 4). The presence of radical intermediates highlights the importance of catalyst surface properties and active site accessibility, all of which directly influence the overall decomposition rate and thermal efficiency of the catalyst bed.

For the experiment examined in this research thesis, a MnO_2/Al_2O_3 catalyst was selected and synthesized. The substance was produced at the TU Dresden ILR/WIK laboratory by **wet impregnation** method using manganese oxide as active phase and γ-alumina, 1/8" pellets as support. In this choice, particular attention was devoted to the repeatability and scalability of the synthesis procedure, in order to ensure that the resulting catalyst could be realistically reproduced for larger-scale experimental campaigns or future propulsion applications. The carried out process is hereby presented, along with catalyst final results (although for proprietary reasons no quantity measurements of the amount of species is given).

Alumina pellets are firstly ground using a grinder until reaching a desirable size and then separated from smaller debris using a sieve. Final pellets are afterwards polished: they are placed in a beaker with a certain amount of water and stirred with a magnetic stirrer. This step reduces surface asperities and improves pellet uniformity, positively affecting both flow distribution within the catalyst bed and mechanical resistance of the pellets. For obtaining a more homogeneous result, the whole product was placed on a PLA, 3D-printed support which stands 5 mm from the bottom of the beaker, while magnets are rotated underneath, adjusting the

RPM so that all particles are fully agitated. The step is carried out for about 24 hours.

The polished catalyst support is then washed through a sieve to remove the fine alumina particles generated during the polishing process. Then, the support is dried in a convection oven for 24 hours following the temperature gradient shown in figure 2.12. The use of a controlled temperature gradient is particularly relevant for aerospatial catalysts, as it minimizes the risk of thermal shocks and microcrack formation that could later lead to particle fragmentation.

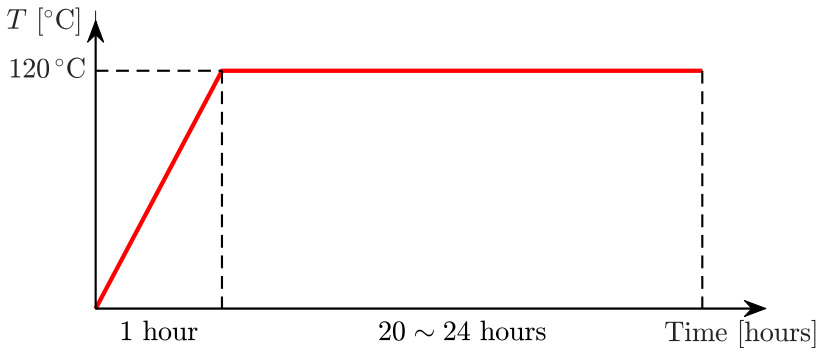

Figure 2.12: Catalyst support drying process

The dried catalyst is afterwards placed in a beaker where the impregnation of the active phase will occur. For this step a solution of sodium permanganate ($NaMnO_4$) is prepared. The solution is slowly poured into the beaker with the help of a glass stirring rod. Due to its high splashing behaviour, the liquid is carefully guided along the glass rod until the support pellets are fully covered. This part clearly represented the most challenging step of the whole process, as manganese oxide has a pronounced tendency to stain surrounding surfaces. For this reason, every laboratory equipment such as beakers and glass rod must be washed several times before reuse. The solution is then stirred with the magnetic stirrer similarly to the previous step for about 24 hours. The opening of the beaker was covered with a sheet of aluminum foil during the process for avoiding permanganate splashes to contaminate the environment, leaving several small holes to allow air to escape.

The air-dried mixture is then filtered using a clean, small sieve, while the rest of the permanganate is removed and discarded (sodium permanganate waste is washed and diluted multiple times before disposal). The impregnated particles are then spread evenly on the sieve and sealed with aluminum foil to prevent the solution flow dripping through the bottom, then placed in a convection oven for the next drying process. The oven is set with a heating ramp of 1 hour to

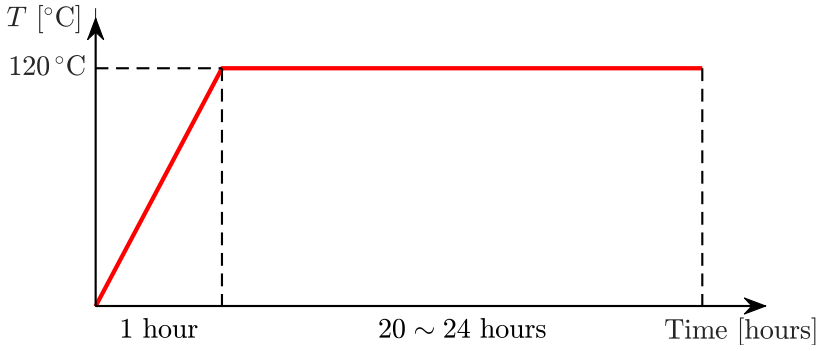

Figure 2.13: Impregnated particles drying process

reach 120°C from room temperature, followed by an holding time of 22 hours, as shown by figure 2.13.

The dried MnO_2/Al_2O_3 catalyst then follows a step of **calcination** in the convection oven. Calcination represents a critical step in the synthesis process, as it promotes the formation of the desired manganese oxide phases and enhances the adhesion of the active layer to the alumina support. For this part, the particles are placed into small ceramic crucibles. The calcination is carried out at a temperature of 500°C, with a heating ramp time of 2 hours and a holding time of 5 hours (see figure 2.14).

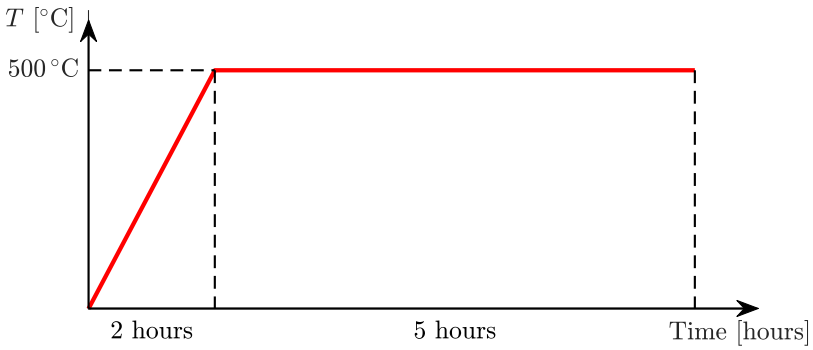

Figure 2.14: Catalyst calcination process

As a final step, the catalyst is washed under running water for about 5-10 minutes. This step ensures the removal of residual sodium species, which could otherwise negatively affect catalyst performance or long-term stability. The catalyst is then dried again in oven for 22 hours at 120°C.

Figure 2.15 shows some pictures during some of the main steps of the synthesis process.

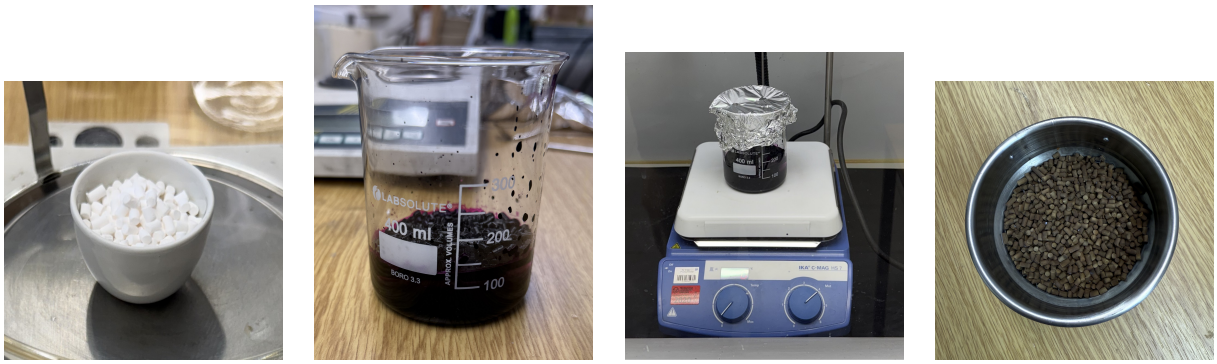

(a) (b) (c) (d)

Figure 2.15: (a) Alumina 1/8" pellets placed in the ceramic crucible while measured; (b) manganese impregnated pellets during air-drying process; (c) manganese impregnated pellets are stirred with the magnetic stirrer covered by aluminum foil; (d) final catalyst results after calcination, final washing and drying.

Following synthesis, catalysts intended for hydrogen peroxide monopropellant applications are typically subjected to a series of performance evaluation tests prior to their integration into propulsion systems. These tests aim to verify the catalytic activity, decomposition efficiency and operational stability of the material under representative conditions. Common evaluation methods include batch or drop tests, in which small amounts of concentrated hydrogen peroxide

are brought into contact with the catalyst surface to qualitatively assess ignition delay and decomposition vigor, as well as flow-through reactor tests that allow for quantitative measurements of temperature rise, pressure drop and decomposition efficiency. In addition, endurance tests are often conducted to evaluate catalyst durability under repeated thermal and chemical loading. Although such characterisation tests were originally planned within the scope of this research, time constraints prevented their execution. Nevertheless, the synthesis procedure was carried out following established methodologies reported in the literature, which have been shown to produce catalytically active and stable materials for hydrogen peroxide decomposition.

Chapter 3

Description of the test setup

The setup designated for testing a new concept of cooling system for a laboratory scale rocket engine is composed of three main parts: the experimental **test bench**, which represents the fluidic and mechanical core of the setup and contains all components necessary for the proper operation of the rocket engine, such as propellant tanks, pipelines, the feed and pressurization system, various valves with different functions, and the engine itself; the **electronics system**, which is responsible for the control of the solenoid valves and the test sequence; the **sensors** and **data acquisition system**, which are fundamental in an experimental campaign for acquiring the necessary results.

The realization of the setup took several months of work and involved the selection and

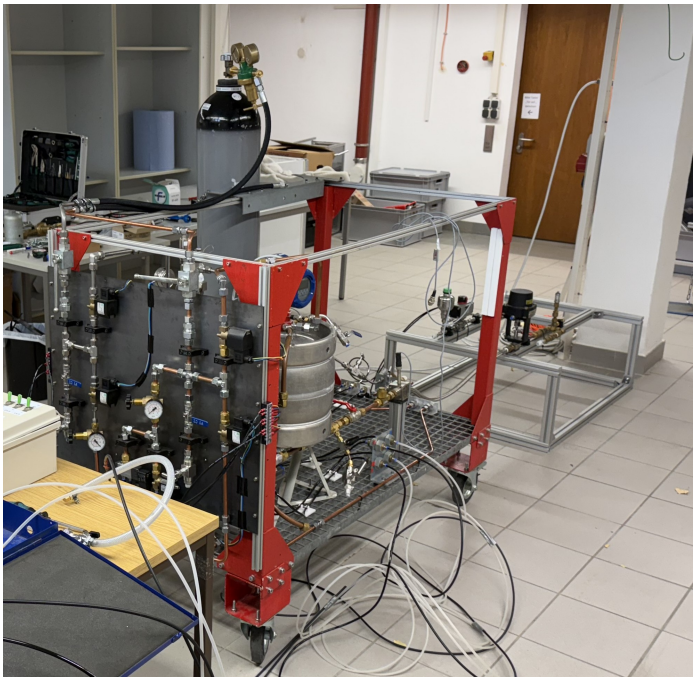

Figure 3.1: Experimental test bench prepared for the pressurization test set up in the wind tunnel laboratory. On the left there is the metallic trolley with the storage and feeding section, while on the right there is the engine support section (although in this case engine was not mounted on the bench). For the pressurization test, only one nitrogen vessel was employed due to temporary pressurized gas low availability.

integration of numerous fluidic components, including valves, manifolds, tubing, fittings and flexible connections, as well as their mechanical support and routing. Particular attention was devoted to the assembly of hydraulic and pneumatic lines, requiring the use of specific tools, careful handling procedures and precise installation techniques in order to minimize leakage risks.

Equally challenging was the preparation of the electronics and sensors compartments, including their connections with the solenoid valves and the rest of the system. This phase required a detailed understanding of the communication protocols adopted by these devices and their necessary control logic.

In the following sections, the complete test setup will be described, by giving a detailed presentation of the test bench and an explanation of all its different branches and their associated function. Subsequently, the working principle of the various component types implemented in the test bench are discussed. This presentation also includes the control logic adopted for operating the solenoid valves, which are responsible for the most important functions within the system. Then, a description of the sensors used for the test campaign will be given, together with the Data Acquisition System and the dedicated software tool for data post-processing. Finally, as a practical example of the overall setup operation, the execution of a pressurization test is described.

3.1 Experimental test bench

This section is dedicated to the presentation of the experimental test bench specifically developed for the present campaign, with the aim of describing in detail its functionality and highlighting the main challenges encountered during its realization. The system was designed and assembled at the TU Dresden ILR/WIK Wind Tunnel Laboratory over a period of approximately five months.

The development of the test bench required a combination of theoretical design and practical implementation, addressing both functional and safety-related requirements. In particular, the setup was conceived as a fully integrated system, comprising all the hydraulic and pneumatic lines necessary for the nominal operation of the experiment, as well as auxiliary circuits and emergency features implemented to address safety concerns, such as venting, purging and isolation capabilities. These elements were incorporated from the early stages of the design process in order to comply with laboratory safety standards and to ensure safe operation throughout all phases of the experimental campaign.

The design of the test bench was primarily driven by the need to integrate all system elements within a relatively limited available space, while simultaneously ensuring a clear and orderly routing of lines and cables and ease of operation. In this sense, particular attention was devoted to the arrangement of control interfaces, such as valves, in order to guarantee their accessibility at all times during both normal operation and, most importantly, emergency conditions. Additionally, an effort was made to preserve a consistent level of symmetry between the two propellant sides. This approach resulted in two largely independent and almost identical subsystems, which proved beneficial for system comprehension and familiarization, operational clarity and reduction of handling errors during test procedures.

From a structural and layout perspective, the test bench consists of two separated parts, the **storage and supply section** and the **engine section**. This configuration was chosen mainly due to safety reasons, so that the engine, namely the most critical and risk-generating element of the

system, is separated from the rest and can be also isolated in hazardous cases, while the remaining, more complex and expensive part is safe. A more detailed explanation of the intended test site organization and benches disposition will be given later in this section. Focusing on the first part, its configuration was built on a compact mobile trolley with approximate dimensions of 1.5 m × 1.0 m, allowing the entire setup to be easily moved and transported to the test site when required. The supporting structure consists of a metallic frame resembling an open cage, featuring a lower grated platform and vertical steel beams at the corners. This configuration provided both high mechanical stability and sufficient flexibility for all components placement.

In order to provide a clear overview of the test bench layout and the interaction between the different subsystems, the complete setup is introduced through the P&ID diagram shown in figure 3.1. This type of diagram is the best way for summarizing fluids flow paths and line connections, symbolically representing each component and element of a complex architecture. The entire system is pressurized using high-pressure gaseous nitrogen, which is contained into two **vessels** (1), one for each propellant line. Nitrogen was preferred to other inert gases like helium and argon because it is far cheaper, denser (hence less quantity is required for the experiment) and equally stable when coupled with hydrogen peroxide and ethanol. Due to their size and weigth, the pressurized vessels could not be mounted directly on the test bench trolley and were therefore secured in place to the side of it with two dedicated chains. During setup operations, the trolley is first positioned at the test site, after which the vessels are carefully moved separately and placed alongside the bench by rolling them on their lower perimeter.

Both vessels are equipped with multiple safety measures: first of all, the main release of pressurized gas is controlled by a main shut-off valve placed on the top of each vessel; then, a pressure regulator is installed (2) to adjust and maintain the desired nitrogen pressure at a constant level. Additionally, the regulator has also an incorporated safety needle valve to allow gradual opening of the line. This arrangement creates a sequential safety configuration, in which the system transitions from a fully sealed state to a controlled pressurization through successive and independent actuation steps: nitrogen is first released by opening the main shut-off valve, then the desired outlet pressure is set through the regulator and finally the needle valve is gradually opened to allow pressurization of the downstream subsystem.

From each vessel, a separated pneumatic line departs to pressurize a complete subsystem. All lines (both hydraulic and pneumatic) are manufactured from materials selected according to their compatibility with the respective propellant. Fuel lines are made of bronze, chosen for its low cost and high formability, which facilitates bending and routing within the limited available space. However, this material is unsuitable for the oxidizer line because of incompatibility reasons and it was rather employed stainless steel, although much more expensive and harder to bend.

A ball valve (HP_Gas_BV (6), Eth_Gas_BV (6)) is implemented on each pressurization line to allow manual isolation of the nitrogen vessels when required. Downstream of these valves, two filters (4) are also installed to prevent any type of debris or particulate contamination from potentially obstructing the system. The pressurization line feeding each propellant tank can be interrupted by a remotely controlled solenoid valve (HP_Tank_SV (5), Eth_Tank_SV (5)), enabling rapid isolation during operation or emergency conditions. In addition, a check valve (10, 12) is installed to prevent any gas from flowing backwards to the vessels. This component plays a fundamental role in protecting the upstream branch, which is not designed to withstand sudden pressure surges and emergency backflow conditions. Both lines also include a dedicated vent branch, which allows residual pressurized gas trapped in the system to be safely discharged

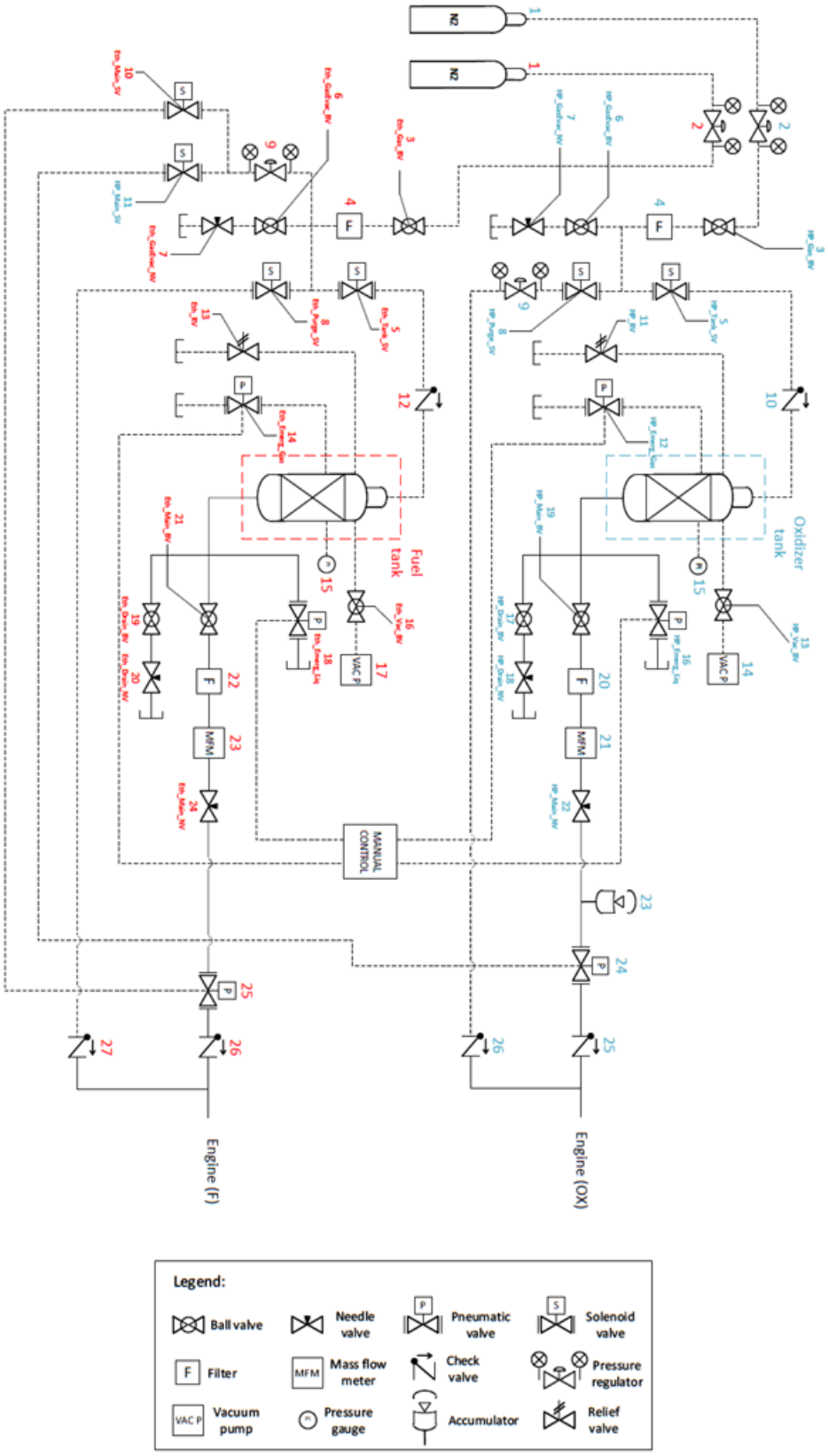

Figure 3.2: Test bench storage and supply section P&ID

once the experiment is concluded and both ball and solenoid valves are closed. Venting is performed through a combination of a ball valve (HP_GasEvac_BV (6), Eth_GasEvac_BV (6)) and a needle valve (HP_GasEvac_NV (7), Eth_GasEvac_NV (7)), enabling a slow and controlled depressurization while minimizing the risk of dangerous vibrations for more delicate components.

The pressurization lines then deliver high-pressure gaseous nitrogen to the **propellant tanks** from the top. Both propellant tanks have a nominal volume of 12 liters and consist of austenitic stainless steel cylindrical pressure vessels. The tanks are rigidly soldered to dedicated tubular support structures, providing enhanced mechanical stability and ensuring a fixed and robust positioning on the test bench trolley. The propellants, hence, flow from the bottom of the tanks towards the final part of the system and the engine. The main propellant lines consist of rigid tube sections connected with hydraulic manifolds and fittings, specifically adopted for avoiding liquid leakages. The propellant supply to the engine is directly controlled by the actuation of a set of pneumatic valves (24, 25), placed at the end of each line. As discussed in following sections, pneumatic valves can change position when a sufficiently-high pressure gas is provided. In this case, pressurized nitrogen is supplied to the valves from a dedicated branch of the fuel pressurization line, by opening two solenoid valves (HP_Main_SV (11), Eth_Main_SV (10)). The reason why both pneumatic valves are powered with pressurized gas coming from the fuel line is that, due to the much lower required fuel mass flow rate, less pressurized gas is required as well. Moreover, the fuel does not flow through the catalyst bed, therefore is subjected to a smaller pressure loss.

Along the main feeding lines, additional valves (HP_Main_BV (19), HP_Main_NV (22), Eth_Main_BV (21), Eth_Main_NV (24)) are also installed in order to hypothetically interrupt the propellant passage at necessity, as well as filters for preventing pipeline obstructions and two Coriolis-type mass flow meters for monitoring propellants mass flow rates.

The tanks are refilled by recreating internal vacuum conditions with a vacuum pump, which is connected at the top of the tank, after opening valves HP_Vac_BV (14) and Eth_Vac_BV (16). The negative pressure generated by the vacuum pump allows the propellants to be drawn into the tanks from below, after opening two drain valves (HP_Drain_BV (17), HP_Drain_NV (18), Eth_Drain_BV (19), Eth_Drain_NV (20)). Moreover, each tank is equipped with multiple safety features to employ in emergency cases of power outages. Since under normal operating conditions propellant flow is controlled exclusively through the actuation of electrically driven solenoid valves, in the event of a loss of electrical power these valves may no longer be actuated. In such case, dedicated emergency venting and draining lines are implemented for each tank, allowing both residual pressurized gas and liquid propellant to be safely evacuated by manually opening four pneumatic emergency valves (HP_Emerg_Gas (12), HP_Emerg_Liq (16), Eth_Emerg_Gas (14), Eth_Emerg_Liq (18)). These valves are actuated via a manual control interface, connected with a continuous supply of pressurized air.

An additional layer of safety is provided by a pressure relief valve installed on each tank (HP_RV (11), Eth_RV (13)), which ensures that the internal tank pressure remains below a maximum threshold of 100 bar. This passive safety device operates independently of the control system and prevents structural overload in case of over-pressurization. Furthermore, tank pressure can be continuously monitored during all phases of the experiment with a dedicated pressure gauge (15). Although the best way for keeping tracks of tank pressure is the use of calibrated pressure transducers, this element allows real-time verification of the tank pressure state, proving helpful especially during pressurization and post-test depressurization procedures.

A further safety measure implemented on the propellant feed line is represented by an accumulator, a device which acts as damping volumes during rapid valve closure. During shutdown of the experiment, when the propellant feed is interrupted by closing the main solenoid valves, a rapid pressure decay occurs inside the engine. At the same time, pressure rises upstream of the pneumatic valves due to the sudden flow arrest. This transient phenomenon may lead to pressure oscillations and "water-hammer" effects, potentially propagating upstream along the feeding lines and inducing mechanical stress on sensitive components. In this sense, accumulators can absorb pressure peaks, thereby protecting the upstream system from potentially damaging pressure transients.

One last section of the system are the two propellant **purge lines**, consisting in two pneumatic lines which depart from the pressurization circuit, upstream to the propellant tanks. Their goal is to directly provide pressurized nitrogen to the engine at the end of each fire sequence in order to eliminate any propellant residual and prevent any further combustion. Purging procedure can be manually controlled by operating a solenoid valve (HP_Purge_SV (8), Eth_Purge_SV (8)). As can be seen by the P&ID scheme, two check valves are also implemented at the end of the lines: this way, during nominal operation of the propulsive system, the propellant is supplied to the engine and can not flow back through the purge line; on the other hand, during purging procedures, neither the gas can reach the tank through hydraulic lines. Furthermore, since the oxidizer is injected upstream to the catalyst bed, on its purge line a pressure regulator is also installed for lowering the gas pressure to a value (10-15 bar) that would not cause any catalyst damage.

As mentioned before, the test bench was designed as a two-sections architecture, consisting of one main setup built on a metallic trolley and a separate engine support section realized with a tubular metallic structure. This configuration was primarily chosen due to the intended test site environment. The main hot-fire test is planned to be conducted at a dedicated experimental facility specifically designed for rocket engines testing. The experiment would be performed under open-air conditions, with the propulsive system surrounded on three sides by reinforced concrete bricks walls. The engine exhaust plume faces a series of retaining walls, arranged in arc-shape configuration.

For safety reasons, the engine represents the most critical and hazardous element of the entire setup and therefore requires a higher level of protective measures. On the other hand,

(a) (b)

Figure 3.3: (a) Schematic representation of the test bench layout within the test site; (b) dedicated experimental facilities for rocket engine testing.

the remaining and more complex part of the test bench can be secured behind the protective walls. Hence, this layout with separated sections allows the main bench structure to be preserved in the event of engine malfunctions or detonations, which always represent a significant risk when testing new rocket engine configurations. The two separated sections are then connected by 4 distinct lines: two hydraulic flexible, stainless stell lines for the propellants supply and two pneumatic lines for engine purging. A visual representation of the intended test setup arrangement is provided in figure 3.3.

3.2 Detailed description of each component

The test bench features a wide variety of valves distributed throughout the hydraulic and pneumatic lines. Each valve is characterised by a specific actuation method, contributing to an intentional level of safety redundancy within the system. As a result, any branch of the setup can be isolated at all times and fluid flow can be promptly interrupted when required. This approach ensures safer and more controlled operation during all phases of the experimental campaign and proved particularly beneficial during initial system familiarization.

Moreover, the presence of different valve types allows to effectively manage the system functionality under all operating conditions, including off-nominal and emergency situations such as power outages or potential component failures. Each valve and auxiliary component follows a specific operating principle and fulfills a well-defined role within the test bench architecture. The purpose of this section is to describe each element type and illustrate their functioning within the overall system.

3.2.1 Ball and needle valves

The easiest way of controlling a fluid passage along a line is by using manual-actuating valves, such as **ball** and **needle valves**. These two types of components, although very simple, represent two essential elements in both hydraulic and pneumatic systems and are characterised by a relatively straightforward functionality. The following figure shows the schematics of the two component types, highlighting their working principle.

In general, a valve interrupts a flow passage by physically obstructing the line. What differentiates between various valve types is primarily the actuation method. Manual actuation represents the easiest and most robust possible way, because it does not rely neither on eletrical nor other forms of connections, therefore can be utilized at all times, including during power outages. However, this excludes the possibility of a remote actuation, which can be helpful or even necessary in emercency conditions. Moreover, these types of valves are relatively slow in changing position, hence are not suitable to be utilized as primary shut-off device for propellant supply.

A **ball valve** has a highly compact architecture and, as suggested by its name, consists of a perforated sphere, welded to a metallic stem and an external lever. Then, at both sides, G-threaded manifolds allow sealed connections of the valve with the rest of the lines. The flow passage is permitted when the hole in the ball is parallel to the inlet and outlet ports. The valve changes position as the lever is rotated, which causes the ball to rotate accordingly, permitting a gradually actuation from a fully closed position to a fully open one. This method has the benefit of a fairly fast actuation, although it does not permit a precise positioning.

A pratical way of identifying a ball valve position is by looking at its lever orientation: normally, levers are mounted parallel to the sphere's hole; hence, valve is open if the lever is alligned to the pipeline, closed if it is placed perpendicularly. More advanced ball valve designs

also include safety locks for securely maintaining positions. [4]

Ball valves are often coupled with **needle valves** in hydraulic pipelines. A needle valve has a different working principle, while maintaing a fairly simple design. The main element is a metallic, threaded plunger, featuring a tapered point end and a cylindrical, upper handle. On the lower part, flow goes through a small orifice with a long, tapered seat, which perfectly fits the plunger end's needle-shape. As the handle is rotated, the plunger vertical position can be adjusted thanks to its thread, therefore determing the orifice occlusion by the point end and, consequently, the flow passage. Valve's position can be changed gradually by rotating the handle as a screw: a clockwise rotation screws the plunger into the thread, closing the valve, while a counter clockwise rotation retracts the plunger and opens the valve.

Since it takes many turns of the fine-threaded screw to retract the plunger, needle valves are not used for simple shut-off applications where a more fast actuation method is required. Nevertheless, they allow a very precise regulation of the flow rate. Moreover, it is not possible to recognize its position solely by looking at the handle, hence necessing a small rotation attempt. [5]

To sum up, ball and needle valves present complementary advantages and drawbacks. For this reason, they are frequently employed together in fluid systems, to achieve a more practical and flexible configuration.

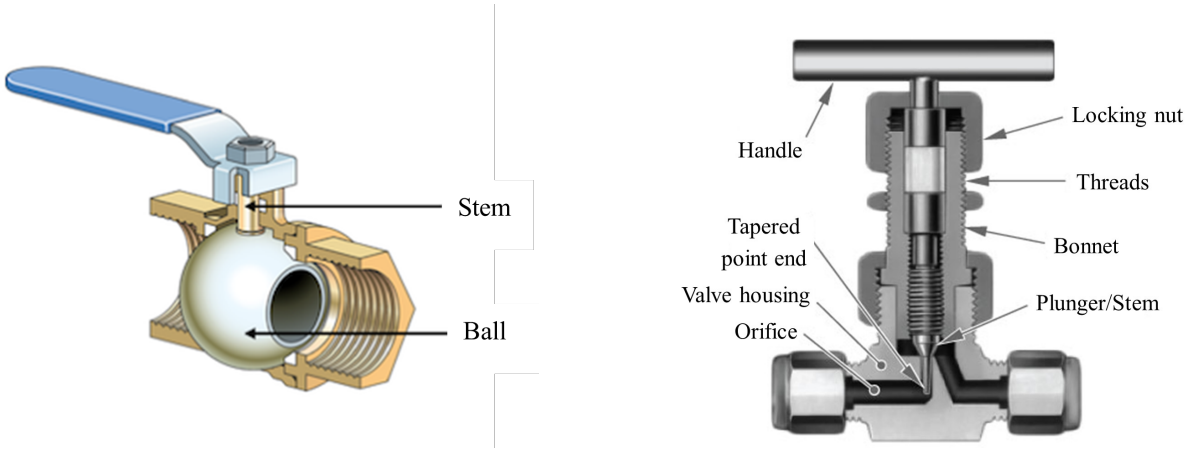

Figure 3.4: Schematic representation of a ball valve (a) and a needle valve (b) [4, 5]

3.2.2 Pneumatic valves

Pneumatic valves are highly reliable components, whose actuation requires the presence of a gas at a sufficiently high pressure level. Although there are several types of valves with different architectures, this section focuses exclusively on two-way valves, which are characterised by two ports only, an inlet and an outlet. The main element of the valve is represented either by a flexible diaphragm and a plate enclosed in a pressure-tight housing, or by a piston contained in a cylinder. In both cases, this element is rigidly connected to an actuator stem and presents a spring. The extremity of the actuator stem, hence, can obstruct the flow passage by perfectly fitting in a tapered orifice, similarly to a needle valve concept.

Depending on the relative arrangement of the spring and the piston in the upper case, a pneumatic valve can be **normally-closed** (as the one represented in figure 3.5) or **normally-open**. In both cases, pneumatic pressure enters the housing and applies pressure to the main moving element (piston or diaphragm). As the air pressure increases, the force exerted against the spring rises accordingly, causing the actuator stem to move and change the valve position. Intuitively, valve can maintain its position only if the incoming gas keeps the required pressure level.

As the piston moves and compresses the spring, air pressure in the opposite side of the housing would rise as well, therefore impeding the actuator movement. For this reason, cylinder's side featuring the spring has always a venting hole, ensuring that the internal pressure remains at atmospheric level and does not interfere with valve operation.

Pneumatic valves can be further classified either as single-acting or double-acting, depending on the number of gas supply lines which are connected to the cylinder. A single-acting valve receives pressurized air only from a single supply line. When sufficient positive pressure is applied, valve changes position; to return to the initial state, the pressurized side of the cylinder has to release air, usually from an implemented auxiliary valve or release port, allowing the spring to restore its original configuration. Conversely, in a double-acting valve a distinct gas supply line is connected to each side of the cylinder. In this case, valve actuation and repositioning are achieved by alternately pressurizing the two sides. [6, 36]

In the test bench developed for this experimental campaign were installed five pneumatic, single-acting valves (25, HP_Emerg_Gas (12), HP_Emerg_Liq (16), Eth_Emerg_Gas (14), Eth_Emerg_Liq (18)) and one double-acting valve (24), due to temporary equipment availability.

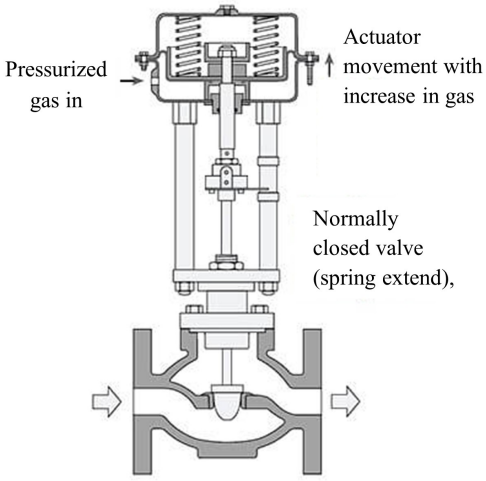

Figure 3.5: Schematic representation of a normally-closed, two-way pneumatic valve [6]

3.2.3 Solenoid valves and Portable Logic Controller (PLC)

The last type of valve employed in the experimental test bench is the **solenoid valve**, which consists of an electro-mechanically operated valve. Its functionality resembles pneumatic's one, since they feature a plunger with a spring, which axially moves when the valve is powered and fits in a tapered seat, obstructing the flow passage. What differs is the valve's actuation method: solenoid valves are powered by electrical current (alternate or direct) rather than pressurized gas.

In this case, the main element of the valve is a magnetic coil, positioned on top of the two manifolds. The coil has the property of generating a sufficiently powerful magnetic field when current runs through it. The metallic plunger is installed at the centre of the coil, where magnetic field lines are the most compact and the field has its maximum intensity.

When current passes through the coil, the resulting magnetic force causes the plunger to axially move, overcoming the opposing spring force and changing the valve position. As for pneumatic valves, solenoid valves can be normally-closed or normally-open. In a normally-closed configuration, the valve obstructs the flow passage when de-energized. Hence, when power is supplied, the plunger is retracted by the coil's magnetic field, opening the connection between the inlet and outlet ports. Conversely, in a normally-open valve, the plunger is already retracted and due to the magnetic forces it moves downwards into the tapered seat, interrupting the flow. Between the two configurations, the plunger motion differs due to the mechanical arrangement of the spring and valve seat, while the spring defines the default valve position in the de-energized state. Nonetheless, in both cases energizing the coil generates an attractive magnetic force that pulls the plunger toward the region of maximum magnetic field, regardless of the direction of the flowing current. [37]

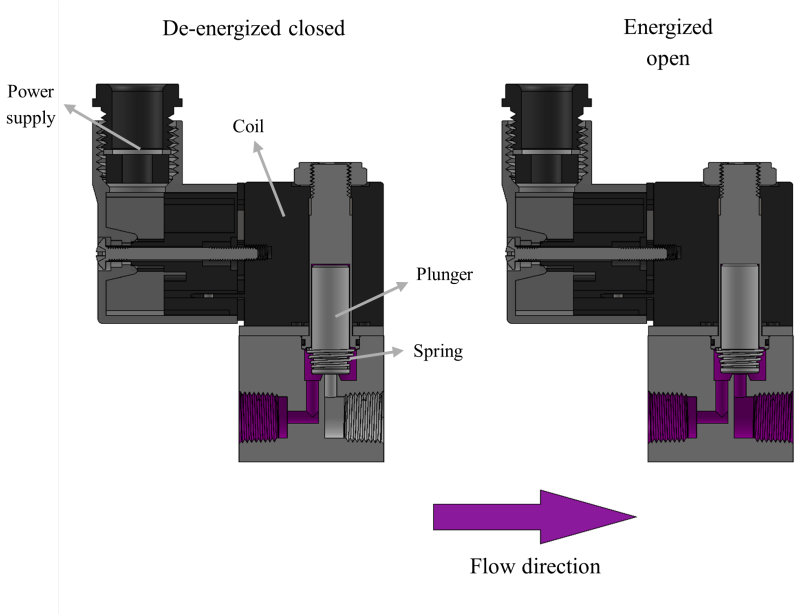

Figure 3.6: Schematic representation of a normally-closed, two-way solenoid valve [7]

Due to their working principle, solenoid valves typically operate with a delay of 5 to 10 milliseconds after electric power supply. Moreover, as pneumatic valves, they do not need manual actuation and can be remotely controlled. Their high reliability, precision and adaptability make them a necessary component in numerous types of industrial and everyday automation systems.

For all these reasons, in the developed test bench solenoid valves were implemented to serve for the primary functions of the system, which are tank pressurization, propellant supply and purging execution. In particular, were implemented five two-way, normally-closed, single-acting solenoid valves (HP_Main_SV (11), Eth_Tank_SV (5), HP_Tank_SV (5), Eth_Purge_SV (8), HP_Purge_SV (8)) and one three-two way solenoid valve (Eth_Main_SV (10)). The latter's name means that the valve features three total ports, one inlet port and two outlet ports, and two possible positions. Consequently, flow passage is always permitted to at least one of the outlet ports, while valve's actuation changes the position of the stem body and therefore the

connected manifold. This configuration was necessarily implemented for valve Eth_Main_SV, which provides pressurized gas to the main oxidizer pneumatic valve (24). As it was explained in section 3.2.3, valve 24 has a double-acting actuation method, hence requires gas supply for both opening and closing movements.

As it was mentioned above, solenoid valves can be remotely controlled by sending precise electrical inputs generated in several various ways. A typical way of managing input and output signals is by using a **Portable Logic Controller** or **PLC**, a programmable control unit which is capable of carrying out pre-programmed outputs based on received inputs and following a set of uploaded logic rules. Depending on the program installed on the controller, outputs can be triggered manually, for example by turning a switch on, or automatically by following a precise sequence of commands, logic operations and timers. For these reasons, PLCs are vastly employed in different types of industrial and commercial applications to control systems with minimal manual intervention.

Initially, PLCs replaced panels of relays, which were electrically operated switches that controlled running machines and devices. Relays had a very simple working principle, although they were relatively slow and rather cumbersome, moreover they were not very reliable and need physical changes in the wiring in order to operate a different logic. The advent of solid state electronics and microchips allowed bulky relays banks to be replaced with much more compact controllers, which operate on software logics.

Although there are many variations of PLC, its basic architecture remains basically the same, containing an input module, a Central Processing Unit (CPU), an output module and a power module. The input module contains a terminal block through which the PLC can acquire input signals from the outside world. This inputs can be digital signals, such as the one provided by an on/off switch, or more complex analogue inputs, like a sensor measurement. In both cases, this signal is properly converted into a digital format for the PLC's CPU, for example by filtering noise or eliminating oscillations.

The CPU is a small computer capable of running a set of rules or a program, based on the inputs signals provided by the first module. It typically consists of a microprocessor, which is the actual component that operates the program based on the input values; a memory chip in which the program and its whole history (inputs and outputs, flags and faults etc.) are stored; integrated circuits such as modbus and LAN connections, thanks to which it is possible to remotely communicate with the PLC, reprogram and monitor it. Moreover, the CPU module may also contain a little battery for keeping the PLC alive for a limited time in case of a power failure.

The output module is much similar to the input one and features a dedicated terminal block where all necessary devices can be connected. The number of terminals in both modules changes depending on the PLC model. Finally, the power module contains a power supply which provides current for the correct fucntionality of the controller and all its parts.

The chosen PLC is a LS Electric MASTER-K120S, powered by an external 24 V DC power supply. The controller is equipped with 36 digital input pins and 24 relay-type output pins and does not feature any analogue input terminals (although several additional module can be implemented for analogue devices). The controller case is placed in a compartment along with everything else necessary to its functionality, while input switches and output connections are accessible from the cover of the box. Figure 3.7 shows the PLC model employed in this test campaign placed in its dedicated compartment.

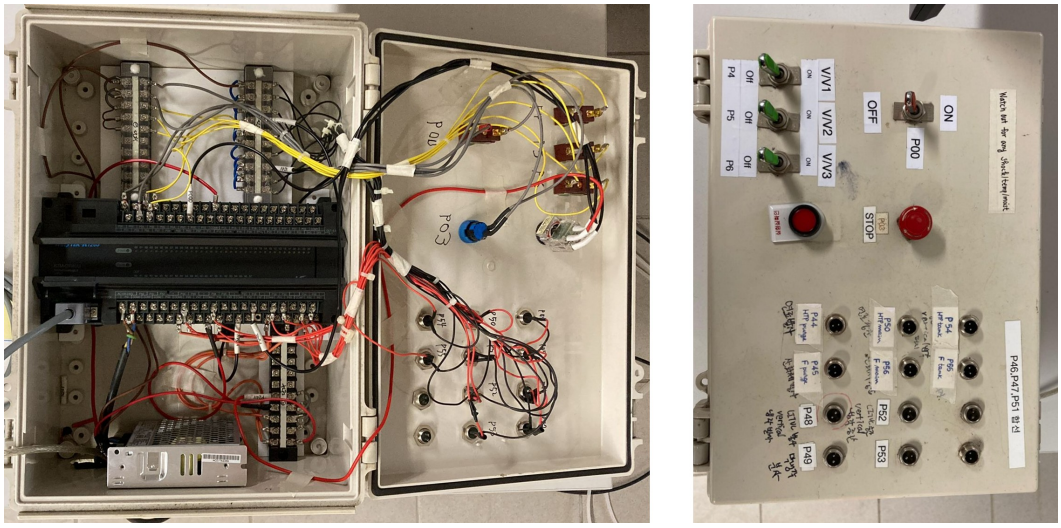

Figure 3.7: Inner and outer view of the PLC compartment

Referring to the image, the input module and its terminal block are located on the upper side of the PLC, to which are connected five input switches: one main switch for the execution and termination of the entire system (P00), three switches for occasionally controlling outputs independently of the programmed task sequence (P04, P05 and P06) and one final push button for the emergency shut-off of the PLC (P03). Meanwhile, the output terminal block is placed on the lower part of the case and here are attached the six solenoid valves (orderly, P54 - HP_Tank_SV, P55 - Eth_Tank_SV, P50 - HP_Main_SV, P56 - Eth_Main_SV, P44 - HP_Purge_SV, P45 - Eth_Purge_SV). At the centre, two lines of LEDs show in real time how the controller is working and which contact is powered. On the top-left corner, a manual switch permits to control the PLC working mode between three choices: when in RUN mode, the PLC can run programs and tasks, other than receive manual inputs; PAUSE mode allows to temporary interrupt the program execution for reprogramming the controller or make adjustments to the code; STOP mode turns the PLC off. Finally, through a RS-232C/RS-485 communication port, the PLC can be connected to a PC or a HMI for monitoring and reprogramming the system, using dedicated softwares.

Due to the numerous connected devices (both input and output ones) and consequent wires, additional terminal blocks were added to the architecture. A terminal block is a hardware component that allows the distribution of current to multiple devices. In the presented arrangement were used three terminal blocks, two of them for distributing 0 V (upper side) from the power supply and one of them for distributing +24 V DC (lower side). For a more precise and neat layout, terminal blocks are mounted on 3D-printed PLA support plates, placed around the PLC case.

Depending on how the input module of the PLC is connected to the input device, PLCs can operate in either current **sourcing** (or **PNP**) and current **sinking** (or **NPN**) mode. These two terms describe the direction of current flow between the PLC and the connected devices. In a sinking configuration, the PLC input module provides a connection to 0 V, while the external device provides +24 V DC. In this case, it is said that ”the external device is sourcing the current and the PLC is sinking the current”. Conversely, in a sourcing configuration, the PLC provides the positive voltage while the external device connects the 0 V, therefore currents flows from the PLC to the device.

LS MASTER-K series models are characterised by a great flexibility and their input terminals

support both sink and source configurations, making the choice between the two arrangement arbitrary. For this project an input sinking-type (NPN) setup was selected. In fact, from the power supply, positive voltage is provided to the COM (Common) port of the PLC input module. The COM port is a common terminal which provides a certain current to all input pins of the PLC. Then, voltage is brought from the PLC terminal to the switches, which are thus connected to power supply 0 V. Hence, PLC sources current to the sinking input switches.

Regarding the output module, since the output are of relay-type with mechanical contacts, sourcing and sinking description does not apply. Here, PLC simply sends a signal to the output module to close the circuit and power the connected device.

For monitoring, modifying and debugging the program, LS MASTER-K PLC series rely on the KGLWIN software, a Windows-based tool developed by LS Electric which uses a visual programming language called **ladder logic**. This language mimics traditional electric relay circuits, whose shape superficially resembles a ladder. In a conventional relay circuit, connections are represented with horizontal lines called **rungs** and vertical rails: at the top of the ladder it is a placed a power supply, with the power rail going to the left side of the ladder and the neutral rail going to the right. Then, each horizontal rung represents a logical connection between inputs, positioned on the left, and coils or outputs, on the right. According to this representation, power is therefore flowing from left to right. All elements of the circuit are also represented with intuitive symbols.

Different outputs are placed on distinct horizontal rungs and, by convention, the program is read by descending the ladder, working from top to bottom.

Figure 3.8 shows an example of ladder logic program in the KGLWIN environment. The software interface has a top toolbar for the access to the primary functions, for example for creating a new program or opening an existing one, for modifying the window appearance, for

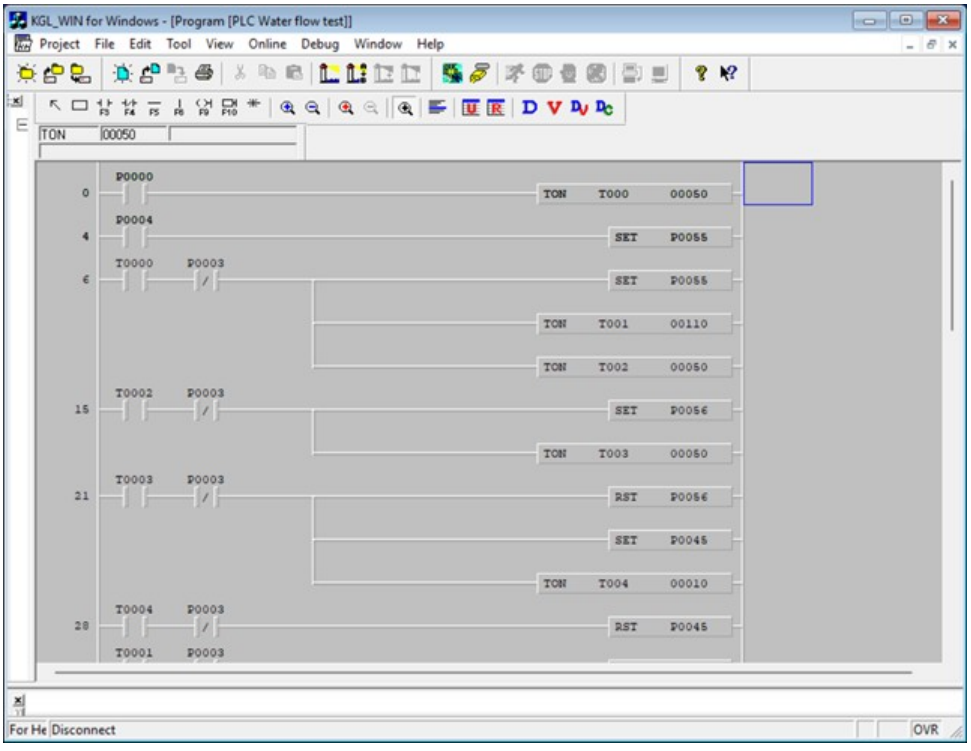

Figure 3.8: Example of a ladder logic program on KGLWIN

debugging the program and more. Of particular importance is the ”Online” functions section, through which it is possible to connect and disconnect the PLC from the computer, upload a program on it and remotely changing its mode.

The whole project is developed within the central programming box. The power supply at the top of the diagram is not physically shown, however from the top of the window the two main vertical rails depart, the left power one and the right neutral one. To create a command, a connection from the left rail to the right one must be established, by placing an input component, such as normally-open or normally-closed contacts, and an output or a load. A single rung can also include multiple loads connected in parallel.

As rungs are created, numerical labels on the left side of the diagram explain what the tasks order would be, running from the top of the program to the bottom. The program termination is finally represented by an empty rung containing an END button.

Each element of the program, once defined, it refers to a specific contact on the PLC, assigned by its name. This implies that, when creating a program, physical hardware connections between the PLC, switches and loads must be known in advance.

The ladder logic allows to power a load not only based on a direct physical input, but also as a function of previously defined output values or states. For example, in rung 0 of the presented program, as the P00 contact is closed (by pressing a button or turning a switch on), function TON (Timer ON) is activated. This creates and starts an on-delay timer of 5 seconds named T000. This command is useful for delaying actions, since it starts a countdown when its input becomes true (ON) and activates its output only after the preset time has elapsed. Hence, in rung 6, the timer closes the corresponding contact and permits to power the requested loads. A normally-closed contact is also included in the same rung as a safety measure: in case of failure, the emergency push button connected to P03 can be pressed and interrupts all connections with outputs.

Finally, for activating a solenoid valve, SET and RST functions are employed. These commands are typically used as latching instructions in ladder logic to turn outputs on (SET) and off (RST), acting like physical switches. For example, in rung 4, by turning switch P04 on, valve connected to P55 is opened. A similar line using RST function instead resets the output value to 0, closing the valve.

In the programs developed for this thesis, only a few, basic functions were implemented, although the KGLWIN software is equipped with dozens of very specific others and presents a lot of different features. The description hereby presented is therefore not intended as a complete overview of the software. For a complete and detailed documentation, reference is made to the KGLWIN user manual reported in the bibliography. [38]

3.2.4 Relief valves

A relief valve is a safety measure used to control the pressure level of a tank or system, by opening at a predetermined set pressure. This device allows to protect pressure vessels and other components from being subjected to pressures that exceed their design limits. In the developed test bench two pressure relief valves are implemented, one for each propellant tank, for limiting the pressure inside the tank underneath a certain fixed level (100 bar).

Typically, a relief valve is installed on a hydraulic or pneumatic line, to which it is connected thanks to a threaded manifold. The main element, as for pneumatic valves, is a spring, whose rigidity can be adjusted in some valve models with a screw, hence modifying the set pressure.

The spring is rigidly connected to the valve body. As long as the force applied to the valve body by the pressure of the fluid inside the system is less than the spring force, the valve remains closed. However, if the pressure level rises, its force overcomes the spring one, moving the valve body from its seat, and opening the auxiliary circuit. Pressure is therefore relieved, depressurizing the system. The valve stays opened until the system's pressure level is not reset again below the spring force value.

For high-pressure systems involing non-hazardous fluids, like in this experimental campaign, the outlet of relief valves would be the atmosphere. By contrast, if the system contains harmful fluids, the diverted fluid should be recaptured by a vapour recovery system and afterward either burned or appropriately discharged.

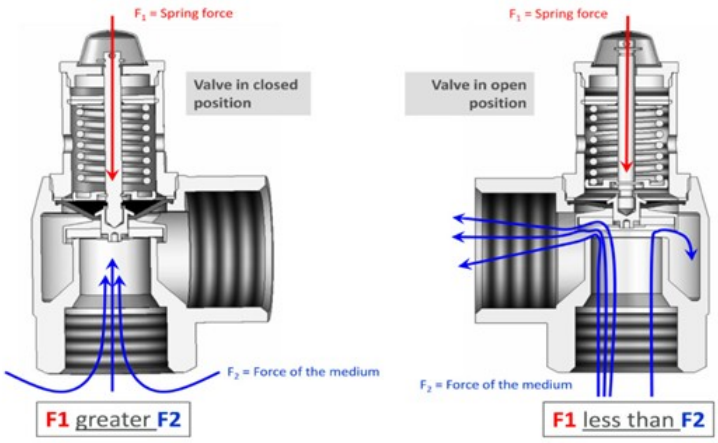

Figure 3.9: Schematic representation of the functionality of a relief valve [8]

3.2.5 Check valves

A check valve is a two-port valve that allows a fluid to flow through it in only one direction, by blocking its passage with a movable internal object. Its operation is entirely passive and relies exclusively on the pressure difference across the valve, without requiring any actuation or control signal.

Although several different types exist (such as ball, diaphragm, lift and butterfly check valves), a swing check valve (like the ones implemented in the test bench) contains a disc as the obstructing part, which is hinged to the valve's body. When fluid flows in the right direction, it can easily pass through the valve by shifting the disc from its place and making it rotating around the hinge. Conversely, if pressure is applied from the opposite direction, the disk is pushed back into its seat and the valve is closed, not allowing the fluid to pass through. Hence, their correct installation is essential for proper operation.

Normally, check valves are employed as safety measures in hydraulic and pneumatic systems for preventing undesired backflow conditions, which could lead to over-pressurization, contamination of upstream branches or damage to delicate components such as tanks and measurement devices. Their simple construction and high-reliability make them particularly suitable for high-pressure hydraulic and pneumatic systems, however in cases with high flow rates non-negligible pressure drops due to the disc-hinge mechanism should be taken into account.

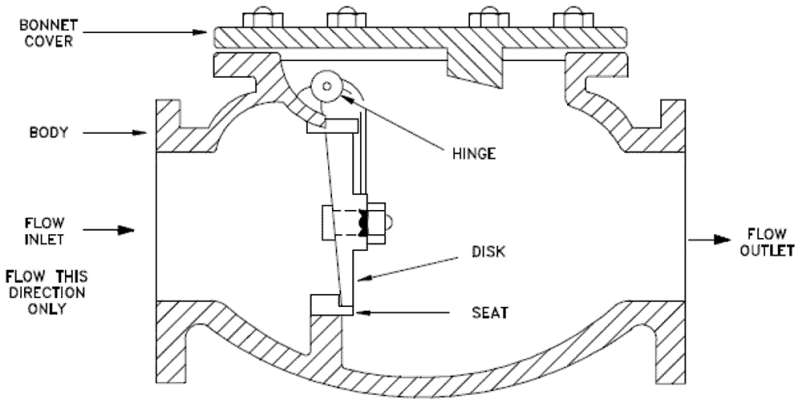

Figure 3.10: Schematic representation of a swing check valve [9]

3.2.6 Filters

The function of a hydraulic filter is to prevent any foreign and undesired substances from entering the hydraulic system, since the presence of small debris and particles can cause irreversible damage to the components if unchecked. Filters therefore catch contaminants by forcing the fluid through a very fine porous element. The pore size is on a scale of micrometers, meaning that hydraulic filters must be properly sized to filter out even the smallest of particles.

By analysing the internal architecture of a conventional micro-hydraulic inline filter, it is possible to identify two main elements, both mounted together between the gasket and the component body. The first one is the filter element, a porous structure usually having a cylindrical metallic shape. Following the fluid path, the flow passes from the outside of the cylinder through the porous medium and then proceeds downstream. The second element is not always present and it is represented by a spring, which serves as a preload mechanism for the porous element, holding it in position and avoiding that any fluid quantity can bypass the structure from its sides.

More advanced filters are also equipped with safety bypass valves, which allow the fluid to overcome the filtering part when this gets clogged. In such cases, the filter would otherwise cause excessive pressure drops or potential damages to the upstream components due to the rising pressure levels. Although bypass valve opening is not desired, as the fluid is no longer filtered, it ensures the preservation of the system integrity.

Figure 3.11: Schematic representation of a micro-hydraulic inline filter [10]

3.2.7 Pressure regulators

A precision pressure regulator is a device that controls the pressure setting in a pneumatic system in a very precise manner. It is an auxiliary component that reduces the inlet gas pressure and maintains a constant outlet pressure, regardless of upstream pressure changes or downstream gas consumption variations.

A regulator mainly consists of a calibrated spring, a flexible diaphragm, a feedback chamber, a valve and an adjustable handle. Its working principle is based on the continuos balance of two contrasting forces: the spring force from one side, compressed by the adjustable handle, and the downstream gas pressure, which acts on the flexible diaphragm.

As the set pressure is fixed with the adjustable handle, the spring is compressed and its force is set accordingly. The inlet gas keep flowing through the valve located beneath the diaphragm as long as the force generated by the outlet gas pressure acting on the diaphragm remains below the spring force level. Once both forces reach equilibrium, the valve settles into an indermediate position, stabilizing the outlet pressure. If the gas consumption downstream increases, the outlet pressure slightly reduces, hence the spring opens the valve a little more, letting more gas through. On the other hand, if the gas request decreases, pressure rises and the diaphragm is pushed back, closing the valve.

In a precision regulator this balancing action is extremely sensitive because it relies only on the physical interaction of mechanical components. Furthermore, the outlet gas applies pressure on the diaphragm from the so called feedback chamber, which helps isolating the regulator from all the pressure oscillations and turbolences that could influence its operation. In this sense, the feedback chamber acts as a pneumatic damper, providing the diaphragm with a mean outlet pressure value rather than instantaneous local fluctuations.

The developed test bench is equipped with R21 regulators for gaseous nitrogen. This regulator model has two pressure gauges for showing respectively the inlet gas pressure value and the outlet set pressure. Moreover, as it was mentioned in section 3.1, the regulator features also a safety needle valve, for occasionally sealing the outlet line while pressurizing the system.

A key aspect for correctly operating a pressure regulator is understanding that adjusting the set pressure handle requires a movement opposite to that of a needle valve, even though they appear very similar. This means that unscrewing the handle closes the valve inside the regulator completely, while screwing the handle increments the outlet pressure value. This feature is particularly important for safety reasons: contrarily to needle valves, where it is not possible to externally identity their state, a regulator functionality can instantly be recognized by the adjustable handle position.

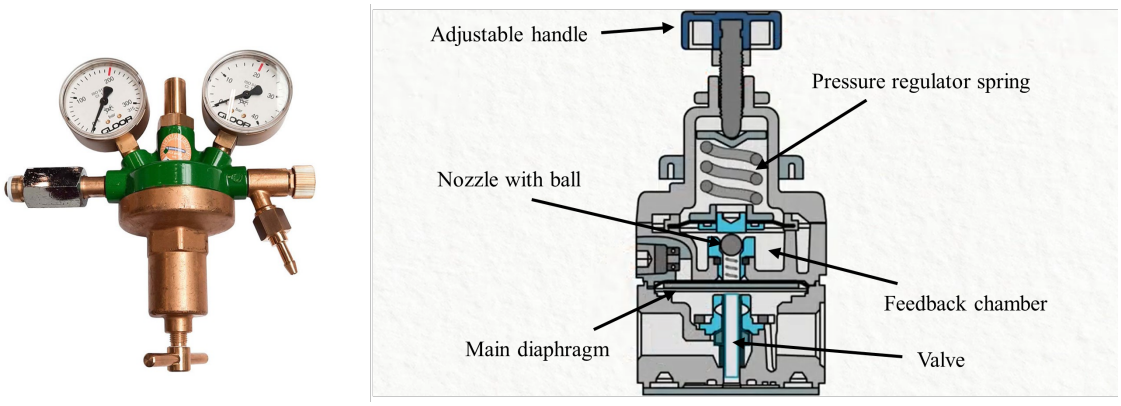

Figure 3.12: R21 N_2 precision pressure regulator [11]

3.2.8 Mass flow meters

A Coriolis mass flow meter measures the mass flow rate of a liquid which flows through it based on the Coriolis force. Inside the device, the fluid flows through a dual bent tube, as shown in figure 3.13. An exciter, typically placed at the lower part of the bend, induces a continuous oscillation of the tube. This component consists of an electro-magnetic driver coil: when it is powered with an alternate current, it generates an electromagnetic field that interacts with a magnet rigidly fixed to the tube, inducing its periodic oscillation at its natural frequency.

If no fluid is flowing through, the measuring tube oscillates uniformly and sensors located at the inlet and outlet of the component can measure the motion accurately. As the fluid starts flowing though, additional twisting is imposed on the oscillatory motion due to the Coriolis force deriving from the liquid's inertia. When this happens, the tube twisting causes the inlet and outlet sections of the tube to oscillate in different directions at the same time. The motion sensors (consisting of electromagnetic coils as well) can capture this change in the tube oscillation in terms of a phase shift, which can be directly connected to a measure of how much liquid is currently flowing through the pipe. The higher the fluid's momentum (velocity or mass), the greater the phase shift of the oscillating measuring tube, according to the following equation:

$$\dot{m} = \frac{K_u - I_u \omega^2}{2Kd^2}\tau \tag{3.1}$$

where K_u is the tube stiffness, which depends on the temperature, K is a tube geometric shape factor, d its diameter, τ is the time lag between the oscillation of inlet and outlet section of the tube, ω is the vibration frequency and I_u is the inertia of the tube.

The tube geometry play a significant role in the measurement principle. In addition to affecting the parameters appearing in the governing equation, its shape increases the Coriolis force effect and therefore the accuracy of the measurement. In fact, a vibrating curved tube imposes stronger lateral accelerations. As a result, for same mass flow rates, the oscillation distortions induced on a curved tube would be greater if compared to a straight one.

Furthermore, sensor coils can also detect changes in the oscillating frequency for measuring the flowing fluid's density, since denser liquid reduce the oscillating frequency of the tube, compared to lighter ones.

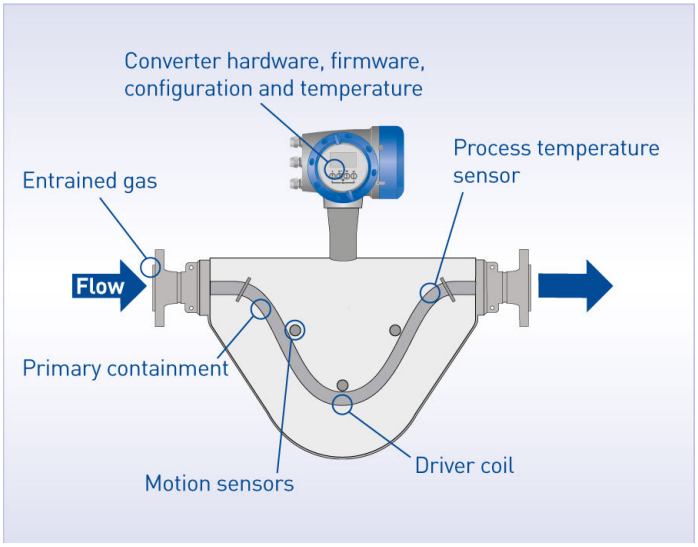

Figure 3.13: Schematic representation of a Coriolis mass flow meter [12]

In the upper part of the device it is placed the signal converter module. The mass flow meter model used in this experimental campaign is an OPTIMASS 6000F S08 equipped with a Krohne MFC400 converter module, powered by 100-230 VAC at 50/60 Hz. This element receives analogue signals from the motion sensors, which are subsequently amplified, filtered and converted in digital form.

The processed datas can then be trasmitted either as analogue signals through three 4-20 mA robust outputs, or through digital communication protocols. In particular, the MFC400 provides several digital interfaces such as HART 7, Modbus RTU and Profibus-DP, which allow the exchange of multiple measured quantities, configuration parameters and diagnostic information. [39, 40]

3.2.9 Pneumatic accumulator

A pneumatic accumulator is a pressure storage device consisting of a metallic cylinder, whose internal volume is divided into two parts by an elastic element, either a spring-loaded piston or a flexible bladder. One volume contains the working fluid and is connected to the main hydraulic line, while the other chamber contains a pressurized inert gas, such as nitrogen. Thanks to its gas side, the accumulator can respond to pressure variations in the system, serving as a pressure damper.

Its operating principle is based on the compressibility of the gas and the elasticity of the separating element. When the pressure inside the system increases, the gas pressure rises accordingly and stores energy in pneumatic form, which can be subsequently returned to the system in case of pressure drops.

By this way, the accumulator reduces pressure oscillations during system operation. Moreover, as it was detailed explained in section 3.1, accumulators are largely useful for preventing hardware damages due to sudden flow variations and water hammer effects. By providing an additional compressible volume, the accumulator attenuates these pressure peaks, thereby reducing the intensity of the transient and protecting sensitive components from damage.

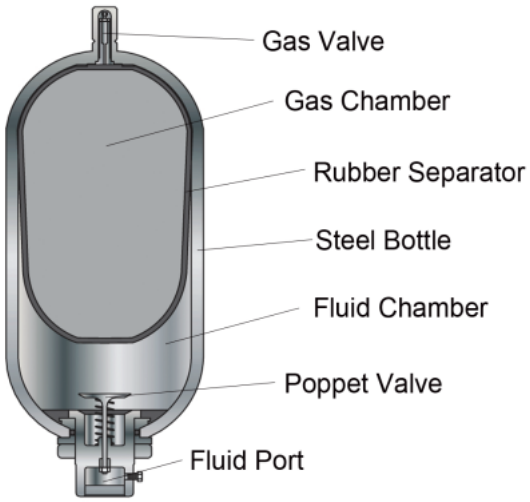

Figure 3.14: Schematic representation of a pneumatic accumulator [13]

3.3 Sensors and Data Acquisition System

Acquiring data represents the most important aspect of an experimental campaign and requires the use of appropriate sets of sensors, specifically chosen for the considered application and placed at strategic points throughout the system. Both the choice of sensor type and the selection of the measuring point are crucial for the acquisition of correct data, which ultimately determine the success of the experiment.

For this experimental campaign, three types of sensors are mounted on the test bench for acquiring data about the measurement of three physical quantities: the first sensor is the **mass flow meter** for measuring the propellants mass flow rate while conducting the test, which was directly implemented into the propellants hydraulic lines and whose functionality was detailed addressed above; in addition, for measuring pressures and temperatures at various points of the system, **pressure transducers** and **thermocouples** are respectively employed. In particular, type-K thermocouples would play a key role in determing the thermo-fluid dynamic behaviour of the combustion products inside the nozzle and the coolant flowing within the porous sample.

All instruments acquire data in the form of voltage signals, which are subsequently trasmitted to a **Data Acquisition System** (**DAQ**). The DAQ system represents the interface between the physical devices and the digital processing environment and is responsible for signal conditioning inclunding filtering, amplification and proper correction. At the end of the process, finished signals in digital form are ready to be communicated to a PC for being processed with dedicated software tools. The DAQ system, the sensors terminal pannel and the necessary power supply are all placed in a dedicated compartment (see figure 3.15) for a more accessible and pratical usage, nonetheless for a more easy transportation and positioning.

The aim of this section is to provide a detailed description of the whole measuring data setup, explaining how the chosen sensors work and how the signals are managed by the DAQ system. Ultimately, a brief presentation of the LabVIEW sotware, utilized for the post-test processing of the data, will be given.

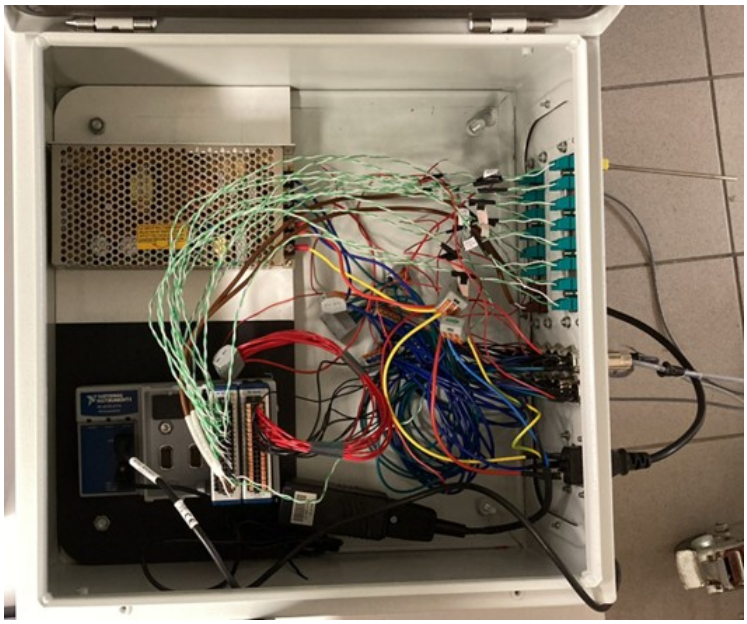

Figure 3.15: Data Acquisition System dedicated compartment

3.3.1 Thermocouples

A thermocouple is a temperature transducer capable of translating the temperature of a specific point into an electrical voltage signal. Its operating principal is based on a thermo-electric phenomenon known as the **Seebeck effect**. According to this effect, when a closed electrical circuit made of two distinct conductors welded together at both ends is subjected to a temperature gradient, an electromotive force directly proportional to the temperature difference is produced in the circuit. This can happen, for instance, when the two junctions of the circuit are maintained at a different temperature.

At a molecular level, this phenomenon can be explained by considering the behaviour of charge carriers inside a conductor. When a material is exposed to a heat source, atoms in the inside are thermally excited and the energy of the electrons is increased, allowing them to move more freely across the conductor valence band. Through this movement, electrons tend to migrate from the warmer region towards the colder one, therefore creating an electric potential difference between the two ends of the material. If the circuit consists of a single material, this effect produces equal voltages at both ends, resulting in no net measurable voltage. Conversely, if two conductors are implemented, due to their different resistivity, electrons move differently across the two conductors and different voltages occurs at each cold end under the same temperature gradient. Hence, this difference generates a measurable voltage at the colder junction of the circuit.

In 1821, Estonian physicist Thomas Seebeck observed that the voltage experimented at the cold junction of a circuit made of two different conductors is directly proportional to the temperature difference between the two circuit sides, therefore deriving the following formula:

$$V = (S_A - S_B)\Delta T \tag{3.2}$$

where V is the voltage difference, ΔT is the temperature difference and S_A and S_B are the Seebeck coefficients of the two conductors. As shown by equation 3.2, the linear trend slope depends on the difference between the Seebeck coefficients of the materials.

The **Seebeck coefficient** S of a material is an index of the material's inclination to manifest the Seebeck effect. Since this phenomenon occurs only if two distinct conductors are employed, one can only measure the Seebeck coefficient of the couple of conductors, as the ratio of the induced thermo-electric voltage to the temperature difference across the materials:

$$S_{AB} = S_A - S_B = \frac{V}{\Delta T} \tag{3.3}$$

To obtain the Seebeck coefficient of a specific material, this should be coupled with a second one whose coefficient is already known. Alternatively, superconductors can be used in an experimental thermocouple, since their coefficient is zero due to their nature, therefore the coefficient of the entire couple reflects the unknown material's one.

Depending on the pair of conductors employed, thermocouples differ both in terms of operating temperature range, sensitivity and accuracy. In this sense, different type of thermocouples exist, such as type J, E, M or N. Among them, the **type-K thermocouple** is the most commonly used for general-purpose applications. It is composed of nickel-chromium (chromel) and nickel-aluminum (alumel) conductors and allows temperature measurements in the range of -200°C to 1350°C, with a typical sensitivity of about 40 μV/°C. However, it is worth noticing that thermocouples sensitivity slightly varies with their temperature following a non linear trend, due to the Seebeck coefficients dependence to the absolute temperature (as an example, type-K thermocouples sensitivity is 42 μV/°C at 100°C, 43 μV/°C at 500°C and 39 μV/°C at 1000°C).

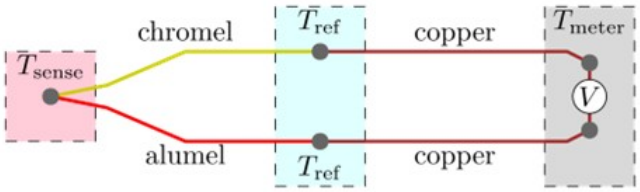

Figure 3.16: Representation of a typical type-K thermocouple circuit [14]

Figure 3.16 shows a typical circuit of a type-K thermocouple. The junction exposed to the measured temperature is also referred to as the **hot joint** and it can be either exposed directly to the warm environment or protected by a sheath. An uncovered joint provides a faster and more accurate measurement, although is more subjected to degradation. The opposite end of the circuit is called **cold joint** and represents the part of thermocouple which is subjected to the voltage difference and allows the temperature measurement.

At the cold junction, thermocouples feature two pins, which represent the extensions of the internal conductors. The device is then inserted in a dedicated terminal block, from which signals can be trasmitted to the DAQ system through conventional copper wires.

The developed experimental setup is equipped with up to 13 1/8" type-K thermocouples for measuring the temperature of the propulsive systems at different points. In particular, the new cooling system is designed for including 4 thermocouples, arranged in X-shape as explained in chapter 2, with the aim of measuring the temperature of the coolant at multiple depths within the porous structure.

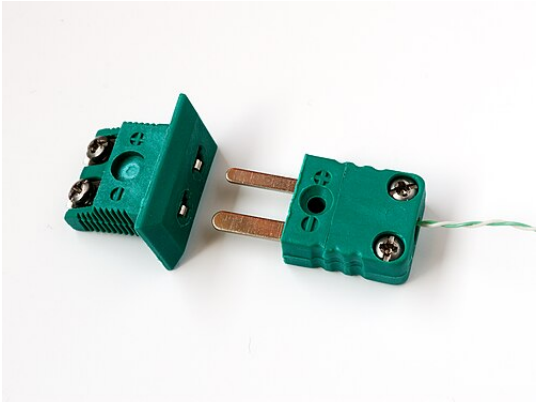

Figure 3.17: Example of a type-K thermocouple: on the right the two conductors wires (green-chromel, white-alumel) are shown, while the cold junctions pins are inserted with the correct polarity into the terminal block on the left [15].

3.3.2 Pressure transducers

A transducer is a device that actively or passively converts one form of energy into another. Among these, pressure transducers use electro-mechanical internal parts for measuring pressure with a high degree of accuracy, and then translate it in the form of a voltage or milliamps current. The most common type of pressure transducer is the strain gauge-based transducer. This type of devices typically have cylindrical shape, with a pressure inlet hole at one end that allows the local pressure to act on a thin metallic diaphragm. Here, the conversion from mechanical pressure to an electrical signal is achieved through the controlled deformation of a strain gauge.

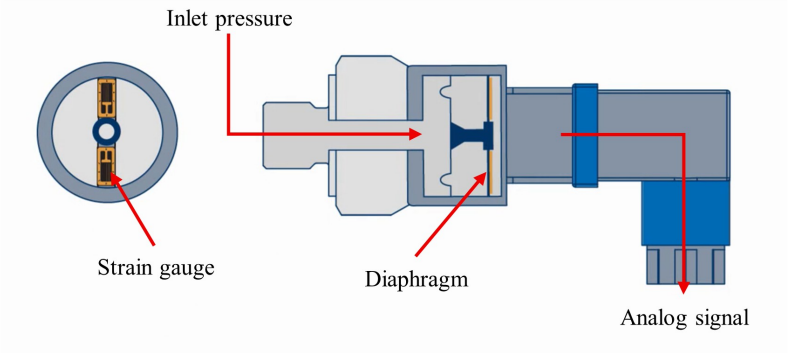

Figure 3.18: Strain gauge-type pressure transducer [16]

A strain gauge is a component consisting of a thin conductive wire, usually made of constantan, bonded to a flexible insulating substrate. When the substrate is subjected to mechanical strain, the wire follows the deformations of the material to which is attached, thus it changes its length and consequently its resistance. The resistance variation is proportional to the applied strain.

Inside the device, the strain gauge is bonded to the transducer's diaphragm. When a certain pressure is applied to the sensing port, the diaphragm deforms and induce a resistance change of the strain gauge. Usually, this change is measured using a Wheatstone bridge configuration, which allows to convert it into a measurable voltage signal. Moreover, an internal circuit is responsible of signal conditioning such as amplifications and linearization of the bridge output, providing a stable and standardized electrical signal.

Once the electrical signal is generated, it is trasmitted to the DAQ system through a proper connection. Usually, transducers implement 5-pin M12 circular connectors (norm IEC 61076-2-101), due to their high reliability and flexibility for all applications and output types. The pins are used to supply power to the internal electronics, provide the analog output signal (voltage of 0-10 V or current of 4-20 mA), and, in some configurations, enable additional functions such as

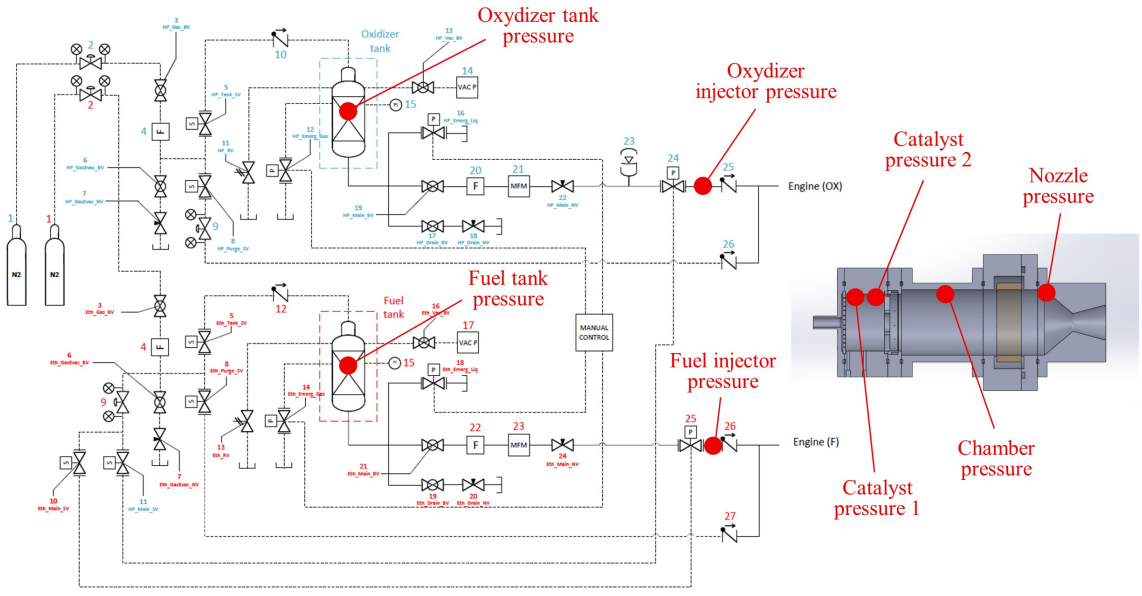

Figure 3.19: Locations of the pressure measurement points on the experimental test bench

diagnostics or secondary outputs.

The arrangement planned for this test bench features 10 pressure transducers for measuring pressure in various points of the hydraulic circuits and throughout the engine (see figure 3.19). All measuring devices are then connected through 5-pin M12 circular connectors to dedicated female receptacles installed on the DAQ compartment. On the rear side of each connector, five wires trasmit signals from the pins to the necessary hardware: two of them communicate with the DAQ module for data acquisition, while the remaining three are connected to the power supply.

3.3.3 Data Acquisition System

The Data Acquisition System is the component that collects all the measurement data of physical conditions, it converts them from analog to digital form with dedicated **analog-digital converters** (**ADC**) and sends them to a computer where they can be processed and stored. Its hardware is usually composed of a chassis and several different input modules.

The chassis permits plug and play connection of the input sensors to the PC with a simple USB port, while also controlling timing and synchronization of data transfer. The present setup employs a National Instruments cDAQ-9174 model, which is a compact DAQ USB chassis designed for small, portable sensor measurement systems. It features four available slots for C series I/O modules to create a mix of analog and digital I/O and counter/timer measurements, a USB 2.0 connection to the external host and a regional power cord for power supplying. The chassis is placed inside the sensor compartment, positioned on a dedicated PLA 3D printed support, as well as the whole compartment power supply.

For the experimental activities carried out for this MSc thesis, only two of the four available slots were actually used, mounting respectively a module NI 9213 and a NI 9202. The first module is a high-density thermocouple input module and features up to 16 differential analog input channels. Additionally, the module integrates two internal auxiliary components: anti-aliasing filters, which are low-pass filters (LPF) that attenuate high-frequency signal parts that may lead to distorted digital signals after the conversion; an open-thermocouple detection circuit, for automatically identifying a broken or disconnected thermocouple. Last but not least, the input

Figure 3.20: NI chassis cDAQ-9174 [17]

module is responsible for the **cold-junction compensation**.

Thermocouples generate a voltage corresponding to the temperature difference between their two junctions. As it was mentioned earlier, the cold junction representes a reference point for measuring the hot junction temperature and to do so it is supposed to remain at a constant temperature (hypothetically 0° C). Holding the cold junction at 0° C, though, requires using an ice bath setup, which is not practical for industrial applications. This issue can be solved by adopting the cold junction compensation technique.

This process consists of adjusting the thermocouple's voltage measurement by properly taking into account the cold junction temperature, thus avoiding the need of keeping it at a fixed temperature. To carry out the compensation, the module includes a temperature detecting device such as a **thermistor** or **resistance temperature detector** (**RTD**). This component consists of a highly thermal-sensitive resistor, through which it is possible to measure a temperature by measuring its resistance with a simple circuit and a micro-controller.

The thermistor independently measures the temperature of the cold junction (T_{cold}) and its value is summed after the analog-digital conversion of data to make sure that the voltage accurately represents the temperature at the hot junction point (T_{hot}). [41]

$$T_{hot} = \frac{V}{S_A - S_B} + T_{cold} \tag{3.4}$$

Figure 3.21: NI input modules 9213 (left) and 9202 (right) [18, 19]

The second module, a NI 9202, is a flexible solution, capable of acquiring signals for a wide range of applications. As well as the first one, the module has up to 16 differential input channels and acquires voltage signals within a range of -10 V to 10 V. The module supports a relatively high sampling rate, making it suitable for monitoring both steady-state and fast transient phenomena. Moreover, it includes configurable filters, which eliminate electrical noise originating from the system, while maintaining low latency in the signal acquisition.

In the developed experimental setup, the NI 9202 module is primarily employed for acquiring analog voltage outputs from pressure transducers and mass flow meters. For a more exhaustive description of the components specifications, refer to the official website of National Instruments [42].

3.3.4 LabVIEW software tool

LabVIEW is a program development environment produced by National Instruments which uses a graphical programming language known as **G** (from "graphic") to create programs in block diagram form. It is a general-purpose programming system with extensive libraries of functions for any programming task, such as data acquisition, instrument control, data analysis and storage. Moreover, LabVIEW includes conventional development tools that allow the user to monitor data flow within the program and do a step-by-step code debugging.

A LabVIEW program is also called Virtual Instrument (VI) because its appearance and operation resemble an actual instrument. It consists of two interactive windows, a **front panel** and a **block diagram**. The program is mainly controlled from the front panel, which serves as an interactive user interface and simulates the panel of a physical instrument. On the front panel, the user can implement knobs, push buttons, levers, graphs and other components for properly managing the VI and its execution.

The front panel features two main types of elements, **controls** and **indicators**. A control allows the user to enter data into the VI interactively as inputs, while an indicator is used for displaying outputs. There are different types of controls and indicators, depending on the data format they manage, such as integer or floating-point numbers, Boolean variables and strings.

The source code of the program is rather represented by a block diagram constructed in G language, which provides istructions to the VI for its correct execution. This diagram is composed of functions represented by icons, organised in structures and connected by wires and nodes. This also includes controls and indicators that the user adds in the front panel and will represent respectively inputs and outputs of the VI. The program can also feature complex structures and loops, or utilize sub-VI programs as special functions, exploiting the hierarchical nature of the G language.

Wires are used for carrying different types of data and are connected to dedicated terminals, which are analogous to parameters in text-based programming languages. A terminal is a specific region of a function or an element of the diagram where a wire can be connected to trasmit a data.

Figure 3.22 shows the typical arrangement of windows of LabVIEW for a VI, found among the example programs proposed on the National Instruments official website. The aim of the

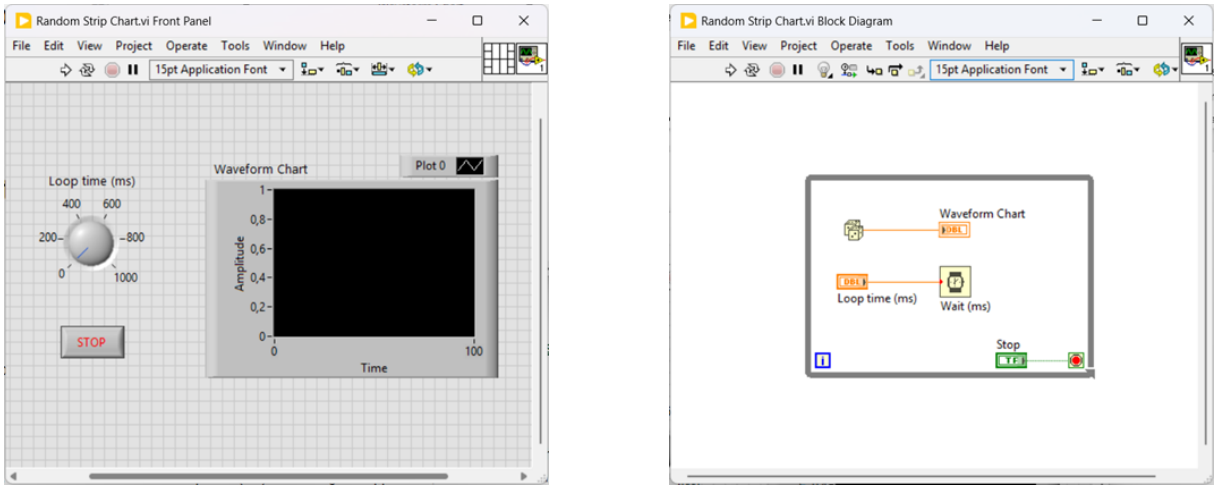

Figure 3.22: Typical view of a VI example program in LabVIEW (National Instrument example code "Random Strip Chart")

program is to generate random numbers with a specified frequency and show them on a graph. As mentioned, the front panel presents controls and indicators, respectively representing inputs and outputs of the program. In this case, there are two control devices, a regulable knob for adjusting the numbers generation frequency and a push button for shutting-off the program. Moreover, a graph is added as an indicator to visualize the output variable.

On the block diagram, the essential elements of the program are represented by icons within a while loop structure. This is due to VI logic, which is to generate random numbers until the user physically presses the STOP button. The condition to terminate the loop is defined in the bottom-right corner, where a ”Stop” control box connected to a red dot. Inside the while loop structure, a control box related to the knob on the front panel permits to regulate the delay of the loop iteration, while the dedicated functions generates a random integer number at each loop iteration and sends it to the graph to display it.

To run the VI, the user clicks on the dedicated icon on the toolbar, either from the front panel or the block diagram window, regulates the numbers frequency as desired using the knob on the front panel and arrests the program by pressing the red stop button.

In addition to general-purpose programming capabilities, LabVIEW features a set of dedicated functions for **data acquisition**, specifically designed to interface with sensors and DAQ systems. When a National Instruments DAQ device is connected to the PC, LabVIEW recognizes the hardware and makes it available within the development environment. This integration allows the user to configure data acquisition, selecting the desired input channels from the DAQ modules, defining the sampling frequency and acquisition mode (single-sample or continuous).

The acquired signals are then trasmitted into the block diagram as numerical data, where they can be processed and saved. At this scope, LabVIEW also provides tools for data logging, permitting signals to be saved to disk during or after execution. Measurement data can be written on text-format files with a structured layout, facilitating post-processing, visualization and compatibility with external analysis softwares such as MATLAB. [43]

3.4 System pressurization test

Once the entire system is assembled, all hydraulic and pneumatic lines are secured and each component is properly installed, a preliminary step in an experimental campaign is the execution of a system **pressurization test**. This necessary procedure allows to verify the correct operation of the full circuit under applied pressure. The importance of the test covers all system elements, regardless of their level of complexity and functional relevance, ranging from the integrity and proper connection of pipelines, where potential leaks or undesired venting must be identified, to the correct functioning of more delicate components such as solenoid and pneumatic valves. Moreover, the test also represents a safety validation step, ensuring that isolation devices, venting lines and relief components operate as intended.

Additionally, the pressurization test serves as an initial step towards the definition and validation of safe operational practices for the system during all phases, both regular and emergency ones. In this sense, by applying low pressure levels, it is possible to develop convenient, safe and repeatable procedures regarding pressurization, depressurization and purging of all branches of the circuit.

The test is carried out using the same pressurizing gas intended for the nominal operation of the system, gaseous nitrogen. Using an inert gas like nitrogen eliminates the risks of future

dangerous reactions inside the propellant tanks. In addition, nitrogen has a relatively lower price than other inert gases like helium.

The gas available for the pressurization test is stored in a single vessel, kept at a pressure of approximately 110 bar. Consequently, only one propellant line can be pressurized at a time. On the other hand, this configuration permits a more controlled verification of individual lines and their components, without the need to account for the remaining part of the system.

The system pressurization procedure starts with the connection of the gas vessel to the pipeline. The following process involves the same steps for both propellant sides and is carried out in an analogous manner. Before starting pressurizing, it is important to check that all manual valves (both ball and needle valves) are safely closed. Once everything is ready, pressurization starts from the valves located on the top of the vessel. As it was explain in detail in section 3.1, the gas vessel is equipped with a main needle valve and a pressure regulator, which features an incorporated needle valve itself. This configuration forms a series of successive safety measures that protects from the danger of very high-pressure gas.

The procedure requires first the opening of the vessel main needle valve, while keeping both the pressure regulator and the second needle valve closed. The inlet pressure can be visualized from the first pressure gauge mounted on the top of the regulator. Then, next step consists in chosing the desired output pressure with the pressure regulator and subsequently slowly opening the second needle valve, thus starting the pressurization of the first part of the line.

Once the ball valve 3 (see the whole system P&ID in figure 3.2 for a better understanding) is open and the first branch is no longer isolated from the rest of the circuit, pressurization of the remaining part of the system can proceed.

A fundamental part of the pressurization test is ensuring the correct operation of the solenoid valves, since their actuation covers the three principal functions required during a test sequence, namely tank pressurization, propellant supply and purge execution. The valves actuation is electrically governed from the PLC, either automatically or manually. For distinctly testing the devices, since a precise and punctual control of them is required, a ladder logic program was prepared on the KGLWIN software specifically for this application. In fact, the PLC compartment features three on/off switches, each one related to a certain solenoid valve for acuating it at desire.

Another delicate component whose functionality needs to be ensured is the pneumatic valve. In the developed test bench are implemented six pneumatic valves, two of them are responsible for the propellants supply and are actuated by the injection of gaseous nitrogen through the opening of two solenoid valves, while the rest of them are emergency valves for occasionally evacuate the tank in dangerous scenarios.

Since the propellant supply pneumatic valves require a sufficiently high pressure in the system for being actuated, the input pressure for the test was increased to approximately 8 bar. The test confirmed the correct operation of all solenoid and pneumatic valves, effectively opening the main propellants supply lines. The remaining pneumatic valves are powered differently. Since their usage is required only for emergency conditions in which a power outage could occur, valves are powered with the continuous supply of pressurized air. Their actuation is thus controlled from a remote compartment with four manual ball valves. The correct functionality of these valves was tested during the first depressurization procedure.

The pressurization test primarily highlighted two types of problems. First of all, in some cases it evidenced the lack of operativity of some valves due to a incorrect installation orientation.

As it was discussed in the previous sections while describing valves operating principles, each valve has a particular internal geometry which allows the fluid to flow only if installed in the correct direction. Performing tests at very low pressure levels is essential for identifying this type of installation error at an early stage.

The second evidenced issue regarded vents and leakages in certain points along the lines, especially at connections between pipeline segments. In a pressurized hydraulic system, a leakage can be sensed by audible hissing sounds or vibrations of the metallic structure and it can be subsequently highlighted with the use of a simple soap foam. By spraying some soap on the suspected leakage point, at the contact with pressurized gas, this creates little droplets which better indicates the exact venting location. The test evidenced leakages problems mainly at manifold connections, which were promptly eliminated by better tightening the parts together.

The pressurization test concludes with the complete evacuation of all gas trapped into the system, namely the full **depressurization** of the pipelines. This procedure is as critical as the pressurization phase and must be carried out with the same level of care. To stop the pressurized gas supply, the sequence of steps requires closing the vessel main needle valve, the pressure regulator and the second needle valve in this order. Then, with the solenoid valve controlling the tank pressurization closed, the depressurization of the upstream branch can be carried out by opening the dedicated venting valves. Tank gas evacuation can also be conducted through the discharge lines. As it was mentioned, both ordinary and emergency lines were tested during this process. The tank depressurization permits to eliminate also the remaining gas trapped into the propellant main line.

When considering a pipeline in which a couple of ball valve and needle valve are installed, a useful practice for properly evacuate all gases is to follow a precise sequence of steps. Along the line, the gas encounters first the ball valve and then the needle valve. The recommended approach is to slowly open the ball valve first and then slightly open the needle valve. By this way, gas is vented without the risk of inducing dangerous vibrations on delicate components of the test bench and excessive noise. Once the pressure within the pipeline is sufficiently decreased, the needle valve may be opened completely so that the remaining gas can easily escape. Additionally, at the end of the process, it is always recommended the multiple actuation of the ball valve, since small quantity of pressurized gas can remain trapped in the space inside the valve's ball.

The described test was carried out multiple times, with progressively increasing pressure levels. This approach allowed to familiarize with the system, which proved useful for the development of the **Standard Operating Procedure** (**SOP**) document for the subsequent water flow test. This document is a necessary paper for every type of experimental activity because it contains the precise steps order for safely carrying out the experiment. A brief presentation of the prepared SOP for water flow test will be given in chapter 4.

Chapter 4

Water flow test

Once the test bench is completed and a few pressurisation tests are carried out for confirming the correct operativity of all valves and pneumatic devices, the research project moves on to the execution of a test for the experimental assessment of the porous wall permeability, in which the objective is to find the actual empirical correlation between the mass flow rate transpiring through the lattice and the pressure drop occuring between the wall sides. The need of deriving an experimental correlation for this structure comes from the difficulty of calculating the permeability of a precise and complex lattice from existing formulas, which have factors depending on the geometry and the flow regime.

To carry out the experiment, the cooling system assembly is mounted on the test bench and simple tap water is injected. During the execution, the injected water mass flow rate is measured via multiple ways, meanwhile the pressure difference across the wall is calculated as the difference between a pressure measured upstream of the injector (with a transducer) and the atmospheric one. By carrying out various test sequences with different pressures inside the tanks, the experiment should provide mass flow rate data related to multiple pressure drop values, namely the porous wall permeability.

This chapter focuses on describing the objectives and motivations behind the experiment, explaining how the desired results are intended to be obtained. Subsequently, it describes the preparation of the test bench and the execution of the experiment, including possible inconveniences that may occur during an experimental project, and ultimately discussing the test results. The assessed permeability will then be employed as input in chapter 5 within the modelling and simulation process of the cooling approach.

4.1 Objective of the experiment

When assessing the functionality of a porous component like the one employed in the investigated transpiration cooling system, one main property to consider is the wall's **permeability**. The word permeability refers to the ability of a material of letting a fluid passing through it. The factors influencing this feature are related to the microscopic structure of the porous medium. In particular, the dimension of the pores inside the material, namely its **porosity**, and how well pores are interconnected to each other within the internal structure largely influence its value.

The most common relation that describes the flow of a fluid in a porous medium is the **Darcy law**. This law was formulated by French engineer Henry Darcy in 1856, based on the results

of experiments of water flow through the sand. By conducting a certain number of experiments under various conditions, Darcy discovered a mathematical relationship between the steady-state mass flow rate of water ($\dot{m}$) and the pressure difference of the fluid at both sides of a sand filter (Δp). This relation also depended on the geometrical shape of the filter, in particular its length (L) and cross section (A):

$$\dot{m} \propto -\frac{\Delta p}{L} A \tag{4.1}$$

The relation shows that the water mass flow rate across the sand filter is directly proportional to the pressure difference. In the experiment, the pressure is measured using water filled tubes known as piezometers. The elevation of the water level in the piezometer is referred to as hydraulic head and, as in mercury manometers, is related to the water pressure. Hence, the water pressure difference is computed as the difference in hydraulic head between two locations at each side of the filter. Additionally, the negative sign in the equation derives from the convention of defining a positive volumetric flow rate in the direction of a negative change in head (i.e., head decreases in the direction of flow). [44, 45]

Darcy observed that the ease with which water crossed the filter was changing with the character of employed sand, meaning that different filters with various materials implied different water behaviours, even though the proportionality relation stood. This effect was enclosed in the proportionality constant of the relation, which took the name of permeability and expresses the ease with which a fluid flows through the material:

$$\dot{m} = -K \frac{\Delta p}{L} A \tag{4.2}$$

However, this expression implies several limitations in the system model, regarding multiple aspects. Its validity, essentially, covers incompressible and isothermal flows with low velocities. For quantifying this limitation, the Reynolds number computed with the scale of the pores within the material must be below unity. Moreover, the relation applies for Newtonian fluids through a relatively long, uniform and isotropic porous medium of low permeability.

Over the years, various corrections of the equation were proposed with the scope of increasing its range of validity. For example, Hazen in 1893 proposed a corrected form of the equation with an added dependence on the fluid's viscosity and temperature. This effect was not considered by Darcy's first experiments since he focused only on the use of a single fluid and did not compare the results with other ones. The proposed modification is:

$$U = \frac{\dot{m}}{A} = \left(\frac{T + 10}{60} \right) K_{ref} \frac{\Delta p}{L} \tag{4.3}$$

where U is the fluid velocity (also known as the **Darcy's velocity**) and K_{ref} is the medium's permeability at a reference temperature in °F. In addition, Kozeny and Carman in 1927 derived a different expression for taking account of the fluid-viscosity dependence of Darcy equation in the case of creeping flows. They associated the Poiseuille's theory of flow through capillaries with Darcy's empirical law. By assuming a uniform pressure drop across the medium and integrating Poiseuille's partial differential equation along a certain capillary length, an equation similar to the Darcy law is obtained:

$$\frac{A}{8\pi\mu} = U \frac{L}{\Delta p} \tag{4.4}$$

The analogy with Poiseuille flow allows the interpretation of the Darcy equation as a balance between pressure and viscous stresses, thus supporting Hazen's theory on the fluid viscosity

effect.

A second, more important limitation for the investigated application of the Darcy law is the inertia effect, occurring when faster flows are considered. As mentioned, the Darcy law is valid only for so called creeping flows in which the fluid's velocity and thus its inertia is negligible. When pores-scale Reynolds number increases, a non linear version of the Darcy law may be applied, with the implementation of the **Forchheimer correction**:

$$-\nabla \vec{p} = \frac{\mu}{K}\vec{v} + \beta\rho \left|\vec{v}\right| \vec{v} \tag{4.5}$$

This version of the law contains the conventional viscous term from the original Darcy law, plus a non linear inertial term, depending on the fluid's viscosity, its velocity and a Forchheimer factor related to the porous medium internal structure. [46]

The described corrections are only a few of the possible versions of the Darcy law, and finding the right version of the formula for a particular application with precise operation conditions remains a difficult task. The necessity of knowing precise correcting parameters depending on the porous medium geometry, thus required the execution of an experimental evaluation of the chosen part permeability.

As discussed in chapter 2, the porous wall considered for this experimental campaign consists of a metallic lattice, obtained from the repetition of a cubic cell with face centered holes. The fluid flows from the outer diameter of the lattice towards the inner one, crossing a total length of 7 mm. The short length of the porous medium and its precise geometry compromise the Darcy law validity. However, due to the cylindrical shape of the lattice, the coolant flows through the pores in radial direction. These internal spaces, hence, act as linear orifices, for which a similar equation stands:

$$\dot{m} = C_d A \sqrt{2\rho\Delta p} \tag{4.6}$$

where $C_d A$ is a discharge coefficient, which depends on the orifice geometry. The nature of the relation resembles the Forchheimer version of Darcy law, where the inertia effect is considered with a quadratic dependence of the fluid's velocity. This formula therefore represents a valid alternative to the Darcy law for cases featuring relatively fast flows and high pores Reynolds number (**turbulent flows**) or high permeability values. Due to the high pressure drop occurring across the porous wall, this equation seems most suitable.

The discharge coefficient remains the only unknown parameter. For assessing the relation between the coolant mass flow rate across the porous wall and the imposed pressure difference, a test was carried out, using water as working fluid. The water flow test, hence, has the objective of experimentally assessing the actual permeability of the chosen porous wall. The test results will serve as input for the subsequent numerical simulation of the transpiration cooling operation, for computing the transpiring coolant mass flow rate as a function of the difference between the coolant inlet pressure and the chamber pressure.

4.2 Preparation of the experiment

To assess the porous wall experimental permeability, water is injected in the cooling system with the objective of measuring its mass flow rate as a function of the pressure difference imposed across the structure. By running the experiment multiple times with different coolant pressure

levels, it is possible to graphically represent the test results, derive a general trend of data and extrapolate its slope, namely the dicharge coefficient of the porous wall, which corresponds to the permeability extent.

The water mass flow rate will be measured in two different ways, with the ojbective of obtaining a more reliable result. The first measurement is accurately carried out by the Coriolis mass flow meter installed along the propellant line. Due to the mass flow rate conservation for steady-state conditions, the mass flow rate measured by the device should match the value at the porous wall location (although some differences are expected due to the lack of absolute steady-state conditions). The second measurement is carried out by collecting all the water coming from the cooling system, weighting it and dividing the total mass to the experiment duration time. By this way, a mean mass flow rate value can be assessed. If the experiment has a sufficiently long duration with negligible water losses during its collection, both results should be fairly similar.

In addition to the intended tests described above, similar executions involving minimal modifications to the setup will be performed also for veryfing the uniformity of the assessed global permeability. For this purpose, water is collected only from a portion of the porous wall, from which it is possible to obtain a measurement of local permeability. To do so, additional parts were 3D printed and connected to the cooling system assembly. In particular, three additional components were produced: a rotating ring, a curved collector designed to fit in the hole placed at the centre of the ring, a flange for locking the parts together with the rest of the system. The complete assembly is represented in figure 4.2.

The collector is made waterproof by multiple external PLA layers and is designed to perfectly adhere at the internal surface of the porous wall, limiting the amount of water losses. On its other end, a G thread is also added for extending the pipe and easily collecting water in a container. In addition, the whole system can rotate, allowing to measure the local permeability in different

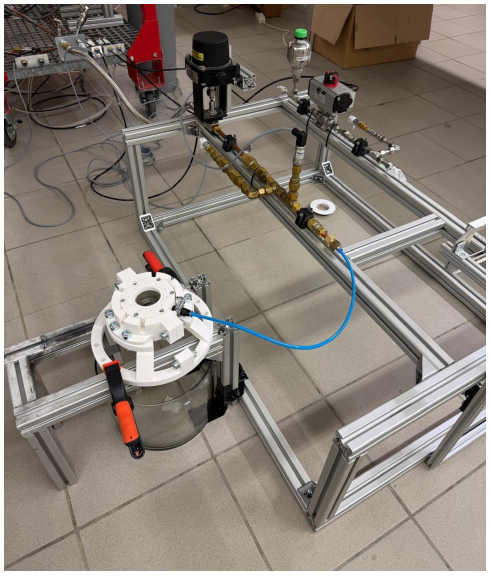

Figure 4.1: Structural support for the cooling system, prepared for the execution of the water flow test. The structure is attached to the side of the test bench and the support is held to the structure with two pinches. Water is injected from the lateral injector of the system and is then collected from below. At the end of the fuel line, after the pneumatic valve, a pressure transducer is also mounted for measuring water injection pressure.

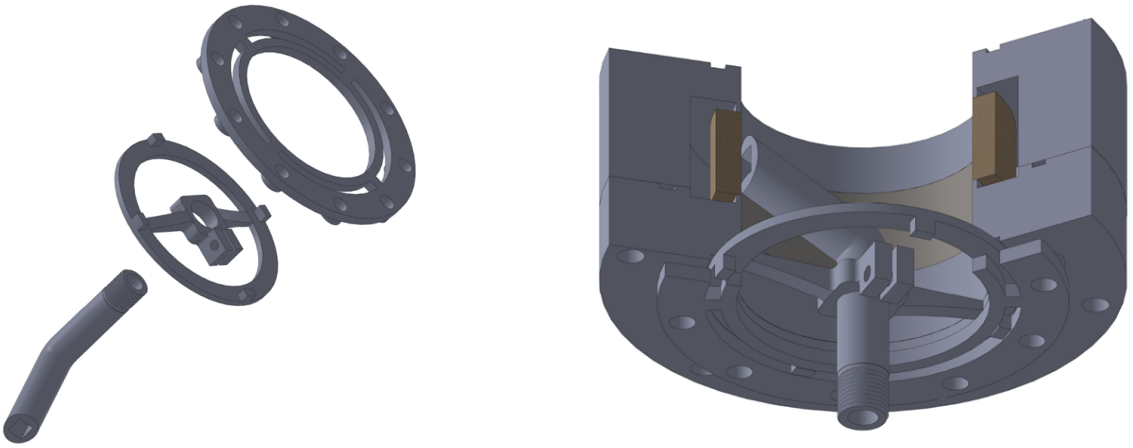

Figure 4.2: Additional parts printed for measuring lattice local permeability

positions of the lattice.

For carrying out the experiment, the test bench has been prepared similarly to what was done for the pressurization test. The only new feature is the addition of the cooling system at the end of the propellants lines. The cooling system is placed on a dedicated structure, built with square-section metallic beams and placed alongside the test bench. To provide a more stable positioning, on top of this structure, the system was secured to a PLA 3D-printed support, designed specifically for this application. This support is held to the structure below by two pinches. The whole structure weight, in fact, guarantees enough stability, if considering that pressures applied will not be excessively high. The whole arrangement is shown in figure 4.1.

As for the pressurization test, one single nitrogen vessel was employed, since only one propellant line is necessary for the experiment execution. In particular, it was chosen the fuel line for providing water to the cooling system. This choice allows the usage of simple tap water which is perfectly compatible with ethanol and whose residuals would not cause any problems inside the tank. On the contrary, the hydrogen peroxide line would have required the usage of deionized or demineralized water (or DI water) for avoiding possible undesired reactions with the peroxide or its slight decomposition.

As mentioned before, for obtaining an acceptable representation of the mass flow rate trend with the pressure difference, a high number of tests with various coolant pressure levels is required. Due to the restrained amount of water available in the tank, it is convenient to carry out test executions with a not excessive duration. On the other hand, the water flow inside the porous wall should persist for a sufficient amount of time for the conditions to be defined as steady-state. A good trade-off for these requests is a total injection of water of 5 seconds. By this way, properties inside the lattice have enough time to stabilize and the number of tank refill procedures is sufficiently reduced.

For carrying out a 5 seconds water flow test, a specific sequence of inputs for opening solenoid valves is created with the help of the KGLWIN software. Figure 4.3 represents an explicative graph of the test sequence, meanwhile figure 4.4 shows the related ladder program on KGLWIN. The whole sequence is initiated by turning the main P00 switch on from the PLC compartment box. After a 5 seconds initial pause, the tank solenoid valve opens for pressurizing the tank. Precisely, tank pressurization can be performed manually by controlling the opening of the tank

solenoid valve with the P04 switch. This allows to make sure that the pressure tank is always at the correct value and can be adjusted regardless of any test sequence. A 5 seconds-pressurization was also inserted at the beginning of the sequence to adress for any pressure losses that may be occurred during previous procedures or executions.

After 5 seconds from the beginning of the pressurization, the ethanol main solenoid valve opens and water injection starts. At the end, a 1 second purge procedure is also added. This part was inserted as a further proof of correct functioning of the related solenoid valve rather than an actual system purging, since the purge line is not in communication with the propellant circuits.

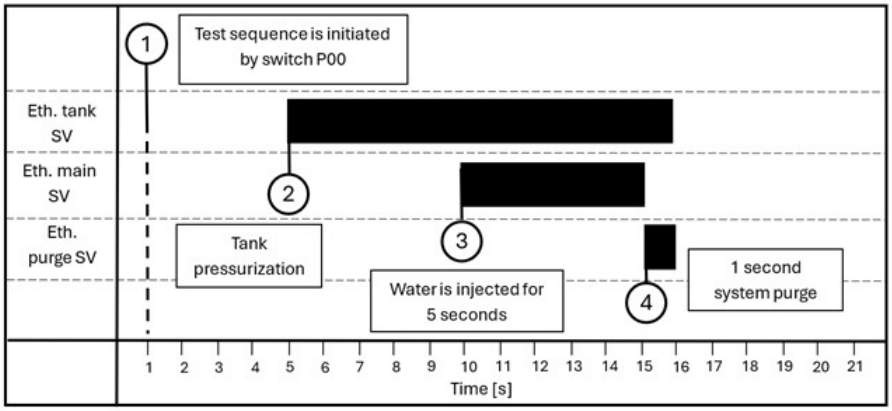

Figure 4.3: Water flow test sequence

For the acquisition of the necessary data, other than the mass flow meter (which is connected to the AI3 channel of the NI 9202 module), on the test bench were implemented two pressure transducers: the first (connected to the AI0 channel) is mounted on the ethanol tank for measuring the tank pressure, while the second one (connected to the AI2 channel) is mounted downstream of the fuel supply pneumatic valve for measuring the water injection pressure (which is visible in figure 4.1). The second value is particularly important since it serves as reference for the creation of the permeability graph, in which the difference of pressure between the two wall sides is considered. Moreover, even though temperature measurements are not necessary for this application, a thermocouple was still mounted on the system for a data acquisition test.

The sensors are connected to the DAQ system in the dedicated compartment and thus to the laptop, where data can be registered with a specific LabVIEW program. This program is designed following a general logic for allowing also the post-processing of thermocouples data, making it suitable for an eventual hot-fire test too. The mass flow meter data, on the other hand, are measured in the form of voltage signals as well as pressure transducers and are acquired from the NI 9202 module of the DAQ system.

Before initiating the test sequence from the PLC compartment, the data acquisition program must be started from the ”Run” button. Two DAQ Assistant functions acquire data from the DAQ module channel with a ”continuous samples” mode at a frequency of 1 kHz. Results are then shown on the program Front Panel on two different indicators (one for the voltage values, namely pressures and the mass flow rate, one for temperatures) and are saved on a text file whose name and directory can be specified at the beginning of the sequence. A red stop button on the Front Panel, then, permits to terminate the data acquisition at the end of the sequence.

An important and necessary step before running the actual experiment consists in the **sensors**

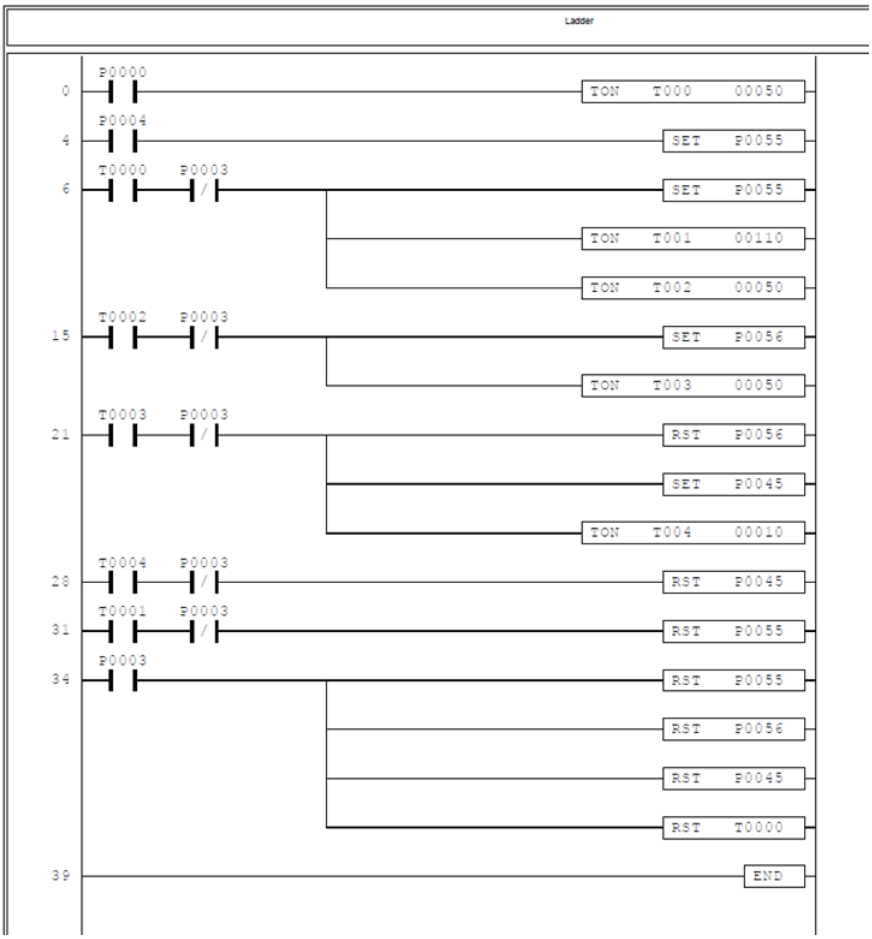

Figure 4.4: Ladder program on the KGLWIN software for the execution of water flow test sequence

calibration. Prior to the beginning of the experiment, when the system is still depressurized and has no water in it, the data acquisition program is run for a few seconds for acquiring pre-test data for sensors calibration. In fact, all transducers detect a mechanical force and send a voltage signal proportional to this value within a certain range. Pressure transducers employed for this experimental campaign can measure pressures between 0 and 40 bar, sending out an output signal value within 0 and 10 V. However, due the device functionality, a certain data offset is always present and must be identified before the actual experiment.

The transducer calibration was carried out by acquiring the sensors voltages corresponding to the atmospheric pressure value. This procedure is also referred to as ”single-point calibration”. In fact, one single pressure value was used as reference for the calibration. This approach is acceptable for an experimental activity, even though a two-point calibration is considered to be more accurate. Conversely, as second necessary information for deriving the sensor conversion formula, its sensitivity was considered constant at the nominal value (0-40 bar, 0-10 V $\rightarrow$ 4 bar/V). As a result, the transducer's data conversion formula follows a linear model:

$$p = a \cdot x + b \tag{4.7}$$

where $a = 4$ bar/V is the sensor's sensitivity considered constant at the nominal value, while b is the offset value measured with the pre-test. For example, from the calibration procedure, a pressure transducer provided a voltage value of 0.0231 V corresponding to atmospheric pressure.

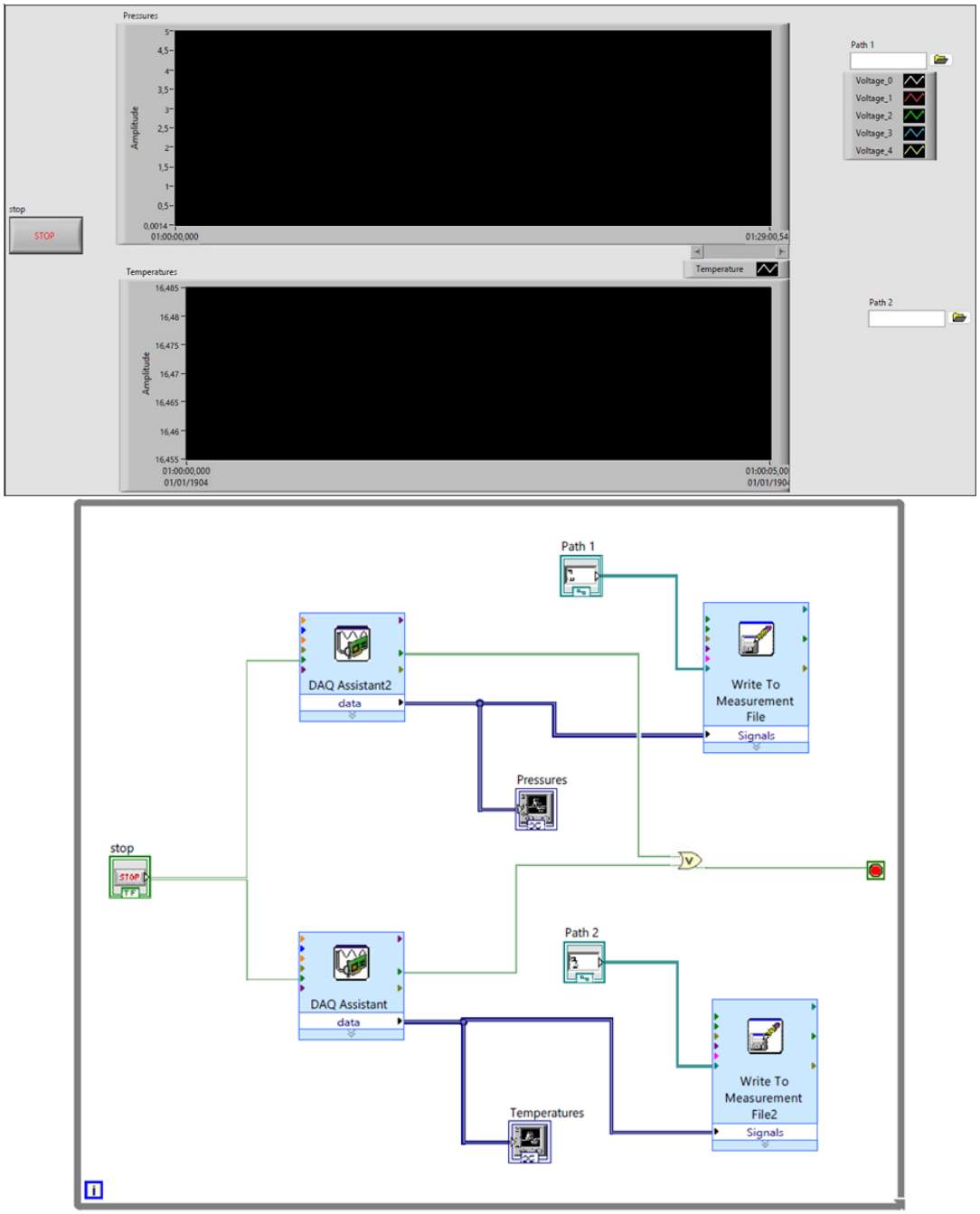

Figure 4.5: LabVIEW program for data acquisition and save

From equation 4.7 it is possible to obtain:

$$1 \text{ bar} = 4 \text{ bar/V} \cdot 0.0231 \text{ V} + b \quad \rightarrow b = 1 \text{ bar} - 4 \cdot 0.0231 \text{ bar} \tag{4.8}$$

Consequently, equation 4.7 may be rewritten as:

$$p = 4 \text{ bar/V} \cdot (x - 0.0231 \text{ bar}) \tag{4.9}$$

An analogous conversion formula was implemented for each sensor, based on the measurement value got from the calibration procedure.

Finally, a conventional practice for the proper and safe execution of an experimental activity is the preparation of a document, which will serve as a guide for everything related to the test, called **Standard Operating Procedure** or **SOP**. Even though there is not a standard path to follow for the preparation of this document, it is recommended to insert every information regarding the experiment that may be useful for the operation.

The written SOP includes a description of the activity, its objective and an explanation of how results will be acquired. Moreover, it contains important safety-related informations such as emergency shutdown procedures for the entire system, precise responsives in case of emergency situations, an hazardous checklist for listing possible dangerous substances involved in the experiment (however for the water flow test no hazardous feature is reported), a description of the test site for fire extinguishers positions and for carrying out emergency evacuation procedures or a list of the necessary safety equipment.

Intuitively, the SOP also presents an accurate description of the whole test setup with associated pictures and schemes. Last but not least, it is provided a complete checklist of all necessary steps for carrying out every part of the experiment, from the test bench preparation and pressurization to the system purge. This information ensures a safe execution of the activity, since this checklist accounts for all possible dangerous features and emergency condition, preventing the risk of improvisations. By following a predefined and structured sequence of steps, the test can be carried out in a controlled and repeatable way, reducing the likelihood of human error and unforeseen issues. All steps are defined in advance, allowing potential risks to be carefully evaluated and mitigated before the actual execution of the experiment.

4.3 First experiment execution and results

The experiment was executed two times. For the first execution, in fact, the cooling system's metallic housing was temporary not available due to necessary machining modifications. This part was therefore replaced with an identical PLA 3D-printed replica. Even though the component is identical in every aspect to the metallic part, it was preferred to repeat the experiment a second time, featuring the actual component, for results confirmation. Both experiments were executed in the TU Dresden ILR/WIK Wind Tunnel Laboratory. This section focuses on the execution of the first experiment and the presentation of the results.

The activity began with the preparation of the test bench and the connection of all solenoid valves and sensors to their dedicated compartments. All wiring and connections were completed before connecting the system to the external AC power supplier, in order to avoid electrical shocks hazards. Then, the sequence program was set on the KGLWIN software and uploaded on the PLC, as well as the LabVIEW program for data processing.

The first experimental step to carry out is the calibration procedure of the pressure transducers. At this scope, as it was explained in the previous section, the LabVIEW program was run for a few seconds, registering data coming from the transducers relative to atmospheric pressure. This results were later used as reference data for correcting the sensors signals offset.

Subsequently, the ethanol tank was filled for the first time with tap water using the vacuum pump (the refill procedure was explained in detail in section 3.1). Hence, the whole system was pressurized to the first pressure level relevant for the experiment.

The porous wall global permeability was assessed first. For obtaining a sufficient amount of results and therefore creating a precise data trend, tests were run with pressure levels ranging from 6 bar to 16 bar with a 2 bar interval. For each pressure value, 3 tests were carried out in

Step	Classification	Contents	Check
1	Pre-check	Check safety precautions in advance	
2	Cooling system assembly and installation	Cooling system assembly	
3		Secure the cooling system on the dedicated PLA supports	
4		Secure the supports on the test bench structure	
5		Connect the main water line to the lateral injector on the cooling system	
6		Place the water collector bucket below the structure	
7	Electronics connection and system preparation	Connect pressure transducers to measuring points and to the sensors compartment	
8		Connect solenoid valves to the PLC compartment	
9		Connect PLC and sensors compartments to the laptop	
10		Set up the KGL (upload program on the PLC) and LabVIEW programs on the laptop for system monitoring	
11		Connect all electronics to the power supply (sensors and PLC)	
12		Connect emergency pneumatic valves to the manual pneumatic controller and to the external pressurized air supplier	
13		Optional: check solenoid valves operativity with a dummy PLC program	
14	Tank filling	Check valves Eth_Tank_SV, Eth_Emerg_Gas, Eth_Emerg_Liq, Eth_Main_BV and Eth_Drain_BV to be closed	
15		Attach vacuum pump to the tank, open valves Eth_Vac_BV, Eth_Drain_BV and Eth_Drain_NV and fill the tank	
16		Close Eth_Vac_BV, Eth_Drain_BV and Eth_Drain_NV	
17	Sensors calibration	Run LabVIEW program and acquire transducers data for sensors calibration (acquired value represents atmospheric pressure)	
18	System pressurization	Check ALL valves to be closed	
19		Open the gas vessel main valve, regulate output pressure with the pressure regulator and open the gas vessel needle valve	
20		Open Eth_Gas_BV	
21		Open Eth_Tank_SV to pressurize the tank until desired pressure value, then close Eth_Tank_SV	

Figure 4.6: Checklist for the preparation of the test setup from the Standard Operating Procedure document

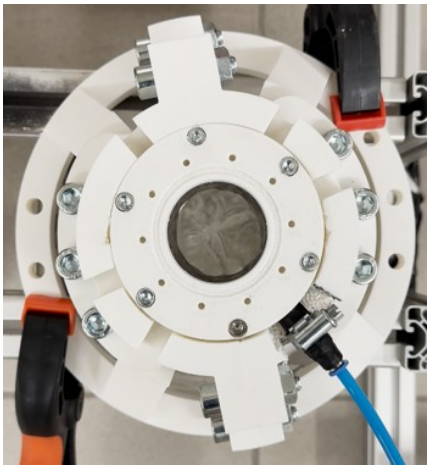

Figure 4.7: Water injection during a global permeability assessment test sequence

order to improve the stastistical reliability of the results. This approach allowed the identification and rejection of outlier measurements originating from inaccurate test conditions. In particular, data affected by the sudden depletion of water in the tank were discarded. Moreover, data from the first test execution following a tank refill were always excluded, due to the vast amount of gas trapped into the propellant line. Additionally, measurements produced during initial procedure trials were also discarded, as they were intended only for preliminary system verification.

The test procedure was carried out by following the steps listed in the figure below:

Step	Classification	Contents	Check
1	Preparation	Set Data files names in the LabVIEW program	
2	Test execution	Run LabVIEW data acquisition	
3		PLC switch P00 ON for starting sequence and collect water from the system	
4		PLC switch P00 OFF when sequence ends	
5		Stop LabVIEW data acquisition	
6		PLC switch P04 ON for opening Eth_Tank_SV and re-pressurizing the tank for next test	
7	Measurement	Set scale tare and measure collected water mass	
8		Compute mean mass flow rate by dividing by execution time (5s)	

Figure 4.8: Checklist for the assessment of the porous wall global permeability

The tests demonstrated the correct functioning of the cooling system and its architecture. In fact, despite the water being supplied from a single inlet, it seemed to uniformly distribute inside

the housing and around the porous cylinder, ensuring homogeneous injection at the centre of the system (as shown in figure 4.7).

After assessing the porous wall global permeability, the additional parts for measuring the local permeability of the component were mounted on the structure. Hence, three sequences were carried out for measuring the local mass flow rate coming from three distinct locations of the porous wall.

These tests were executed with a tank pressure of 12 bar. During each test, the water coming from the investigated location was collected into a beaker using a flexible tube, while the remaining flow was collected in a container, similarly to the global permeability tests. The objective in this case was to evaluate the local mass flow rate as a percentage of the global one and compare the results obtained at different locations.

After the last local permeability test sequence, the experiment is concluded and the system can be depressurized by opening the dedicated purge lines, while the remaining water was drained from the tank. In addition, a further test sequence is run with no pressure inside the pipelines in order to remove any residual water that might have remained trapped in the last section of the line.

The sensors mounted on the test bench acquired data which were subsequently saved by the LabVIEW program in separated text files. Each test sequence produced two text files. The first one contains the voltage signals sent by the transducers and the Coriolis mass flow meter, arranged in five distinct columns. In fact, in addition to the two necessary transducers, two

Step	Classification	Contents	Check
1	Set up laptop	Set Data files names in the LabVIEW program	
2	Test execution	Run LabVIEW data acquisition	
3		PLC switch P00 ON for starting sequence and collect water from the system	
4		PLC switch P00 OFF when sequence ends	
5		Stop LabVIEW data acquisition	
6		PLC switch P04 ON for opening Eth_Tank_SV and re-pressurizing the tank for next test	
7	Measurement	Set scale tare and measure locally collected water mass	
8		Compute mean local mass flow rate by dividing by execution time (5s)	
9		Measure total collected water mass and compute mean total mass flow rate	
10		Compute the local/total mass flow rate ratio	

Figure 4.9: Checklist for the assessment of the porous wall local permeability

5.3 System's pressure change

Step	Contents	Check
1	Close Eth_Gas_BV and Eth_Tank_SV	
2	Regulate the vessel's output pressure with the pressure regulator	
3	Slightly open Eth_Gas_BV	
4	Open Eth_Tank_SV until tank pressure reaches the desired value	
5	Close Eth_Tank_SV and open Eth_Gas_BV	

5.4 Tank refill

Step	Classification	Contents	Check
1	Venting the system	Close Eth_Gas_BV and Eth_Main_BV	
2		Run execution for venting gas in the final section of the line	
3		Open Eth_GasEvac_BV and then Eth_GasEvac_NV for venting the first part of the system	
4		Vent the tank by opening Eth_Vac_BV	
5	Tank filling	Attach vacuum pump to the tank, open valves Eth_Drain_BV and Eth_Drain_NV and fill the tank	
6		Close Eth_Vac_BV, Eth_Drain_BV and Eth_Drain_NV	
7		Open Eth_Main_BV	
8	System re-pressurization	Close Eth_GasEvac_BV and Eth_GasEvac_NV	
9		Open Eth_Tank_SV and slightly open Eth_Gas_BV to slowly pressurize the tank	
10		Close the Eth_Tank_SV when the desired tank pressure is reached	

Figure 4.10: Checklists for respectively regulating the experiment pressure and refilling the tank with new water

additional ones were connected to the DAQ system but were not mounted on the test bench and therefore measured the atmospheric pressure in the laboratory. Each column, hence, features the signals acquired by a specific sensor, with a sampling frequency of 1 kHz.

The second file contains the temperature values provided by the single thermocouple employed in the experiments. Similarly to the unused pressure transducers, this device measured the ambient temperature inside the laboratory during each test sequence, although its data are not relevant for the scope of the experiment.

Resulting values were then processed using a MATLAB script, which corrected them by considering the calibration pre-test results and implementing equation 4.7. The sensors data from the calibration procedure were also saved in similar text files by the same LabVIEW program prior to the experiment. The post-processed data can then be represented on a MATLAB graph, thus showing the properties evolution throughout the test sequences. With reference to this,

25	Experiment termination and gas evacuation	Close the vessel main valve	
26		Close the vessel pressure regulator and needle valve	
27		Close Eth_Main_BV	
28		Vent the tank by opening Eth_Vac_BV	
29		Drain the liquid from the tank by opening Eth_Drain_BV and Eth_Drain_NV	
30		Run the test sequence to evacuate all the final section of the line	
31		Open Eth_GasEvac_BV and then Eth_GasEvac_NV for venting the first part of the system	
32		Check that every part of the line is evacuated	

Figure 4.11: Checklist for the experiment conclusion

figure 4.12 is provided as an example, showing the properties evolution for the third test with a tank pressure of 6 bar and the first test with 14 bar.

After 5 seconds from the beginning of the sequence, the tank solenoid valve is opened for starting a 5 seconds pressurization additional procedure. Consequently, the tank pressure slightly rises (blu line), recovering from the pressure drops that might be occured in the previous test sequence. For the second graph, it can be noticed that the meseaured tank pressure is over 14 bar. The nitrogen pressure is set from the pressure regulator attached to the gas vessel, while the pressure inside the tank is visually monitored from the pressure gauge mounted on its top. However, as it was mentioned in section 4.2, the pressure value read from the pressure gauges may be affected by some errors and offset. Consequently, the pressure transducer's reading is the only reliable measurement to which be referred.

Subsequently, the water injection begins, as indicated by the increasing trend of the purple line. The mass flow rate reaches steady-state conditions after 3 to 4 seconds, confirming that the chosen injection durability for each sequence is enough for getting the desired results. During the injection of water, the tank slightly depressurizes.

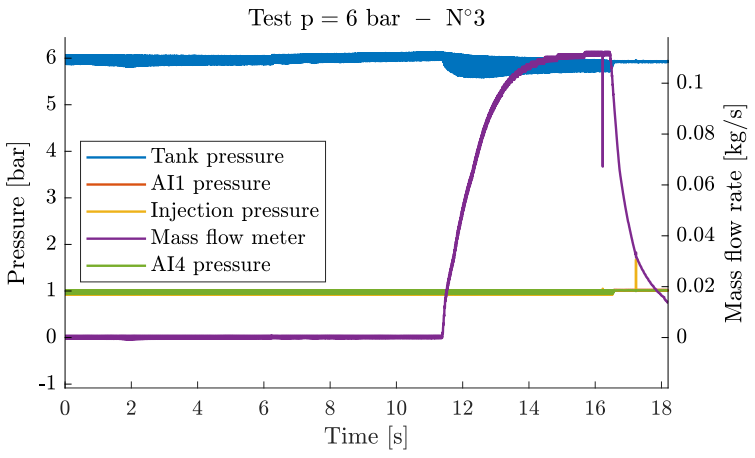

(a)

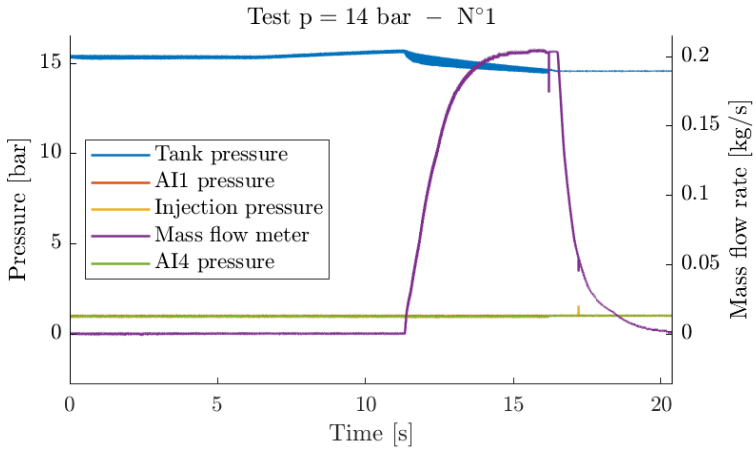

(b)

Figure 4.12: Global permeability test sequences

However, from the graphs, a problem involving the pressure measured upstream of the water injector emerges. In fact, the pressure value (yellow line) is completely overlapped by the atmospheric pressure measurement given by transducers related to the AI1 and AI4 channels (which, as mentioned, were not attached to the test bench). Consequently, this result leads to three possible conclusions: either a not properly functioning pressure transducer, an incorrect calibration procedure, or the investigated porous wall does not guarantee a sufficient pressure drop across its structure. In the last case, this would mean that, due to a too high permeability, water pressure decreases along the pipeline and reaches the cooling system inlet manifold at almost atmospheric pressure. Due to the uncertainty of these results, the mass flow rate measurements obtained from collecting all the injected water, weighting it and dividing the mass to the experiment duration time are not considered anymore, since they can not be related to a proper pressure difference.

On the other hand, the local permeability test results can still be considered since they are all run with the same tank pressure value and the objective is to compare the different location permeabilities. The tests results are hereby provided:

Tank pressure [bar]	Test	Local water mass [g]	Total water mass [g]	Mean total mass flow rate [g/s]	Mean local mass flow rate [g/s]	Local/Total mass flow rate ratio [%]
12	1	30.3	862.4	172.48	6.06	3.5
	2	41.8	838.8	167.76	8.36	4.9
	3	33.9	843.4	168.68	6.78	4.02

Table 4.1: Local permeability experimental results

After each test execution, the mean local mass flow rate value is computed by dividing the mass of local collected water by the experiment duration time. The water was locally collected from three distinct points arranged at a distance of 45-50° from each other (a representative scheme is provided in figure 4.14). Results show that the percentages of mass flow rate regarding these confined regions are fairly similar to one another, confirming a relatively uniform porosity of the porous structure.

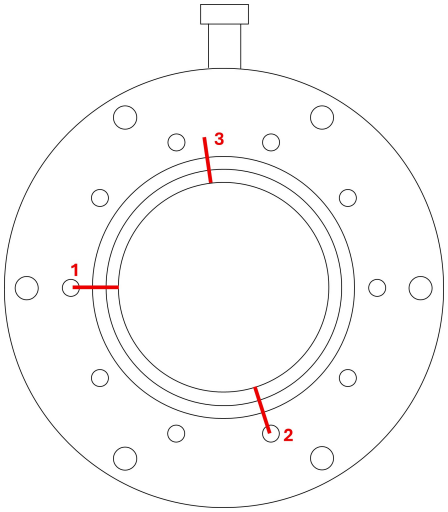

Figure 4.13: Locations of measured porous wall's local permeability

Figure 4.14: Execution of the local permeability water flow test

4.4 Second experiment execution and results

A second experiment execution is carried out with the objective of addressing the problems encountered during the first test run and therefore the correct system functionality. In this case, the cooling system assembly features the actual metallic housing. The test procedure is identical and follows the steps list given in the SOP document. However, due to time constraints, for this second execution fewer tank pressure values were investigated, but this nonetheless ensured a sufficient amount of useful data for the experimental campaign. Moreover, the pressure this time is measured in three different positions, namely inside the fuel tank, upstream to the pneumatic main valve and upstream to the water injector. The fourth voltage signal acquired is then provided by the Coriolis mass flow meter.

During the second experiment execution, with the metallic housing implemented into the system, the porous wall exhibited a clear uneven injection of water. The water momentum, indeed, is too high for allowing a proper distribution around the porous wall. An inevitable

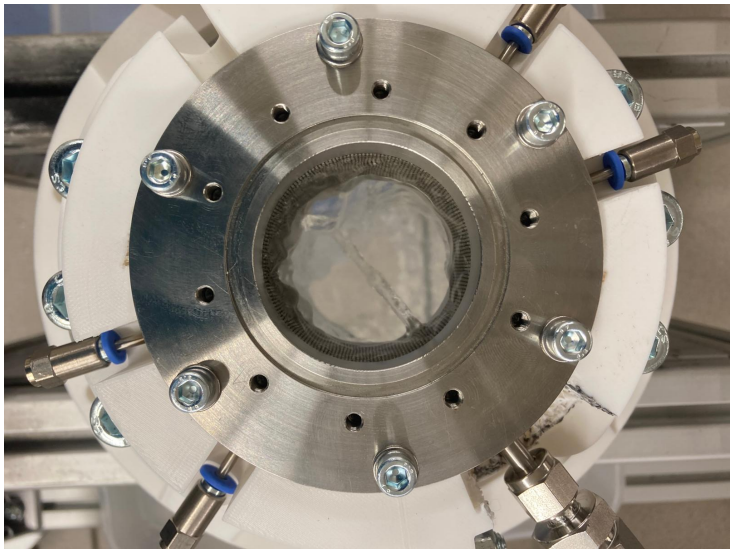

Figure 4.15: Water injection during a second execution sequence

conclusion would be that the employed porous structure does not guarantee a sufficient pressure drop that slows the coolant down and allows a more uniform injection. This effect, however, was not visible in the first experiment execution, probably because the plastic replacement provided a less tight sealing of the internal manifold and may have introduced slight pressure losses, leading to a more uniform distribution. Due to this undesired result, the experimental assessment of the porous wall local permeability was not carried out as it would inevitably provide not accurate or reliable results.

The sensors data are, thus, acquired by the DAQ system, processed on the LabVIEW program and corrected with the MATLAB script by considering the calibration procedure data. The obtained results may be represented on the graph, showing the properties evolution throughout the sequences (see figure 4.16).

The evolutions feature evident differences from the previous test case. The pressures measured upstream to the pneumatic main valve and to the water injector are clearly different from the atmospheric pressure, implying that the metallic housing offers a tighter sealing of the cool-

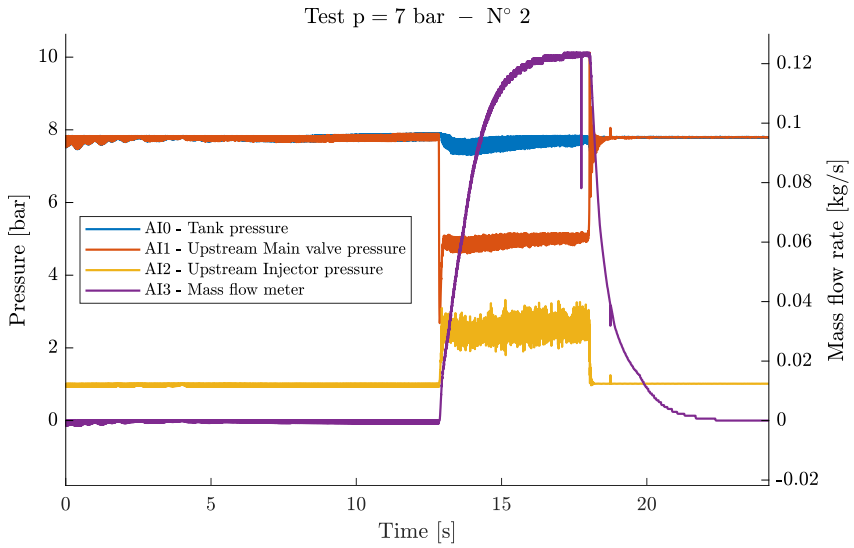

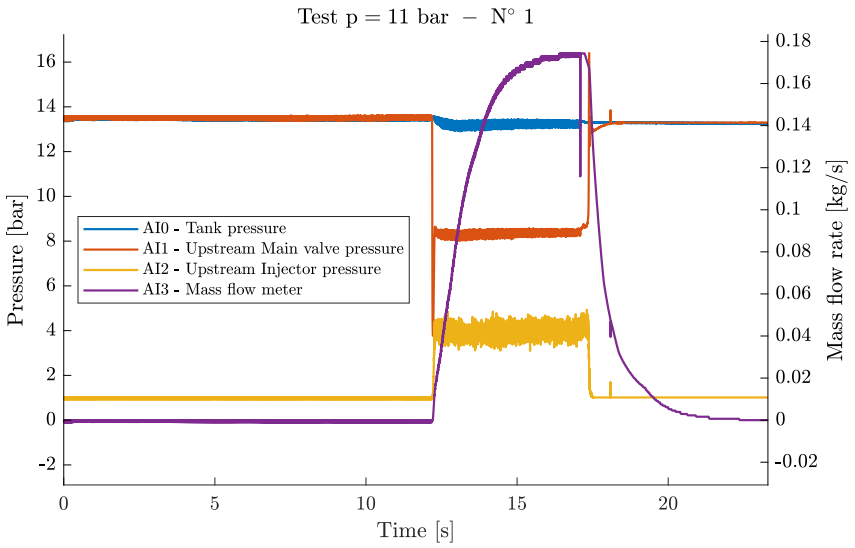

Figure 4.16: Global permeability test sequences

ing system therefore increasing the water pressure drop. The first pressure transducer measured a pressure drop occuring along the line between the fuel tank and the pneumatic main valve of approximately 2 bar for the first represented test and 4 bar for the second. This friction losses are plausible results if considering constant cross-section pipelines with mass flow rates of over 100 g/s. The same pressure drop occurs also between the main valve and the water injector.

Moreover, during the sequence, two additional effects can be visualized: first, the main valve opening causes the pressure inside the pipeline to suddenly decrease, as it is indicated by the clear pressure spike of the red line. Similarly, the valve closing induces the pressure increasing with a ”water-hammer” effect, which is effectively absorbed by the pneumatic accumulator installed along the fuel line.

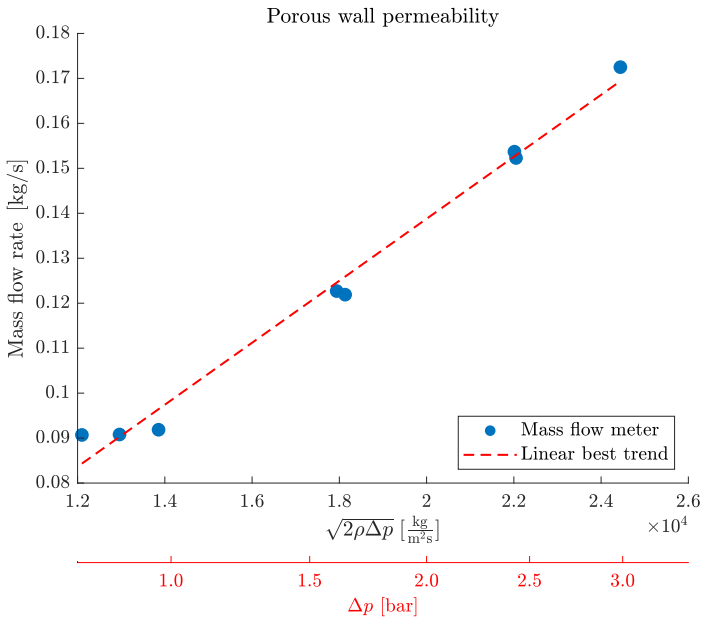

Figure 4.17: Porous wall experimental permeability

All mass flow rate results are subsequently represented on a graph as a function of the pressure difference across the sample. By considering the orifice equation, the dependence of the mass flow rate from the pressure difference is embedded in the term $\sqrt{2\rho\Delta p}$. Hence, data are represented on the graph as a function of the entire term, resulting in the arrangement of data on a linear trend (see figure 4.17). This outcome confirms the validity of the intended theory.

Chapter 5

Numerical simulation and modelling of the transpiration cooling

A fundamental step throughout the development of a new cooling technique for the combustion chamber of a rocket engine is the **numerical simulation and modelling** of the cooling approach through specific simulating and mathematical software tools, in order to obtain a preliminary result of its functionality, theoretical effectiveness and eventual related benefits. This simulation should implement validated models and established theories to provide reliable results of the study.

The objective of this chapter, hence, is to describe a MATLAB script developed for numerically simulating the transpiration cooling approach in a 500 N rocket engine combustion chamber. The model implements the NASA computer program **Chemical Equilibrium with Applications** (**CEA**) to evaluate the chemical reaction properties and thermodynamic constants and the **Allison's theory of hybrid combustion** to describe the various reactions occurring within the chamber's internal boundary layer. In addition, the intention of the study is to implement the permeability data acquired from the water flow test, so that the modelled wall would replicate the Laser Powder Bed Fusion (LPBF) manufactured component and eventually demonstrate the feasibility of this technique for the realization of fine porous structures for transpiration cooling applications.

However, the experimental results described in section 4.4 show a too high permeability for the investigated porous wall. To better comprehend this point, the specific impulse definition is considered:

$$I_{sp} = \frac{F}{g_0 \, \dot{m}} \tag{5.1}$$

where F is the engine's thrust (500 N), g_0 is the acceleration of gravity and $\dot{m}$ is the propellants total mass flow rate. For a rocket engine employing 70% in volume ethanol and 90% in weight hydrogen peroxide with a chamber pressure of 21.82 bar (later in this chapter it will be explained how the pressure value is obtained), the CEA code provides a specific impulse of 261 s, considering a stoichiometric mixture ratio (MR $= 4.9223$). In these conditions, the required propellants mass flow rates for obtaining 500 N of thrust can be computed as follows:

$$\dot{m} = \frac{F}{g_0 \, I_{sp}} = 0.1952 \; kg/s \tag{5.2}$$

$$\dot{m}_f = \frac{\dot{m}}{\text{MR}_{stoi} + 1} = 0.033 \; kg/s \qquad \dot{m}_{ox} = \dot{m} - \dot{m}_f = 0.1622 \; kg/s \tag{5.3}$$

The oxydizer is mostly injected at the starting end of the engine within the catalyst bed, while the remaining part is transpired through the wall, acting as coolant. The propellant total quantity, though, should match the required mass flow rate for the stoichiometric conditions inside the combustion chamber.

By assumption, if it is considered only 10% of the total hydrogen peroxide to be employed as coolant (this reference value was the amount of coolant required from the application of film cooling during previous research stages [47]), this would imply:

$$\dot{m}_{ox,cool} = 0.1 \cdot \dot{m}_{ox} = 0.0162\ kg/s$$

From the experiment results, such coolant mass flow rates would be accociated with very low differences between the coolant inlet pressure and the chamber pressure:

$$\dot{m}_{ox,cool} = 0.0162\ kg/s \quad \longrightarrow \quad \sqrt{2\rho\Delta p} = 2610\ \frac{kg}{m^2 s} \quad \longrightarrow \quad \Delta p = 0.0246\ bar \tag{5.4}$$

Based on its operating principle, the porous wall resembles a propellant "shower-head" injector. The injection system of a rocket engine is typically designed to feature a sufficiently high pressure difference across its small orifices, in order to face all pressure fluctuations that occur inside the combustion chamber (as reference, see figure 5.1). A reference value for this pressure drop could be 2÷3 bar. This means that the permeability results obtained from the experiment are completely incompatible with the engineering requirements for the engine's correct and safe operation. In conclusion, the **LPBF technique is not feasible for manufacturing porous structures for rocket engines transpiration cooling applications** because of the too high resulting permeability.

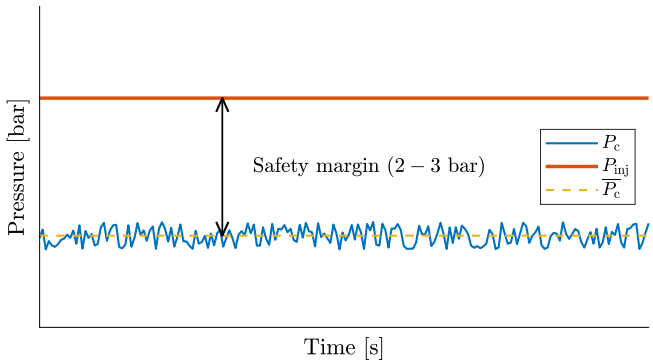

Figure 5.1: Safety margin between the chamber pressure and the injected propellant in a rocket engine

For the sake of this study, the permeability of the simulated porous structure is drastically reduced. In chapter 6 will then be proposed different ways for manufacturing less permeable walls. From preliminary analyses, it was estimated that a proper permeability value for this application could be only **1.3%** of the experimentally derived one. This value, as it will be demonstrated by the code's results, provides a sufficient amount of propellant for the engine cooling, resulting in convenient temperatures within the boundary layer, while maintaining a pressure drop across the wall of more than 2 bar.

The simulation of the transpiration cooling approach is therefore executed with a specifically developed MATLAB script, which implements the new permeability value for the simulated

porous wall. In this chapter, the modelling and simulation of the transpiration cooling functionality will be described, followed by the numerical study carried out. Particular attention will be devoted to the governing equations and theoretical models adopted to represent the underlying physical phenomena, which serve as the foundation of the analysis. Finally, the simulation's results will be presented.

5.1 Hybrid combustion physical model

As soon as hydrogen peroxide enters the combustion chamber, after transpiring through the porous wall, it undergoes a series of chemical and physical reactions due to the high temperatures and pressures encountered. These reactions include **vaporization**, **decomposition** and **combustion** with the fuel-rich freestream. Although in reality all these reactions occur simultaneously throughout the boundary layer near the wall, in this numerical study the system is simplified, following **Allison's hybrid combustion model** [20].

There are three types of a propellant droplet combustion: the **bipropellant combustion**, the **decomposition combustion** and the **hybrid combustion**. When a propellant liquid droplet is considered (for analogy to this study, an oxydizer droplet), the propellant vapours radially diffuse towards the environment. If the droplet is surrounded by a fuel-rich freestream, bipropellant combustion takes place at a specific temperature, referred to as bipropellant flame temperature. On the other hand, monopropellants in an inert environment can also self-sustain their decomposition thanks to the huge amount of thermal energy freed by the exothermic reaction, originating a decomposition combustion at a temperature depending on the propellant nature. Monopropellants like hydrogen peroxide, hydrazine and its derivatives show this particular behaviour.

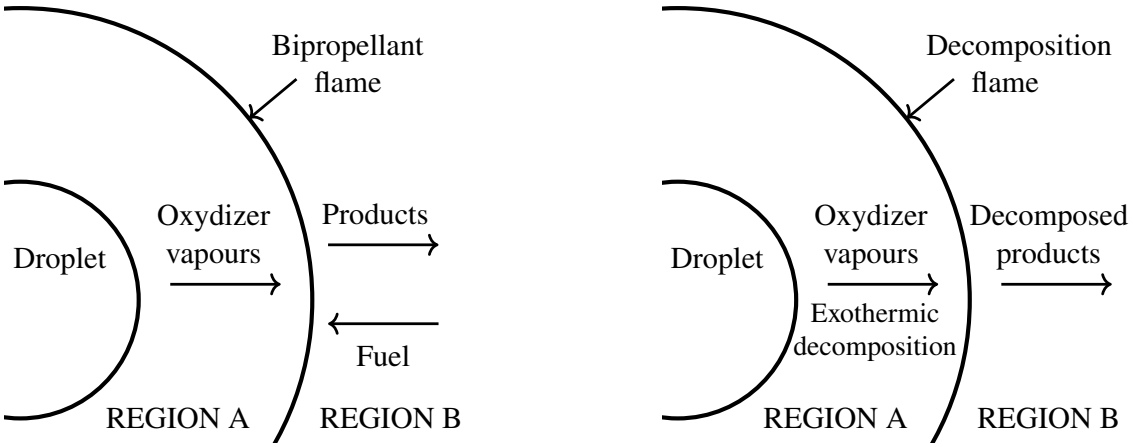

Figure 5.2: Diagrams showing the bipropellant (left) and decomposition (right) combustions of a propellant droplet

When the monopropellant (oxydizer) droplet is surrounded by a fuel-rich freestream, a hybrid combustion occurs. In this case, the oxydizer decomposition products then burn with the external fuel, hence two separated flames are observed, a monopropellant flame related to the decomposition reaction and a bipropellant flame on the outside. This phenomenon,

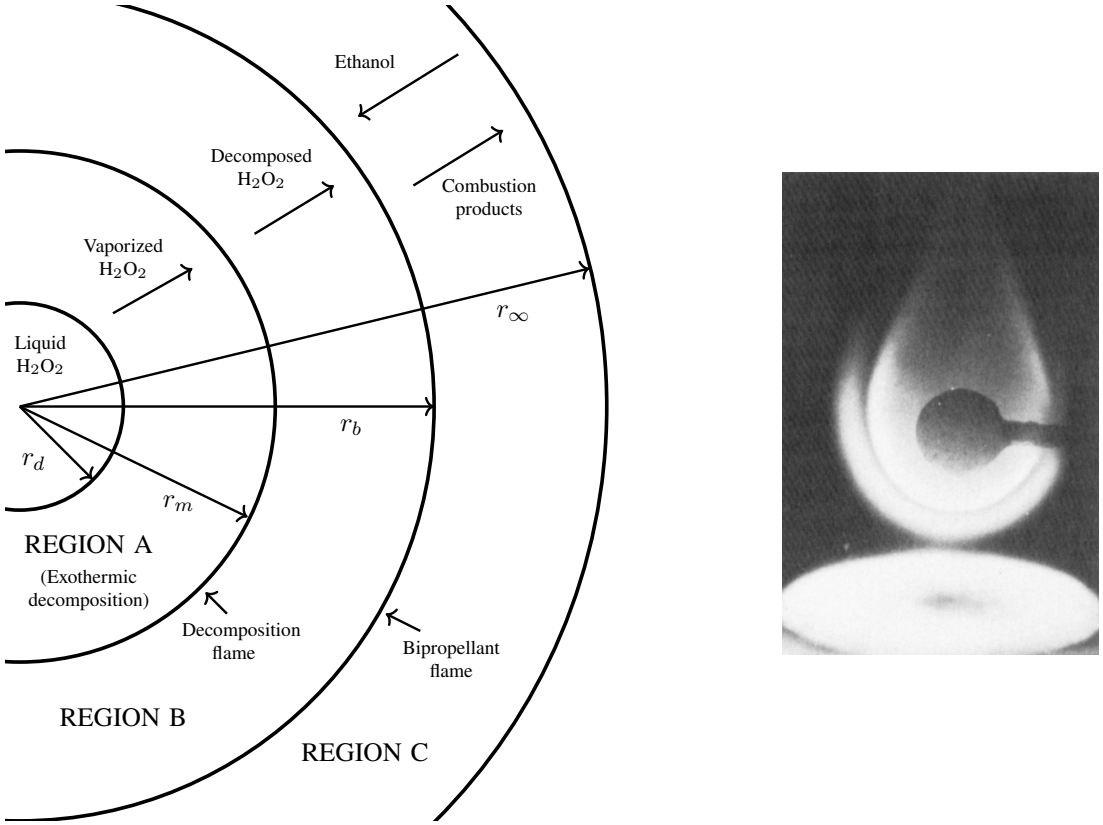

Figure 5.3: Left: diagram showing the implemented model of hybrid combustion for hydrogen peroxide and ethanol. Right: image showing hybrid combustion of hydrazine during an experiment from Allison's research [20]

observed in the past for many monopropellants, was investigated by Allison and Faeth [20], who where focused in particular on hydrazine (N_2H_4), monomethylhydrazine (MMH), unsymmetrical dimethylhydrazine (UDMH) and Aerozine 50 (wt 50% N_2H_4-UDMH) droplets combustion rates.

In order to assess the desired quantities, they suggested a simplified model of the hybrid combustion, whose results proved to be in good accordance with the data measured from experiments. The apparatus considered in their case involves a hydrazine droplet surrounded by oxydizing environment. According to Allison and Faeth's model, the monopropellant vaporizes between the liquid droplet and the monopropellant flame, at which propellant is considered to be fully decomposed. Subsequently, the monopropellant diffuses outward and reacts with the oxydizer at the bipropellant flame, from which the combustion products diffuse outward.

In figure 5.3 it is shown a diagram of the hybrid combustion model applied to the investigated case of this research with hydrogen peroxide and ethanol. Here, the propellant droplet is composed of high-test peroxide, which vaporizes and then diffuses towards the environment throughout Region A. The peroxide vapours (H_2O_2,H_2O), due to the high temperature, decompose forming a decomposition flame at the r_m position. The peroxide's decomposition products (H_2O, O_2) then diffuse outwards and mix with the fuel-rich freestream throughout Region B, originating a bipropellant flame at the r_∞ position. The combustion products, finally, diffuse into the external freestream throughout Region C.

Allison's model introduced several **assumptions** with the aim of simplifying the phenomena. The main ones are hereby listed:

- "The stagnant film approximation is used for estimating the effect of forced convective flow around the droplet. With this approximation, the gas phase system is spherically symmetric between the droplet surface and the edge of the stagnant layer r_∞";
- "the total gas pressure is constant throughout Regions A, B, and C";
- the ideal gas law holds for all species and, due to the high temperatures of the gas surrounding the droplet, compressibility effects can be neglected;
- thermal diffusion and radiation effects are neglected;
- "only steady state conditions are considered";
- "the monopropellant flame is assumed to be located at the radial position where the unreacted gas flows into the flame surface at the laminar burning velocity of the mixture (**Spalding's approximation**)";
- "the bipropellant reaction is confined to an infinitely thin surface where fuel decomposition products and oxidizer combine in stoichiometric proportion";
- all specific heats are assumed constant, meanwhile the thermal conductivity in Regions A, B, and C are assumed to be a linear function of temperature.

Using these assumptions and employing spherical simmetry (all properties only depend on the distance from droplet center r), the equations of conservation of mass, energy and species can be written in polar coordinates as:

$$\dot{M} = 4\pi r^2 \rho v = \text{constant} \qquad \text{(Mass)} \quad (5.5)$$

$$\frac{d}{dr}\left[\dot{m}\sum_{i=1}^{N} h_i \epsilon_i - \lambda r^2 \frac{dT}{dr}\right] = 0 \qquad \text{(Energy)} \quad (5.6)$$

$$r^2 \rho D \frac{dY_i}{dr} + \dot{m}(\epsilon_i - Y_i) = 0 \quad \text{con } \dot{m} = \frac{\dot{M}}{4\pi} \qquad \text{(Species)} \quad (5.7)$$

where ϵ_i is the mass flux fraction of the species i, computed as:

$$\rho v \epsilon_i = \rho Y_i \left(v + U_i\right) \quad (5.8)$$

In the equations above, ρ is the propellant density, v is the mass average velocity, $\dot{M}$ the total mass flow rate and $\dot{m}$ the mass flow rate per unit solid angle, N the total number of species, h_i, U_i and Y_i are respectively the enthalpy, the diffusion velocity and the mass fraction of the species i, λ is the propellants thermal conductivity and D the binary diffusion coefficient.

Applying the assumptions above, the Allison's model considers a set of five equations: the energy equation distinctly applied at Region A, B and C, the species equation applied to the oxydizer at Region C and the mass equation, employing a laminar flame velocity expression (**Arrhenius equation**). These equation have a total of five unknown properties, namely the mass flow rate per unit solid angle, the monopropellant flame temperature , the radius of monopropellant flame, the bipropellant flame temperature and the radius of bipropellant flame.

In conclusion, the Allison's model aims to calculate the mass burning rate of a propellant droplet as a function of the droplet's diameter. Hence, the model has to be modified in order to be employed for the hybrid combustion of a transpiring propellant. In particular, more assumptions are considered for changing coordinates system from polar to one-dimensional. Moreover, the distribution of coolant is assumed even across the inner surface of the chamber's wall. With these assumptions, the Allison's model equations can be written as:

$$\dot{M} = \rho v S = \text{constant} \qquad \text{(Mass)} \quad (5.9)$$

$$\frac{d}{dy}\left[\dot{m}\sum_{i=1}^{N} h_i \epsilon_i - \lambda S \frac{dT}{dy}\right] = 0 \qquad \text{(Energy)} \quad (5.10)$$

$$S\rho D\frac{dY_i}{dy} + \dot{m}(\epsilon_i - Y_i) = 0 \quad \text{con } \dot{m} = \frac{\dot{M}}{4\pi} \qquad \text{(Species)} \quad (5.11)$$

5.2 Description of the simulating MATLAB code

The Allison's model of hybrid combustion is simplified and implemented on a MATLAB script for simulating the functionality of transpiration cooling for the combustion chamber of a rocket engine. This numerical study aims to compute the **temperature** and **heat flux profiles** across the chamber's wall boundary layer, the required coolant mass flow rate and, therefore, assess the cooling approach feasibility. The analysis has two main **constraints** regarding the coolant temperature: the coolant must remain in the liquid state until entering the combustion chamber, otherwise, system detonation becomes inevitable. Moreover, the coolant temperature should remain uniform at all points of the coolant inlet manifold and on the coolant-side of the porous wall. If not, this would indicate that an external heat flux is affecting the coolant and continuous heat exchange could ultimately lead to the system failure.

The system's one-dimensional model is hereby represented:

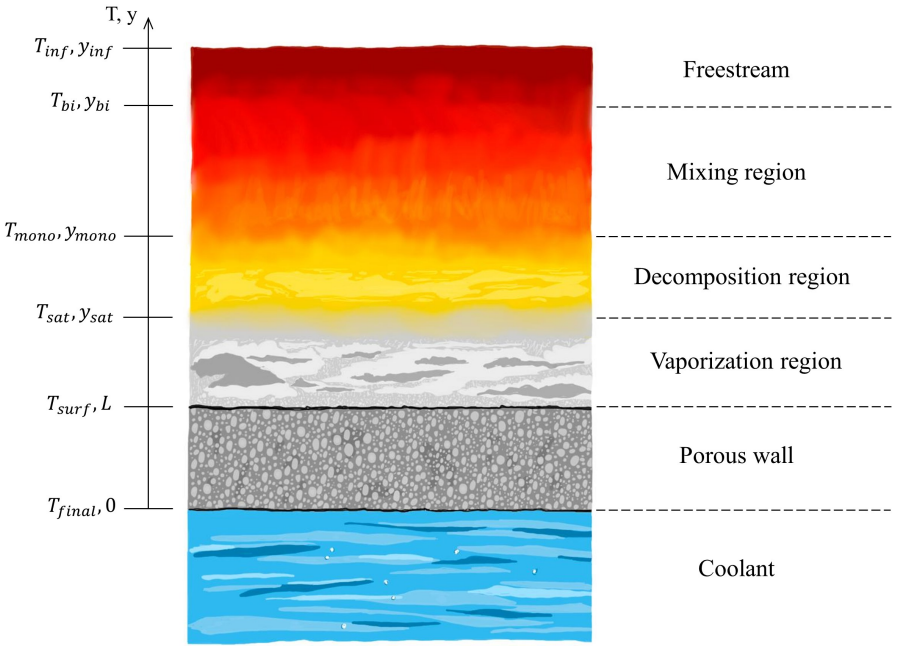

Figure 5.4: Representation of the modelled system

The system is divided into sub-layers, assuming a sequence of distinct reactions, each one confined to a different sub-layer, in accordance to the model. The liquid coolant first vaporizes due to the high temperature (**vaporization region**). Subsequently, heat also induces spontaneous decomposition of the peroxide (**decomposition region**). Finally, the reaction products mix with the fuel-rich freestream and combustion takes place (**mixing region**). Among the cited reactions, decomposition and combustion are **exothermic** processes, which increase the boundary layer temperature up to the freestream value, while vaporization is an **endothermic** mechanism that removes heat from the system and effectively cools the chamber wall. Considering a one-dimensional coordinates system, the flow properties are assessed perpendicularly to the wall across the boundary layer.

All energy contributions, both released and absorbed, related to the distinct sub-layers reactions are assumed to be introduced into the system only at the **interfaces**. Specifically, all vaporization is assumed to occur at a certain position denoted as y_{sat}, all decomposition at y_{mono} at the adiabatic decomposition temperature and all combustion at y_{bi} at the adiabatic combustion temperature. As a result, the **heat exchange discretely changes** when moving from one region to next.

Two additional assumptions regarding the boundary layer concern the heat exchange experienced by the coolant. Since throughout the whole system the velocity normal to the wall is very low and the fluid can be assumed to be static, only **conduction** is considered. This assumption, however, does not hold for the last interface, where the fluid is exposed to the high-momentum freestream. In this case, **convection** becomes the dominant mechanism. Moreover, in accordance with Allison's model first assumption, the **film theory** for heat transfer between a solid wall and a moving fluid can be applied. The theory will be further explored later.

The fixed parameters and design data for the analysis are listed in the following table:

Engine's known data	
Required thrust	500 N
Propellants	70% solution ethanol 90% wt hydrogen peroxide
Combustion conditions	Stoichiometric
Engine's throat cross section area	$1.41 \cdot 10^{-4}$ m^2
Coolant temperature	300 K
Assumed monopropellant flame temperature	800 K

Porous wall material's properties (SS 316)	
Thermal conductivity	20 W/(m·K)
Yield strength	205 MPa

Table 5.1: Analysis reference data

Among the presented data, two of them require further elaboration. First, the engine's nozzle geometry is determined by the original configuration, deriving from the HTP/Kerosene rocket engine. As explained in chapter 2, the investigated rocket engine employs an already existing configuration in which the new transpiration cooling concept has been implemented, therefore the engine's geometry is known already. Secondly, the monopropellant flame temperature, which was one of the five unknown parameters of Allison's model, in this case is assumed known and

equal to 800 K. Even though the 90% hydrogen peroxide adiabatic decomposition temperature given by the CEA program is 1050 K, this reference value was computed in a previous research concerning film cooling with hydrogen peroxide [47], by solving the Arrhenius equation:

$$\dot{m}_{dp} = A\, e^{-\frac{E}{RT}} \cdot C_{HP} \tag{5.12}$$

where $\dot{m}_{dp}$ is the mass flow rate of the decomposition products, A is the pre-exponential reaction rate constant, E is the activation energy, R is the universal gas constant, T is the temperature and C_{HP} is the mass concentration of hydrogen peroxide. If one assumes that all decomposition occurs at the y_{mono} interface and there is no mass accumulation there, the coolant mass flow into the interface must equal the mass flow rate of the decomposition products. Thus an assumed value of 800 K corresponded to the temperature at which the Arrhenius decomposition rate matched the incoming coolant mass flow rate.

The first step of the code is the computation of the **combustion chamber pressure** p_{cc}. Its value depends on the engine's geometry and mass flow rate, in order to obtain the required thrust. The sequence of steps is represented with the following blocks diagram:

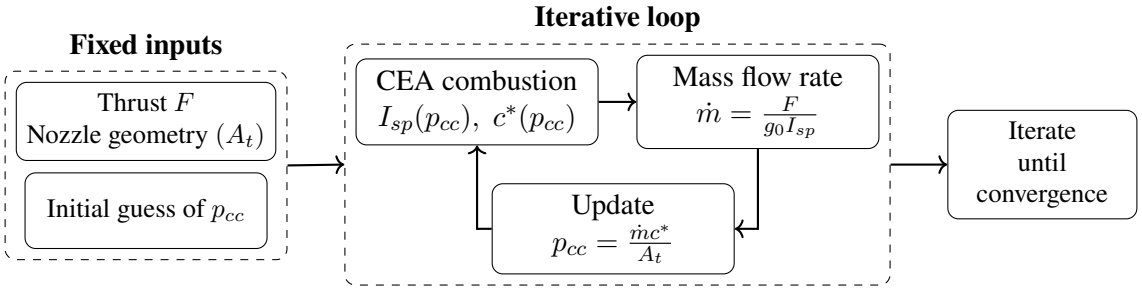

Figure 5.5: Combustion chamber pressure iterative calculation

Given the engine's thrust and geometry, assumed a chamber pressure first guess, the specific impulse I_{sp} and characteristic velocity c^* are obtained from the CEA code. Then, the required total mass flow rate of the engine is computed from the definition of specific impulse. The mass flow rate is subsequently used for updating the pressure value, implementing the characteristic velocity definition formula. Once the pressure is updated, the loop is repeated until convergence. The resulting chamber pressure value is:

$$p_{cc} = 21.82 \text{ bar}$$

Once the engine's chamber pressure is known, using the CEA program, it is possible to obtain the **thermodynamic properties for the propellants adiabatic combustion**, namely the adiabatic combustion temperature T_{cc}, the mean molar mass of the combustion products MW_{mean}, their thermal conductivity k, the Prandtl number Pr and the specific heat at constant pressure c_p. CEA results are listed in Table 5.2. Additionally, the CEA code provides performance parameters of the propulsion system, namely the specific impulse and the characteristic velocity. Among these, one essential output is the **stoichiometric mixture ratio** (MR). Knowing the thrust and the specific impulse, the propellants mass flow rates can be computed (see equations 5.2 and 5.3):

$$\dot{m} = 0.2019 \text{ kg/s} \qquad \dot{m}_f = 0.0341 \text{ kg/s} \qquad \dot{m}_{ox} = 0.1678 \text{ kg/s}$$

T_{cc}	γ	MW$_{mean}$	Pr	c_p	k
2627 K	1.133	21.76 g/mol	0.673	4309 J/(kg·K)	0.612

MR	I_{sp}	c^*
4.992	261 s	1576 m/s

Table 5.2: CEA combustion results

The oxidizer mass flow rate is partially injected at the inlet of the engine into the catalyst bed, while the remaining fraction (G or **porous wall mass flux**) is injected as coolant through the cooling system. This amount is still unknown at this point of the numerical study, since there is still no information regarding the cooling approach feasibility and the required amount of coolant. The porous wall mass flow rate is therefore obtained by multiple executions of the MATLAB script, modifying it until the target results of wall temperature are reached.

The cooling approach is analysed by discretising the chamber's axial length into a finite number of segments. Specifically, 21 axial sample points are selected along the chamber, defining 20 equally sized segments. The numerical model then performs a local analysis of the combustion chamber within each individual segment. For each segment, the flow properties within the boundary layer and the porous-wall mass flux G are locally evaluated. The local injected coolant mass flow rate is subsequently obtained by multiplying the mass flux by the lateral surface area of the cylindrical wall corresponding to the considered segment.

This procedure is repeated sequentially for all segments along the chamber axis, ultimately providing the total oxidizer mass flow rate required to achieve stoichiometric combustion. Since the total amount of oxydizer is fixed, as the G value is regulated throughout the various code executions, the initial oxydizer mass flow rate must be accordingly adjusted.

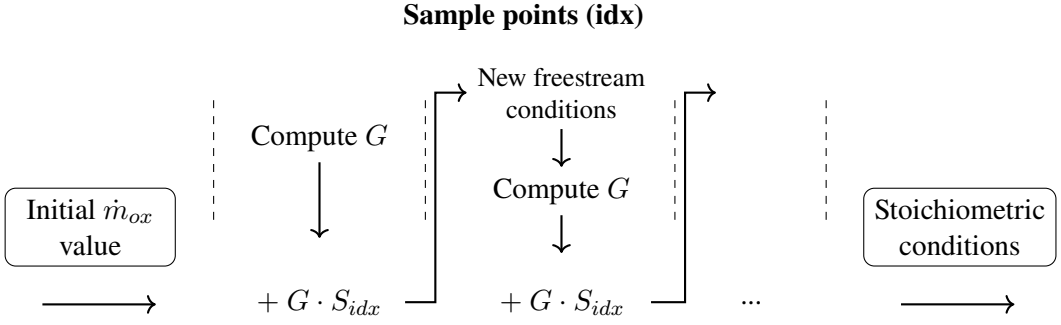

Figure 5.6: Oxydizer mass flow rate injection diagram

After fixing the initial value of the oxidizer mass flow rate injected upstream of the engine, the code proceeds with the analysis of the discretised combustion chamber, one segment at time. Each segment is treated sequentially and analysed independently under locally defined flow conditions. For each cylindrical surface, first the code computes the freestream properties, namely local mixture ratio, gas chemical properties (i.e. specific heat ratio, thermal conductivity, specific heat at constant pressure and Prandtl number), Mach number, static temperature and static pressure, density, speed of sound and flow velocity.

Once the freestream conditions are established, the effective thermal conductivity of the

porous wall is evaluated, by accounting for the combined contribution of the fluid occupying the pores and the solid matrix of the structure. The adopted model expresses the effective conductivity k_{eff} as a function of the fluid thermal conductivity k_f, the porosity of the material ϵ and the conductivity ratio between the fluid and the solid phase σ:

$$k_{\text{eff}} = k_f \left[\left(1 - \sqrt{1-\epsilon}\right) + \frac{2\sqrt{1-\epsilon}}{1-\sigma B} \left(\frac{(1-\sigma)B}{(1-\sigma B)^2} \ln\left(\frac{1}{\sigma B}\right) - \frac{B+1}{2} - \frac{B-1}{1-\sigma B} \right) \right]$$

$$\text{where} \quad B = 1.25 \left(\frac{1-\epsilon}{\epsilon}\right)^{10/9} \tag{5.13}$$

The parameter B is an empirical coefficient that accounts for the geometric characteristics of the porous medium. The effective thermal conductivity is evaluated locally for each cylindrical surface, given the temperature-dependence of the coolant thermal conductivity.

Once these quantities are assessed, the code proceeds with its core section, devoted to the analysis of the various regions and to the determination of the temperature and heat flux profiles

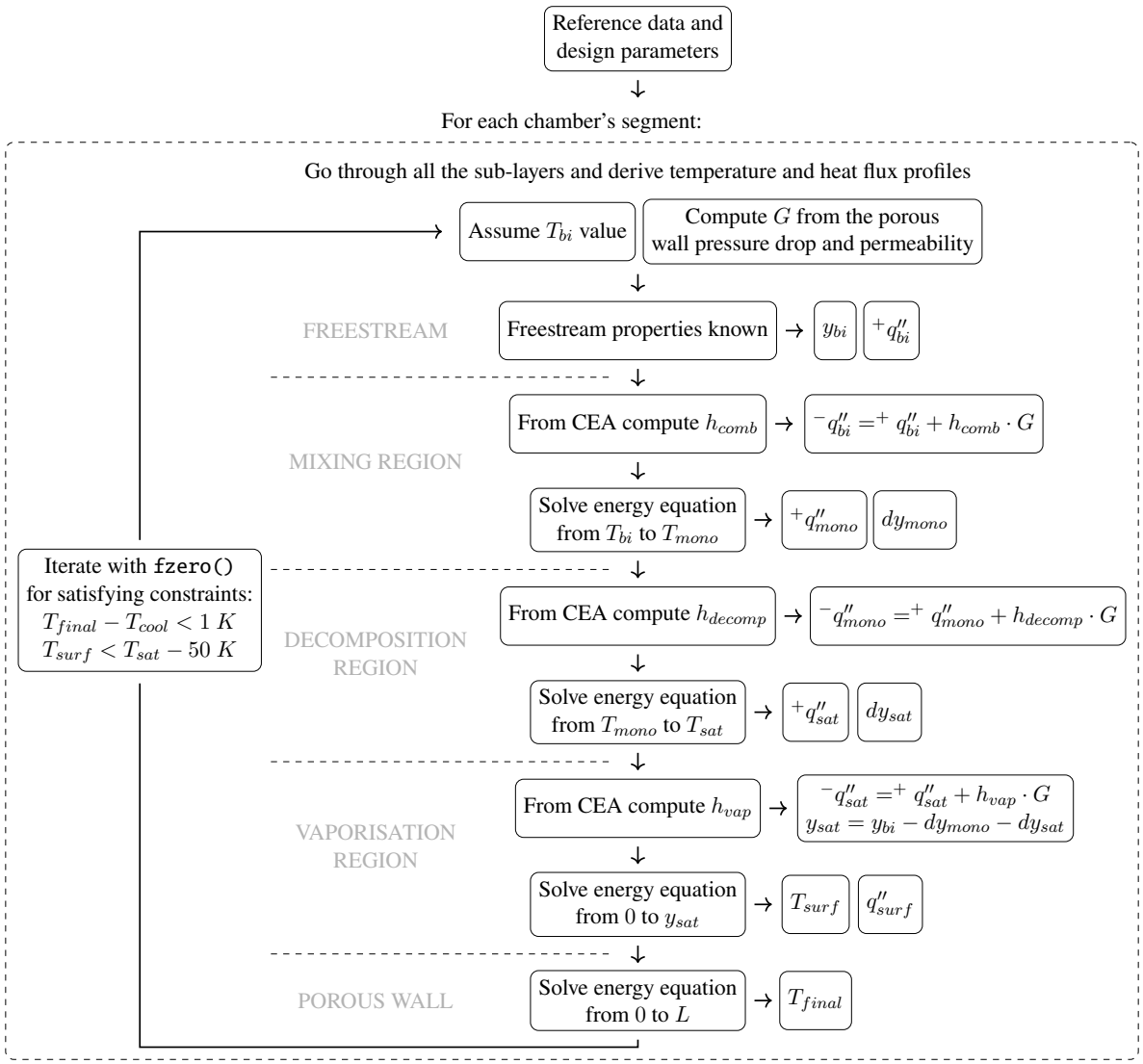

Figure 5.7: Explanatory blocks diagram of the core section of the code

across them. Among the five unknown variables of Allison's model, at this point of the numerical study, only the monopropellant flame temperature T_{mono} is known and assumed equal to 800 K. Since the present work is intended as a preliminary and simplified feasibility study of the cooling approach, several assumptions are introduced to reduce the complexity of the solution procedure.

The bipropellant flame temperature T_{bi} is therefore selected as the **single design parameter** of the analysis. Its value is determined through an iterative procedure based on the MATLAB function `fzero()`, which repeatedly executes the model until a prescribed objective function is driven to zero. As it was mentioned at the beginning of this section, two physical requirements concerning the temperature profile should be satisfied simultaneously:

1. the coolant must remain in the liquid state until entering the combustion chamber to avoid possible detonation;

2. the coolant temperature should remain uniform at all points of the inlet manifold and on the coolant-side of the porous wall.

The first statement is enforced by ensuring that the coolant temperature remains below a 50 K safety margin from the peroxide's saturation temperature, meanwhile the second one imposes that the temperature of the coolant-side of the porous wall is 300 K.

However, since a single design parameter cannot satisfy two independent constraints, only objective 2 is enforced in the procedure. The remaining requirement is afterwards verified, under the assumption that it is reasonably met by the final solution obtained for the bipropellant flame temperature. Once the T_{bi} value is assigned, the three remaining model's unknown quantities are computed through the core section of the code, which is hereby presented.

Freestream

The boundary layer's analysis begins by assessing the heat flux between the mixing region and the freestream (referred to as ${}^{+}q''_{bi}$), using the formula:

$$ {}^{+}q''_{bi} = h_{conv,\infty}(T_{cc} - T_{bi}) \tag{5.14} $$

The hot-flow convective heat transfer coefficient $h_{conv,\infty}$ is computed with a semi-empirical correlation based on the **Dittus-Boelter formula** from the **classical turbulent heat transfer theory**:

$$ h_{conv,\infty} = 0.023 \cdot \frac{(\rho v^{0.8})}{D_h^{0.2}} \cdot \frac{\mathrm{Pr}_\infty^{0.4} \cdot k_\infty}{\eta_\infty^{0.8}} \qquad \text{with} \quad \eta = \frac{\mathrm{Pr} \cdot k}{c_p} \tag{5.15} $$

where ρ and v are the local density and velocity of the freestream gas, while D_h is the chamber's hydraulic diameter (corresponding to the nominal diameter for cylindrical shapes).

Consequently, the whole boundary layer thickness y_{bi} can be computed by using the **film theory**. According to the theory, a quasi-static fluid touching a wall can be assumed as a so called **film**, in which all heat exchanges occurs through conduction. This assumption stands for the lower layers, but is not applicable to the upper interface, where the coolant interacts with the high momentum freestream and convection is the dominant effect. Therefore, the thermal conductivity and the convective heat transfer coefficient can be related for assessing the y_{bi} distance:

$$ y_{bi} = \frac{k}{h_{conv,\infty}} \tag{5.16} $$

Mixing region

From the upper interface, the process starts analysing every sub-layer in succession. The first region encountered is the mixing region. As previously mentioned, the combustion process occurs throughout the whole mixing sub-layer, although the enthalpy produced by the reaction is assumed to be provided only at the upper interface (y_{bi}).

In order to compute the combustion enthalpy and the consequent heat drop across the interface, the **coolant mass flux** G is evaluated. Its value is obtained by considering 1.3% of the experimental permeability results for the porous wall, shown in figure 4.17, and the pressure drop occurring across the wall.

Hence, the flow's enthalpy can be assessed. The enthalpy released by the adiabatic combustion can be quantified as the difference between the combustion products enthalpy at the adiabatic combustion temperature and the enthalpy of the propellants subjected to subsequent combustion (h_{prod}):

$$h_{comb} = \left[h_{LHP,300} \cdot 0.90 + h_{LW,300} \cdot 0.10 + \frac{h_{f,eth}}{\text{MR}} \right] - h_{prod} \cdot \left(1 + \frac{1}{\text{MR}} \right) \tag{5.17}$$

where $h_{LHP,300}$ is the liquid hydrogen peroxide enthalpy at 300 K, $h_{LW,300}$ is the liquid water enthalpy at 300 K and $h_{f,eth}$ is the enthalpy of formation of ethanol. These enthalpies were obtained by using NASA coefficients for calculating thermodynamic and transport properties.
From the upper layer, the heat flux rises discretely of a quantity equal to the enthalpy of combustion h_{comb}. The resulting value of the heat flux is:

$$^{-}q''_{bi} = {}^{+}q''_{bi} + h_{comb} \cdot G \tag{5.18}$$

The last feature to assess for the mixing region is the layer thickness dy_{mono}. Since the lower interface temperature T_{mono} is already known, the code evaluates the layer thickness by computing the conductive heat flux and integrating the **energy equation**:

$$\frac{dT}{dy} = -\frac{q}{k} \qquad\qquad \frac{dq}{dy} = G\, c_p\, \frac{dT}{dy} \tag{5.19}$$

The integration permits to obtain also the heat flux value at the lower interface, $^{+}q''_{mono}$.

Decomposition region

Next sub-layer is the decomposition region, for which the energy produced by the chemical reaction is assumed to be released at the y_{mono} interface. The decomposition enthalpy for 90% hydrogen peroxide is obtained from the CEA code. The heat flux value on the other side of the interface $^{-}q''_{mono}$ is:

$$^{-}q''_{mono} = {}^{+}q''_{mono} + h_{decomp} \cdot G \tag{5.20}$$

Similarly to what has been done for the mixing region, the sub-layer thickness dy_{sat} can be assessed by integrating equation 5.19 until the flow temperature is equal to the vaporization temperature T_{sat} (the saturation temperature for 90% wt hydrogen peroxide given by the CEA code related to a pressure of 21.82 bar is 390 K). As before, the integration provides the heat flux value at the lower interface $^{+}q''_{sat}$.

Vaporization region

While the combustion and the decomposition are exothermic processes which release energy to the system, vaporization is endothermic and subtracts energy from it. The enthalpy required from the system to vaporize a 90% hydrogen peroxide solution is computed as the difference between the enthalpy of the liquid substance and the gaseous one at the saturation temperature. As before, the heat flux at the lower side of the interface ${}^{-}q''_{sat}$ is:

$$ {}^{-}q''_{sat} = {}^{+}q''_{sat} - h_{vap} \cdot G \tag{5.21} $$

For the last sub-layer the thickness is already known, since it can be derived from the total boundary layer thickness y_{bi} and the previous sub-layers ones. However, in this case the final temperature for the integration is not known. As a consequence, equation 5.19 is integrated from 0 to y_{sat} and the surface temperature T_{surf} and heat flux q''_{surf} values are obtained.

Porous medium

Finally, the code evaluates the flow passage across the porous medium. In this case, the thickness of the sub-layer is known and the goal is to compute the temperature of the coolant-side of the wall T_{final}. To assess it, equation 5.19 is integrated from 0 to the wall thickness L.

The same procedure is repeated for each chamber segment individually, determing the correct T_{bi} value that satisfies the main selected constraint:

$$ T_{final} - T_{sat} < 1 \ K $$

Meanwhile, the second constraint is subsequently verified by adjusting the porous wall mass flux value. Code executions confirmed that a proper G value for satisfying both coolant temperature constraints is about $0.6 \div 0.7$ kg/(m^{2}s).

5.3 Simulation results

By performing multiple executions of the numerical model, it was found that a theoretical implementation of the proposed transpiration cooling system would require approximately **2% of the total hydrogen peroxide mass flow rate**. The employed coolant fraction is sufficient to ensure both an adequate pressure drop across the porous wall and an effective thermal protection of the combustion chamber. This result is particularly promising when compared to a conventional film cooling approach, for which a coolant mass flow rate of about 10% was required under similar operating conditions. The significantly reduced coolant demand highlights the potential advantages of transpiration cooling in terms of thermal efficiency and propellant utilization, even within the simplified framework adopted in the present study.

The numerical simulation results are hereby presented. In particular, figures 5.8 and 5.9 show the temperature and heat flux profiles across the porous wall thickness and the chamber's boundary layer, taken at a position of $x/l_{\text{chamber}} = 0.5$.

The temperature profile, assumed to vary linearly across the different regions of the boundary layer, exhibits a monotonically decreasing trend from the freestream towards the wall surface, as physically expected. The temperature values evaluated at each interface confirm that the two main thermal constraints imposed in the model are effectively satisfied. In particular, the

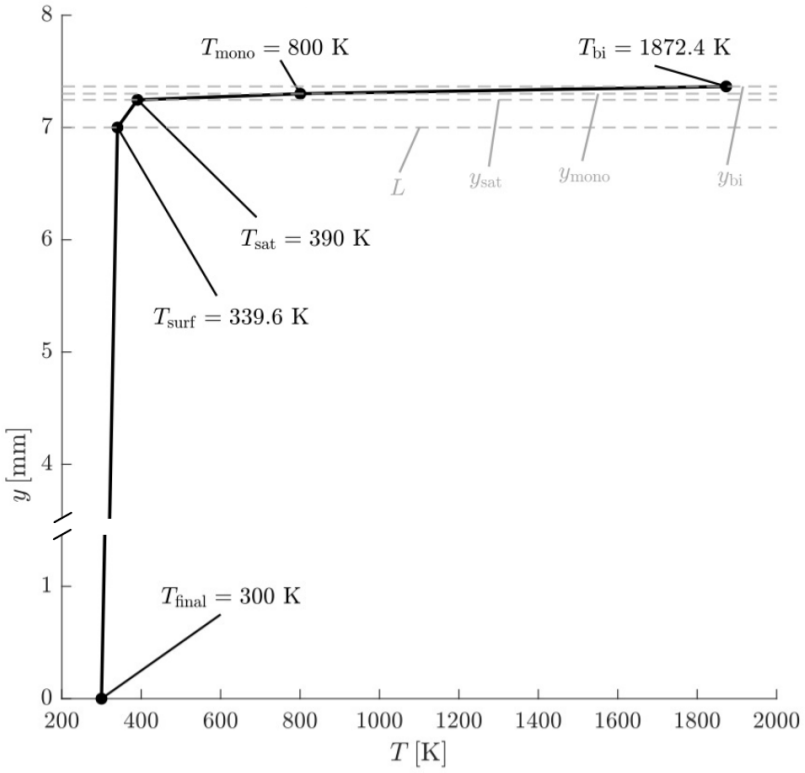

Figure 5.8: Temperature profile

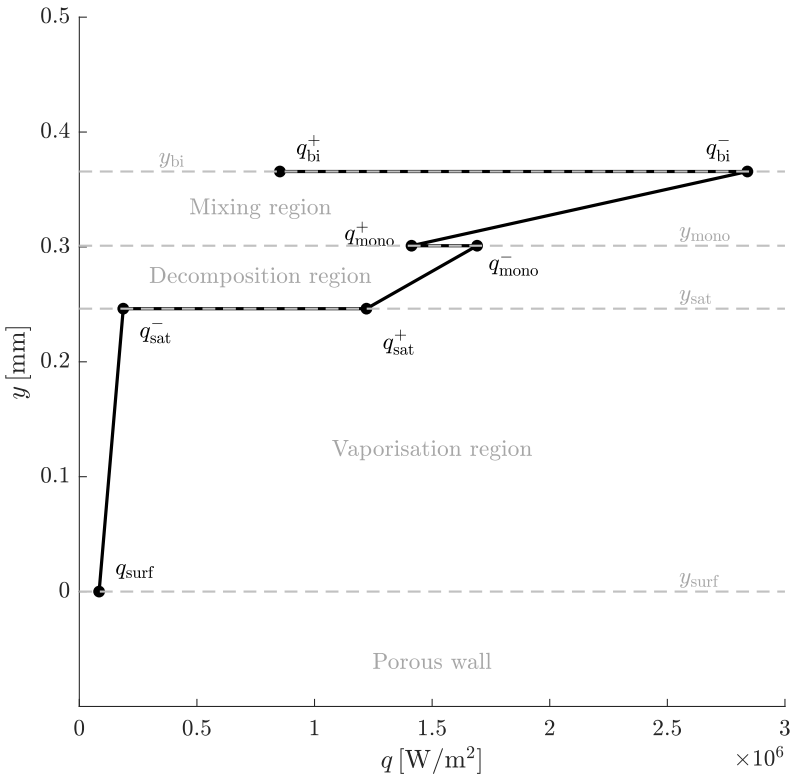

Figure 5.9: Heat flux profile

temperature on the coolant side of the porous wall is fixed at 300 K by construction through the `fzero()` function, while the final coolant temperature T_{final} remains more than 50 K below the hydrogen peroxide saturation temperature. This condition provides a sufficient safety margin to prevent premature boiling and reduces the risk of detonation phenomena within the cooling system.

Starting from the cold side, the incoming liquid coolant maintains a constant temperature of 300 K throughout the inlet manifold and up to the lower surface of the porous wall. This indicates that no heat flux is transferred to the coolant within the feeding system, consistently with the assumption of an adiabatic inlet manifold. Within the porous wall, the temperature increases to 339.6 K as a result of heat conduction through the metallic structure. Moving further outward, the temperature rises rapidly across the thin sub-layers characterised by decomposition and combustion of propellants. The boiling temperature of 390 K is reached at the y_{sat} interface, where all the coolant vaporization is assumed to take place. Continuing across the boundary layer, the temperature reaches the monopropellant flame temperature of 800 K at the y_{mono} interface, corresponding to the location where hydrogen peroxide decomposition is assumed to be complete. Finally, the temperature reaches a value of 1872.4 K at the y_{bi} interface, which represents the bipropellant flame region. Overall, the resulting temperature distribution is physically consistent and reflects the progressive transition from the cold coolant flow to the high-temperature reacting flow in the combustion chamber.

The heat flux profile, on the other hand, exhibits a discontinuous trend, characterized by discrete jumps at the interfaces between the different regions. This behaviour derives directly from one of the main assumptions of the model, according to which the heats of reaction are released only at specific locations within the boundary layer. In particular, both the monopropellant decomposition and the bipropellant combustion processes are exothermic and therefore introduce energy into the system, whereas the vaporization of the coolant is an endothermic process and locally subtracts energy from it. As a consequence, when following a fluid particle moving from the core of the combustion chamber towards the porous wall, the heat flux increases across the combustion and decomposition flame interfaces, while it experiences a sudden decrease at the vaporization interface.

Within each individual region, the heat flux exhibits a monotonically decreasing trend. This feature is associated with the presence of a moving fluid that progressively changes its temperature and internal energy while flowing through the different sub-layers. As dictated by the energy conservation equation, these variations directly affect the local heat flux. Due to the lack of detailed information on the spatial distribution of energy exchange within each region, the heat flux is assumed to vary linearly between adjacent interfaces. The present analysis, in fact, is inadequate for the assessment of the precise trend of the heat flux across the boundary layer.

x/l_{chamber}	0	0.25	0.5	0.75	1
$G\,[\text{kg}/(\text{m}^2\,\text{s})]$	0.6978	0.6978	0.6979	0.6979	0.6979
$T_{bi}\,[\text{K}]$	1871.6	1872	1872.4	1872.8	1873.1
$T_{surf}\,[\text{K}]$	339.3	339.4	339.6	339.8	340
$y_{bi}\,[\text{mm}]$	0.368	0.367	0.366	0.364	0.363
$y_{mono}\,[\text{mm}]$	0.303	0.302	0.301	0.299	0.298
$y_{sat}\,[\text{mm}]$	0.248	0.247	0.246	0.245	0.244

Table 5.3: Simulation results in different positions of the chamber

The relatively small amount of coolant injected through the porous wall is not sufficient to significantly affect the main flow freestream conditions in the core of the combustion chamber. Consequently, the results show a nearly uniform distribution of the mass flux G, the interface locations and the flame temperatures across the different sample points. This behavior indicates that the transpiration cooling system primarily affects the near-wall region, while leaving the freestream flow largely undisturbed.

Moreover, the analysis of the temperature and heat flux profiles shows that the flame locations remain very close to the wall. This outcome represents a particularly favorable result, as it suggests that the proposed cooling approach could also be applied to engine components characterized by more complex geometries, such as aerospike rocket nozzles. In such configurations, the presence of an excessively thick boundary layer could otherwise obstruct the flow passage, especially in critical regions like the nozzle throat.

Chapter 6

Conclusions and possible future research stages

The present research thesis investigated the feasibility of applying the **transpiration cooling** technique to the combustion chamber of a rocket engine using **high-test hydrogen peroxide** as coolant. In particular, the work focused on assessing the potential of additively manufactured porous components for this application, with specific attention devoted to the **Laser Powder Bed Fusion** (**LPBF**) manufacturing process. The study was aimed to establish an integrated framework combining design, manufacturing, experimental characterisation and numerical modeling in order to evaluate both the technological and physical viability of the proposed cooling approach.

At this scope, a dedicated transpiration cooling system was designed and integrated into a representative rocket engine configuration operating with 90% in weight hydrogen peroxide as oxidizer and coolant, and 70% in volume ethanol as fuel. The cooling system assembly consists of three main components, two of which were manufactured in-house at the TU Dresden workshop laboratory, while the porous wall was commissioned to the TU Dresden partner Fraunhofer IWS and produced via the LPBF technique.

Subsequently, the porous component was experimentally characterised through a cold-flow water test aimed at determining its **permeability**. The experiment was conducted on a test bench specifically designed and developed for the investigation of the present propulsion system and described in detail in chapter 3. The experimental results revealed that the investigated porous geometry exhibits a permeability value that is excessively high for the intended application, resulting in an insufficient pressure drop across the wall. As a consequence, **the tested configuration was deemed unsuitable** for transpiration cooling in its current form, indicating that either a different porous geometry or an alternative manufacturing strategy must be considered for future developments.

Despite this experimental limitation, the research continued with the objective of assessing the theoretical cooling effectiveness of the transpiration cooling approach. For this purpose, a dedicated MATLAB numerical model was developed to simulate the thermal behaviour of the cooling system. The model is based on the **hybrid combustion theory** proposed by Allison and allows the evaluation of temperature and heat flux profiles within the boundary layer, as well as the estimation of the coolant mass flow rate required to ensure adequate wall protection. In order to explore the cooling potential under feasible conditions, the permeability of the porous wall was significantly reduced within the numerical simulation, effectively representing an optimized

porous structure.

The numerical results demonstrated that, within the range of validity of the adopted assumptions, the transpiration cooling approach is capable of providing effective thermal protection of the combustion chamber walls while requiring only a very limited fraction of the total propellant mass flow rate. The predicted temperature levels at the wall remain within acceptable limits, and the coolant demand is substantially lower compared to conventional film cooling techniques. These conclusions highlight the significant potential of transpiration cooling for advanced rocket propulsion systems, provided that suitable porous structures with appropriately tailored permeability can be realized.

Possible future research developments may follow several directions. A first step would consist in refining the current numerical assessment by adopting **more advanced theoretical models** and progressively reducing the number of adopted assumptions. In particular, a more detailed description of the boundary layer structure, phase change processes and reaction kinetics could be implemented in order to improve the predictive capability of the model and extend its range of validity. Such improvements would allow for a more accurate estimation of the heat flux distribution, flame positioning and coolant mass flow requirements.

Alternatively, a further advancement would involve the implementation of a **Computational Fluid Dynamics** (CFD) simulation. This approach would enable a more rigorous coupling between fluid dynamics, heat transfer and chemical reactions, thereby providing a more realistic representation of the transpiration cooling approach. However, several modeling challenges must be addressed in this context. In particular, a suitable strategy for simulating the injection of coolant through the porous wall must be defined, treating it as a distributed blowing flow interacting with the high-temperature reacting boundary layer. Additionally, the accurate representation of phase change and subsequent chemical reactions within the boundary layer regions would require careful selection of turbulence models, reaction mechanisms and multiphase modeling approaches. These aspects make the CFD investigation significantly more complex, but potentially far more informative.

Ultimately, the conclusive validation of the transpiration cooling concept with high-test peroxide would require experimental demonstration under realistic operating conditions. A **hot-fire test** performed on a representative propulsion system would constitute the decisive step in assessing the actual effectiveness of the cooling approach. The experiment would allow direct observation of the wall thermal response, verification of structural integrity and confirmation of the predicted coolant performance, thereby providing definitive evidence of the practical feasibility of the proposed solution.

The main challenge to adress before conducting an actual hot-fire test is identifying a **suitable manufacturing process** for producing porous components with adequate porosity and permeability. The present research has demonstrated that the Laser Powder Bed Fusion technique does not meet the requirements of the application. The pore dimensions that can be achieved with this manufacturing procedure remain significantly larger than those required for an effective transpiration cooling system, which would involve characteristic pore sizes on the order of tenths or hundredths of a millimeter. Consequently, the resulting permeability is excessively high and does not allow for the necessary pressure drop across the porous wall.

Therefore, the porous component manufacturing strategy has to be reconsidered. One possible direction would consist in further developing additive manufacturing approaches, which remain highly attractive due to their capability to realize complex internal geometries. Previous research campaigns have proved the feasibility of this manufacturing technique for the produc-

tion of fine porous walls for transpiration cooling applications [48]. In this context, the pore architecture could be redesigned in order to reduce not only the characteristic **pore size**, but also to modify the **connectivity** between pores. The pore network, in fact, strongly influences the permeability value, with the result that a more intricate and controlled interconnection between pores could significantly reduce permeability.

Alternatively, a more radical approach would involve shifting from additive manufacturing to conventional porous material production techniques, such as **powder metallurgy**, as discussed in chapter 2. Processes based on compaction and sintering of metallic powders may allow for the generation of much finer and more homogeneous pore structures. However, this route introduces additional uncertainties, as the final permeability depends sensitively on processing parameters such as compaction pressure, particle size distribution, sintering temperature and more. The identification of an optimal parameter set would likely require an extensive experimental campaign, involving iterative testing and characterisation in order to correlate the manufacturing conditions with the resulting microstructural and permeability properties.

In conclusion, achieving a porous structure with sufficiently low permeability represents the key technological challenge for the practical implementation of the proposed transpiration cooling system. Overcoming this limitation is a necessary requirement for progressing towards the ultimate experimental validation of this potential cooling approach.

Bibliography

[1] G. Sutton and O. Biblarz, *Rocket Propulsion Elements*. A Wiley Interscience publication, Wiley, 2001.

[2] P. Hill and C. Peterson, *Mechanics and Thermodynamics of Propulsion*. Addison-Wesley, 1992.

[3] USP Technologies, "Phase diagram." https://usptechnologies.com/phase-diagram/, 2026.

[4] Tameson, "Ball valve circuit functions." https://tameson.com/pages/ball-valve-circuit-function, 2021. Technical overview of 2-way and 3-way ball valve circuit functions.

[5] Mechanical-Engineering.com, "Needle valves – function and selection criteria." https://mechanical-engineering.com/needle-valves/, 2019. Technical overview of needle valve operation, flow control and selection criteria.

[6] InstrumentationTools.com, "Control valve actuators – pneumatic." https://instrumentationtools.com/control-valve-actuators-pneumatic/, 2019. Overview of pneumatic actuators for control valves, including piston and diaphragm actuator principles.

[7] STC Valve, "Solenoid valve specifications and dimensions: 2p050 series." https://www.stcvalve.com/Solenoid-Valve-Specifications-2P050-Series.htm, 2019. Technical specifications of 2-way normally closed direct-acting solenoid valves (2P050 series), including operating pressure, temperature, materials, and electrical characteristics.

[8] Goetze KG Armaturen, "Pressure relief valves and safety valves." https://www.goetze-group.com/en-us/goetzetechtalk/faq/faq-pressure-relief-valves-safety-valves, 2026.

[9] EnggCyclopedia, "Check valves." https://enggcyclopedia.com/2012/02/check-valves/, 2012. Overview of check valves (non-return valves), their working principle and main types such as swing, lift, tilting disc and piston check valves.

[10] Hy-Lok, "Micron inline filter." https://www.hylok.ca/products/valves/inline-and-tee-filters/micron-inline-filter/, 2026. Technical specifications and description of inline micron filters for particle removal in fluid systems, including replaceable filter elements and compact design.

[11] VIKING Life-Saving Equipment A/S, "Regulator r21 n_2 16 bar for dry powder system." https://www.viking-life.com/shop/firefighting-equipment/firefighting-systems-spares/dry-powder-system/regulator-r21-n2-16-bar-for-d

ry-powder-system/, 2026. Pressure regulator for nitrogen propellant cylinders in dry powder fire suppression systems, supplied with gauges and compatible with N_2 and CO_2 connections.

[12] KROHNE Group, "Flowmeters." https://www.krohne.com/en/products/flow-measurement/flowmeters, 2026. Overview of industrial flowmeters for volume flow, mass flow, density and concentration measurement, including electromagnetic, Coriolis, ultrasonic, vortex and differential pressure technologies.

[13] Engineered Seal Products (ESP International), "Bladder accumulators." https://www.espint.com/products/bladder-accumulators, 2026. Overview and technical specifications of bladder-type hydraulic accumulators, including design, operating principles, pressure ratings, and industrial applications.

[14] Kvota, "Thermocouple (termopara)." https://www.kvota.com.ua/en/statti/termopara/, 2026. Overview of thermocouples, including Seebeck effect, working principle, types of thermocouples and practical applications in temperature measurement.

[15] Process Parameters Ltd, "Miniature flat two pin thermocouple connectors rated to 220°c." https://www.processparameters.co.uk/thermocouple-connectors/miniature-flat-two-pin-thermocouple-connectors-rated-to-220c/, 2026. Technical specifications of miniature flat 2-pin thermocouple connectors with thermosetting plastic body rated up to 220°C, compatible with multiple thermocouple types (K, J, T, N, R/S, E, B, Cu).

[16] IC Components, "Guide to pressure transducers: Design, characteristics, and uses." https://www.ic-components.it/blog/Guide-to-Pressure-Transducers-Design,Characteristics,and-Uses.jsp, 2023. Comprehensive guide on pressure transducers covering working principle, components, types, characteristics, applications, advantages, and limitations.

[17] National Instruments, "Ni compactdaq systems." https://www.ni.com/en/shop/compactdaq.html, 2026. Overview of the modular CompactDAQ data acquisition platform, chassis and compatible C Series I/O modules for sensor measurements and test systems.

[18] National Instruments, "Ni-9213 c series thermocouple input module." https://www.ni.com/en-gb/shop/model/ni-9213.html, 2026. 16-channel thermocouple input module for CompactDAQ and CompactRIO systems, with built-in signal conditioning, cold-junction compensation and high-resolution ADC.

[19] National Instruments, "Ni-9202 c series voltage input module." https://www.ni.com/en-gb/shop/model/ni-9202.html, 2026. 16-channel differential voltage input module ($\pm$10 V) for CompactDAQ and CompactRIO systems with 24-bit resolution and simultaneous sampling.

[20] C. B. Allison, "Hybrid and decomposition combustion of the hydrazine fuels," NASA Contractor Report NASA-CR-72977, National Aeronautics and Space Administration, 1971.

[21] D. Huzel and D. Huang, *Modern Engineering for Design of Liquid-Propellant Rocket Engines*. Ingenieria de transportes y aeronautica, American Institute of Aeronautics and Astronautics, 1992.

[22] C. Percival, "Engine cooling – why rocket engines don't melt." Everyday Astronaut, 2022.

[23] W. Kopacz, A. Okninski, A. Kasztankiewicz, P. Nowakowski, G. Rarata, and P. Maksimowski, "Hydrogen peroxide – a promising oxidizer for rocket propulsion and its application in solid rocket propellants," *FirePhysChem*, vol. 2, no. 1, pp. 56–66, 2022. Progress in Solid Rocket Propulsion - Part A.

[24] Y. Yazici and H. Deveci, "Factors affecting decomposition of hydrogen peroxide," in *Proceedings of the XIIth International Mineral Processing Symposium*, Conference Proceedings, 2010.

[25] Chemical and Material Sciences Department, Research Division, Rocketdyne, "Hydrogen peroxide handbook," Technical Report AFRPL-TR-67-144, Air Force Rocket Propulsion Laboratory, Edwards Air Force Base, CA, USA, 1967.

[26] S. Schuh, T. Bartok, R.-J. Koopmans, and C. Scharlemann, "Hydrogen peroxide material compatibility investigation," in *Proceedings of the 6th European Conference for Aeronautics and Space Sciences (EUCASS)*, (Kraków, Poland), 2015.

[27] D. R. Mattie, "Toxicity of rocket fuels: Comparison of hydrogen peroxide with current propellants," Technical Report CPIA Publication 687, JANNAF 28^{x} Propellant Development & Characterization Subcommittee and 12th Safety & Environmental Protection Subcommittee Joint Meeting, Air Force Research Laboratory, HEST Division, Wright-Patterson AFB, OH, USA, 1999.

[28] I. Inchem, "Hydrogen peroxide (>60% solution in water)." IPCS Inchem, 2018.

[29] C. Chemicals, "Hydrogen peroxide, aqueous solution, with not less than 20% but not more than 60% (stabilized as necessary)." CAMEO Chemicals, 2025.

[30] PeroxyChem LLC, "Safety data sheet: Hydrogen peroxide 90% htp." `https://mae-nas.eng.usu.edu/Peroxide_Web_Page/documents/hydrogen-peroxide_90_htp.pdf`, 2015.

[31] D. J. Munk, M. Selzer, H. Seiler, M. Ortelt, and G. A. Vio, "Analysis of a transpiration cooled LOX/CH_4 rocket thrust chamber," *International Journal of Heat and Mass Transfer*, vol. 182, p. 121986, 2022.

[32] J. E. Terry and G. J. Caras, "Transpiration and film cooling of liquid rocket nozzles," NASA Contractor Report NASA-CR-78541, Redstone Scientific Information Center, Research Branch, U.S. Army Missile Command, Redstone Arsenal, Alabama, USA, Mar. 1966.

[33] S. Han, S. Dutta, and S. Ekkad, "Turbine blade film cooling," in *Gas Turbine Heat Transfer and Cooling Technology*, p. 21, Boca Raton, FL, USA: Taylor & Francis Group, 2 ed., 2013.

[34] S. K. S.L. Guseinov, "Hydrogen peroxide decomposition catalysts used in rocket engines," *Russian Journal of Applied Chemistry*, vol. 93, no. 4, pp. 467-487, 2020.

[35] Z. B. Jildeh, J. Oberländer, P. Kirchner, P. H. Wagner, and M. J. Schöning, "Thermocatalytic behavior of manganese oxide as nanoporous material on the dissociation of a gas mixture containing hydrogen peroxide," *Nanomaterials*, vol. 8, no. 4, 2018.

[36] RealPars, "Pneumatic actuators: How they work & key applications." https://www.realpars.com/blog/pneumatic-actuator, 2021. Overview of pneumatic actuator operation, types (linear and rotary), and applications.

[37] IQSDirectory.com, "3-way solenoid valves – function and operation." https://www.iqsdirectory.com/articles/solenoid-valve/3-way-solenoid-valves.html, n.d. Technical overview of 3-way solenoid valve operation, components, and design considerations.

[38] LS Electric, *KGLWIN User Manual*, 2022. https://sol.ls-electric.com/ww/en/product/document/2510.

[39] KROHNE Group, "Krohne coriolis mass flow meters." https://cmp.krohne.com/coriolis/, 2025.

[40] Wikipedia, "Mass flow meter." https://en.wikipedia.org/wiki/Mass_flow_meter, 2024.

[41] Fluke, "What is cold junction compensation in thermocouples?." https://www.fluke.com/en/learn/blog/calibration/what-is-cold-junction-compensation-in-thermocouples, 2026. Cold junction compensation in thermocouples and how it is calculated for accurate temperature measurement.

[42] National Instruments, "Data aqcuisition system and input modules, specifications." https://www.ni.com/en.html, 2026. Homepage of National Instruments, provider of test, measurement, and control solutions.

[43] National Instruments, *LabVIEW User Manual*. National Instruments, 2001. User manual describing the LabVIEW graphical programming environment and programming features.

[44] W. W. Woessner and E. P. Poeter, *Hydrogeologic Properties of Earth Materials and Principles of Groundwater Flow*. The Groundwater Project, 2020.

[45] A. Atangana, "Chapter 2 - principle of groundwater flow," in *Fractional Operators with Constant and Variable Order with Application to Geo-Hydrology* (A. Atangana, ed.), pp. 15–47, Academic Press, 2018.

[46] J. LAGE, "The fundamental theory of flow through permeable media from darcy to turbulence," in *Transport Phenomena in Porous Media* (D. B. INGHAM and I. POP, eds.), pp. 1–30, Oxford: Pergamon, 1998.

[47] S. Heo, *Design and validation of hydrogen peroxide/kerosene bipropellant thruster*. PhD thesis, Korea Advanced Institute of Science and Technology (KAIST), Daejeon, Republic of Korea, 2018.

[48] C. Poupinha, S. Kozlowska, J. Soriano Lluch, D. Altimare, and M. Kinell, "Experimental study on transpiration cooling through additively manufactured porous structures," *International Journal of Heat and Mass Transfer*, vol. 227, p. 125532, 2024.